**SAKARYA UNIVERSITY**
**INSTITUTE OF NATURAL SCIENCES**

# M13 VIRUS TEMPLATE AS A NEW APPROACH TO ELECTROCHEMICAL ENERGY STORAGE IN Li-O$_2$ BREATHING BATTERY CATHODES

## Ph.D. THESIS

**Ahmed Waleed Majeed AL-OGAILI**

| | | |
|---|---|---|
| **Department** | : | **NANOSCIENCE & NANOENGINEERING** |
| **Supervisor** | : | **Prof. Dr. Hatem AKBULUT** |

**August 2021**

# DECLARATION

I declare that all the data in this thesis was obtained by myself in academic rules, all visual and written information and results were presented in accordance with academic and ethical rules, there is no distortion in the presented data, in case of utilizing other people's works they were refereed properly to scientific norms, the data presented in this thesis has not been used in any other thesis in this university or in any other university.

Ahmed Al-Ogaili

19.08.2021

## PREFACE

I would like to thank my advisor Professor Hatem Akbulut for his guidance and all staff members throughout my laboratory work. He has constantly encouraged me to think critically about my research and provides guidance and advice when I need it.

I would also like to thank Dr. Tuğrul Çetinkaya for helping me develop an experimental plan. This work would not have been easy without the help of my friends Abdulkadir Kizilaslan and Ibrahim Fatih Kekik. I would also like to thank SARA PAKSERESHT, who cooperated with me on this work. It was our collective efforts that brought this work to an end. Working together was a pleasure. We worked hard, but we were able to have fun at the same time.

I would like to thank Mahmud Tukur and Seyma Ozcan. I am incredibly grateful to the experts of FESEM and XRD; they always managed to solve much better results. I also want to thank the rest of the SARGEM lab members. We were an outspoken team that had always had each other's support. The collaborative nature of our team drives the powerful scientific discoveries that happen every day.

I would like to thank M7 staff members, SARGEM staff members, and all of our team members, especially Mustafa Celik and Aslihan Öncü, not forgetting Dr. Mehmet Oğuz Güler and his team.

Finally, I want to thank my family for their support and patience.

# TABLE OF CONTENTS

# LIST OF SYMBOLS AND ABBREVIATIONS

| | |
|---|---|
| A | : Amper |
| Ar | : Argon |
| a.u. | : Arbitrary unit |
| C | : Capacity |
| CV | : Cyclic voltammetry |
| CMC | : Carboxylic methyl cellulose |
| EDS | : Energy dispersive X-ray spectroscopy |
| EIS | : Electrochemical impedance spectroscopy |
| FESEM | : Field emission scanning electron microscopy |
| GO | : Graphene oxide |
| $Li_2CO_3$ | : Lithium carbonate |
| $Li_2O_2$ | : Lithium peroxide |
| mA | : Miliamper |
| $N_2$ | : Nitrogen |
| nm | : Nanometer |
| NPs | : Nanoparticles |
| OER | : Oxygen evolution reaction |
| ORR | : Oxygen reduction reaction |
| rGO | : Reduced graphene oxide |
| SEI | : Solid electrolyte interface |
| TEGDME | : Tetraethylene glycol dimethyl ether |
| TEM | : Transmission electron microscopy |
| TGA | : Thermo gravimetric analysis |
| V | : Voltage |
| W | : Watt |
| XPS | : X-ray photoelectron spectroscopy |

XRD          : X-ray diffraction

2θ           : Scattering angle

Ω            : Ohm

# LIST OF FIGURES

# LIST OF TABLES

# SUMMARY

Keywords: Lithium-oxygen battery, Graphene, Cathode materials, Biosynthesis, nanocomposites

Due to high potential energy densities of lithium-oxygen (Li-O$_2$) batteries (11,140 Wh kg$^{-1}$) have been explored as one of the most promising energy storage systems for the future generation of state-of-the-art batteries. During discharge, oxygen (from the atmosphere) is reduced at the cathode (Oxygen reduction reaction, ORR), where it reacts with lithium ions released from the lithium metal anode to generate Li$_2$O$_2$, and the discharge residue decomposes during charging (Oxygen evolution reaction, OER). Cathode catalysts significantly improve ORR/OER and the electrochemical stability of Li-O$_2$ systems. To accelerate ORR and OER in Li-O$_2$ cells, a suitable air cathode architecture must possess sufficiently porous distribution to allow oxygen diffusion, high conductivity to transfer lithium ions, chemically stable, and highly catalytic activity. Therefore, we first report metal nanoparticles (e.g., Pd and Ru) and α-manganese oxide nanowire supported by reduced graphene oxide. In the Li-O$_2$ cathode, noble metals are used as oxygen evolution reaction (OER) electrocatalysts to minimise charge overpotential and provide stable cycling performance. MnO$_2$ is an appealing, useful transition metal oxide catalyst in Li-O$_2$ batteries due to its cost effective, high catalytic activity, and good oxygen reduction characteristics. In the first experiment, Ruthenium nanoparticles were incorporated on MnO$_2$ surfaces, and then the mixture was applied to 50% graphene via ball milling. This electrode demonstrates the charge overpotential and stability up to 40 cycles at a limited capacity of 800 mAh g$^{-1}$. The produced rGO@Pd@α-MnO$_2$ hybrid nanocomposite cathode delivered a full discharge capacity of 7500 mAh g$^{-1}$ and maintain cycle life upto 50 cycles with a low discharge/charge potential gap of 0.4 V. Our result shows higher stability of Pd despite Ru.

Furthermore, graphene-based electrodes with different graphene content (e.g. 100%, 75%, 50%) were prepared, and by reducing graphene, the higher performance of Li-O$_2$ cell was obtained due to preventing side reactions. On the other hand, plant extract and M13 virus were utilized for the reduction of graphene oxide and preparation of MnO$_2$ nanowires, respectively. Using these biomaterials assist in designing advanced nanomaterials through a green and biocompatible process.

Overall, the synergistically effects of α-MnO$_2$ nanowires and metal nanoparticles are combined in this study by decorating graphene sheets to boost cyclability and capacity, resulting in highly efficient Li-O$_2$ cell performance.

# Li-O$_2$ SOLUNUM PİLİ KATOTLARINDA ELEKTROKİMYASAL ENERJİ DEPOLAMAYA YENİ BİR YAKLAŞIM OLARAK M13 VİRÜS ŞABLONU

## ÖZET

Anahtar Kelimeler: Lityum-Oksijen Pil, Grafen, Katot Malzemeler, Bio-üretim, Nanokompozitler

Lityum-Oksijen piller sahip olduğu yüksek teorik enerji yoğunlukları(11,140 Wh kg$^{-1}$) sebebiyle geleceğin enerji depolama sistemleri arasında ön plana çıkmaktadır. Deşarj prosesinde oksijen katotta indirgenerek (Oksijen indirgeme reaksiyonu, ORR) lityum ile reaksiyonu sonucu Li$_2$O$_2$ oluşturmakta ve şarj sırasında tersinir olarak bozunmaktadır (Oksijen evrim reaksiyonu, OER). Katotta kullanılan katalizörler OER/ORR reaksiyonlarını geliştirmekte ve Li-O$_2$ sistemlerin elektrokimyasal kararlılıklarını arttırmaktadır. Efektif OER ve ORR reaksiyonları için üretilecek katot yapılarının oksijen difüzyonuna imkân veren gözeneklere sahip olması, lityum iyonlarını hızlı ileten, kimyasal kararllığa sahip iyi katalitik etki göstermesi gerekmektedir. Bu amaçla, metal nanopartikülleri ve alfa-mangan oksit nanoçubuklar ile dekore edilmiş indirgenmiş grafen oksit üretimi gerçekleştirilmiştir. Soymetaller (Pd, Ru), OER reaksiyonları için katalitik etki göstererek şarj aşırı gerilimini düşürmekte ve çevrim kararlılığının oluşmasını sağlamaktadır.

MnO$_2$ iyi oksijen indirgeme, yüksek katalitik aktivite ve düşük maliyet gibi avantajları sebebiyle Li-O$_2$ pillerde kullanılan fonksiyonel geçiş metal oksit yapılarıdır. Bu çalışmada, ilk aşamada MnO$_2$ yüzeyine Rutenyum nanopartikülleri dekore edildikten sonra ağırlıkça %50 grafen ile bilyalı değirmen yardımıyla kompozit haline getirilmiştir. Üretilen elektrotlar 800 mAh g$^{-1}$ limitli kapasitede kararlı 40 çevrim göstermiştir. rGO/Pd/α-MnO$_2$ hibrit nanokompozitinde 7500 mAh g$^{-1}$ ilk çevrim kapasitesi ve kararlı 50 çevrim değerlerine 0.4 V polarizasyon ile ulaşılmıştır. Pd nanopartikülleri, Ru nanopartiküllerden daha yüksek kararlılık göstermiştir.

Farklı grafen miktarları (%100, %75, %50) içeren grafen temelli elektrotlar hazırlanmıştır. Grafen kullanımı ile yan reaksiyonların oluşumu engellenerek Li-O$_2$ pillerde daha iyi performans elde edilmiştir. Diğer yandan bitki özü ve M13 virüsleri grafen oksit'in indirgenmesi ve MnO$_2$ nanoçubukların üretilmesinde kullanılmıştır. Biyomalzemelerin kullanımı ile çevre dostu ve bio uyumlu yöntemler ile ileri nanomalzemelerin üretimi sağlanmıştır.

Bu tez çalışması, α-MnO$_2$ nanoçubukların ve metal nanopartiküllerin grafen üzerine dekore edilerek sinerjik etkiler ile çevrim kararlılığı ve kapasitenin arttırılarak yüksek verimli Li-O$_2$ pillerin geliştirilmesini konu edinmiştir.

# CHAPTER 1. INTRODUCTION

## 1.1. Background And History Of Batteries

Energy demand and supply have always been crucial factors for the evolution of civilization. Energy demand is putting a strain on fossil fuel stocks; with the consumption of fossil fuels, energy, and environmental problems are among the most critical concerns in the 21st century. Rapid climate change and warming of the planet over the past century has made the curb of greenhouse gasses imperative to eliminate the release of a large quantity of $CO_2$ and other greenhouse gases during the combustion of fossil fuels; According to reports, oil consumption contributes to 40% of total $CO_2$ emissions and is a key source of global tensions. Nearly one-third of all greenhouse gasses are produced by the energy and transportation sectors. The scientific consensus of a $CO_2$ increase in average global temperature will cause adverse and irreversible climate change. On the other hand, since to the variation in oil prices. Therefore, a cleaner and more sustainable future sustainable energy generated from natural resources, energy in the form of electricity is produced from wind, nuclear power, solar, burning fossil fuels, and fossil-fuel-free transpiration such as electric vehicles, etc. are increasing demanded globally [1].

Along with the expanding market of electrification of transportation, require storage devices for their practical usage. This is heralded by different types of electric cars. As a result, clean energy retention and conversion systems are needed electrochemical devices, including batteries due to the intermittent nature and geographical limitations of each power source and provide enough power to electric vehicles and the range requirements for transportation rechargeable battery systems could be a viable option. Therefore, they play a significant influence in the efficient

use of renewable energy, is generating more interest than at any other point in the past [2].

Different battery systems have been introduced and are now available in stores. A battery is a device containing positive and negative terminals that transform stored chemical energy directly into an electric pass from the negative to the positive through the external circuit, generating an electrical current [3]. Figure 1.1. indicates a range of batteries still in development or commercially accessible, and analyzes their energy densities to gasoline.
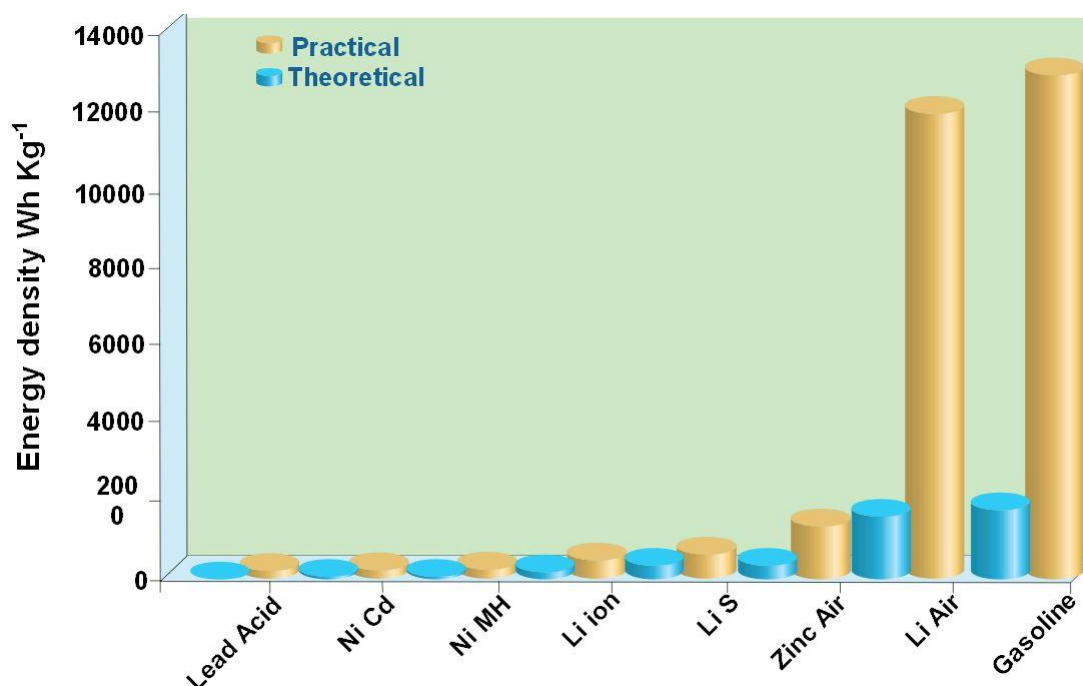


Figure 1.1. Comparison of gasoline the gravitational energy density Wh kg$^{-1}$ for different types of rechargeable batteries.

The Voltaic pile was the first battery developed by Volta circa 1800 consisted of copper and zinc separated by cardboards moistened in a saline solution [4]. After much research and development, batteries are now quite safe and used in different applications such as mobile phones, laptops, medical devices, power tools, scientific tools, digital electronics, and electric vehicles. Nevertheless, the high cost of batteries and limited driving range caused the limited marketing of electric vehicles.

The current state of electric vehicles uses Lithium-ion batteries, classified as secondary batteries which are rechargeable.

The current Lithium-ion has an energy density between $100 - 200$ W h kg$^{-1}$, which is hard to meet the needs for electric vehicles and renewable energy. On the contrary, due to Lithium-ion batteries' cycle life is relatively prolonged, and energy efficiency is considerable, which makes it one of the successful rechargeable battery technologies, which was originally launched in 1991 and is found in a wide range of portable electronic gadgets and equipment [5]. Gasoline has a potential energy density of 13,000 Wh kg$^{-1}$, and for industrial applications, the feasible energy density is 1700 Wh kg$^{-1}$, but taking in mind the energy conversion efficiency of about 13%, and the battery packs have a power density of less than 200 Wh kg$^{-1}$, which is still much less than the requirement of the automotive applications [6].

To provide the customers' requirements, the new battery development technologies must reach farther than the limitations of Lithium-ion batteries and offer new batteries with energy densities comparable to fuel engines. There are various alternative batteries with great specific energy densities that have got considerable interest because of their requirement in electric vehicles with a lighter weight, smaller size, and high energy and power densities such as Metal-air batteries (e.g., Iron-air, Al-air, Lithium-air, Zn-air, Mg-air) [7]. For example, Li-O$_2$ batteries give 3582 W h kg$^{-1}$ (in an aqueous electrolytes system) and 3505 W h kg$^{-1}$(in a non-aqueous electrolytes system) [8]. Figure 1.2. shows the different battery chemistries, practical, specific energy, and the estimated driving range for a pack weight of fully electric vehicle Nissan Leaf [9].

Lithium-O$_2$ batteries are currently under the stage of research & innovation and, in a single charge, have the ability to make an electronic car go a driving a range of further than 550 kilometers, which is about three times the driving distance more than the current electric car powered by Lithium-ion batteries [10]. In addition, lithium air batteries have gotten a great deal of interest because of the metallic air battery cathode gaining oxygen from the environment air as a reactor in the

electrochemical process instead of storing the heavier electrode materials like in other battery systems [11].
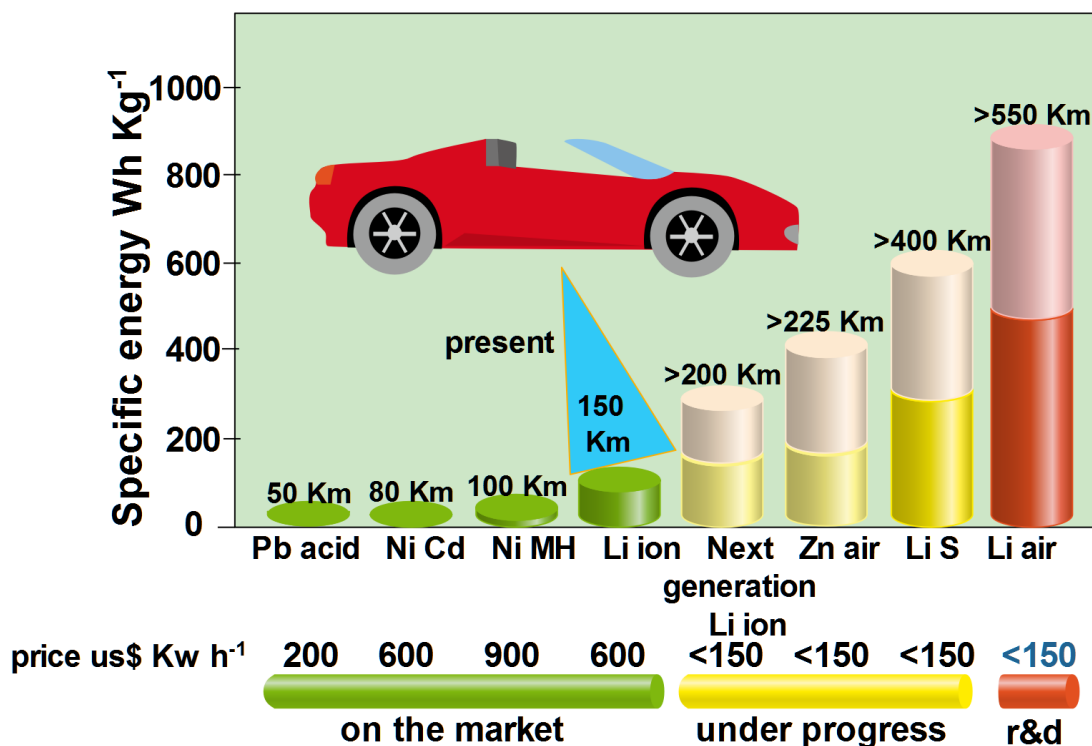


Figure 1.2. Some rechargeable batteries and their specific practical capacities with packaging prices and estimated driving distances. The other color region of the strip shows the expected range of future technology. Values are measured against the Li-ion battery rated power and driving range (Nissan LEAF car).

## 1.2. Thesis Aim And Objectives

Lithium-air batteries can be future power storage and generation technologies in automotive and smart grid applications. Despite the excellent theoretical performance, the Lithium-air battery implementation continues to be hampered by poor cycle retention, low energy efficiency, and safety concerns with the metallic lithium metal anode. Nanomaterials and nanotechnology are believed to be one solution to the great challenge of lithium aerobic systems. However, cathode development, including structure design and electrode materials, is the key.

In this thesis, the development of several nanomaterials was constructed for cathode materials in Lithium-air batteries. Efforts have mainly emphasized carbon-based

nanomaterials synthesis, including reduced graphene oxide nanosheets and incorporated with heterogeneous metal/metal oxide used as electrode materials to design the structure.

It has been found that the main reasons for causing serious degradation of electrochemical performance by impeding the redox reaction reversibility are a generation of accumulation of soluble discharge products and unwanted side-products. Since both $O_2$ evolution reaction and the oxygen reduction reaction take place on cathode of the Lithium-air battery, so to enhance the performance of the Lithium-air battery, the electrocatalytic cathode materials are developed that limit the formation of side-products while facilitating the $O_2$ reduction reaction and the oxygen evolution reaction the process is crucial.

Although these factors are interdependent and overlapping, whereas doping and hybridization of heteroatom determine the oxygen redox kinetics associated with the oxygen evolution reaction and the oxygen evolution reaction, the structure of the catalyst essentially limits the diffusion of oxygen and the storage of discharge products on the oxygen electrode.

This work focuses on exploring stable two-functional oxygen electrodes towards the oxygen evolution reaction and the oxygen evolution reaction to produce a high-performance non-aqueous Lithium-air battery. In order to achieve the goal, the following purposes have been covered as follows:

1. Verify the relationship between rGO porous structures and the electrical stimulation performance of cathode materials in Li-$O_2$ batteries.

2. Discover our effective cathode catalysts towards both ORR and OER in lithium-$O_2$ batteries to improve performance at specific capacity and stable cycling.

3. Improving Li-$O_2$ battery performance by introducing new carbon-based composite cathode materials.

4. Reducing the side reactions by decreasing graphene contents and utilizing effective catalysts.

5. Graphene oxide was produced through a modified hummers method in all experiments, and various reducing agents employed reduction of GO.

The noble metals (such as: Pd, Pt, Ru, Au), and transition metal oxides (like $MnO_2$, $TiO$, $Co_3O_4$, $MnCo_2O_4$), and materials made of carbon (such as Carbon nanotubes, graphene, and carbon fiber) have been all studied as electrodes for catalysts to achieve increased (decreased) discharge (charge) voltages also improved percentage efficiency [12]. Due to its peculiar properties of graphene, such as the high electrical conductivity, high thermal conductivity, and so on, massive total surface area, and good charge mobility, graphene has received a lot of attention as a desirable quality substrate for storage of energy [13]. However, side reactions, including lithium carbonate and lithium carboxylate that occur above 4.2 V, can decompose into lithium, dioxide carbon, and oxygen, have been identified, resulting in the Bare graphene electrodes have a low catalytic action [14]; also the carbon materials are unstable [15]. Consequently, graphene-based nanocomposites have been proposed to assist nanocatalysts made of metals/metal oxides to increase graphene's catalytic activity and minimize the potential for charge to prevent parasite discharge product formation [16]. Furthermore, several studies have looked into this design to attain better capacity and reduced charge-discharge potential using bifunctional catalysts. In this thesis, to increase the electrochemical efficiency for the Li-$O_2$ energy storage, various graphene-based nanocomposites cathodes architecture was developed and integrated with metal and metal oxides. The combination of metal/metal oxide with graphene enhances the properties of graphene, and the nanoparticles can serve as a stabilizer to avoid stacking graphene layers.

First of all, graphene oxide was prepared through a modified hummers' method, then reduced by different reducing agents, such as salvia extract, sodium borohydride, and hydrazine. Next, the effect of each reducing agent was investigated on the thickness and reduction of graphene oxide.

Different experiments were performed to manufacture the graphene based nanocomposites. In the first experiment, a composition of Ru and $\alpha$-MnO$_2$ was prepared. Synthesizing of $\alpha$-MnO$_2$ nanowires was developed by an easy microwaved hydrothermal method. Then, the product was mixed with 50 % graphene. However, the electrochemical test was limited to 40 cycles, which one major problem was the agglomeration of graphene layers that prevent the penetration of electrolytes. Therefore, avoiding oxygen transportation and leads to fading the capacity.

To overcome this issue, Pd nanoparticles were incorporated with graphene oxide layers and simultaneously reduced them. It is believed that by anchoring metals on functional groups of graphene surfaces, the stacking between layers can be reduced and open enough space for electron and O$_2$ diffusion. As a result, the battery life cycle improved up to 50 cycles, and overpotential has alleviated significantly.

Moreover, to conduct an eco-friendly and unique structure of $\alpha$-MnO$_2$ nanowires, a Bio-template was utilized. As a result, we have obtained a rough structure of MnO$_2$, while with the assistance of microwave, a smooth surface of MnO$_2$ was observed. The capacity of the battery extremely increased due to this rough structure, which provided a higher number of active sites for the deposition of discharge products.

# CHAPTER 2. VIRUS TEMPLATED IN ENERGY STORAGE

## 2.1. Overview Of M13 Phage

The bacteriophages, also known informally as phages, reproduce and infect inside archaea and bacteria. Bacteriophages have been identified as one of the most widespread living organisms on the planet; they play a crucial role in sustaining the Earth's microbial balance.

Bacteriophages are anywhere that their bacterial host is found; With an expected total number of $10^{32}$ phages, it has been formed on earth, the number of phages falls within the range of $10^9$ virions per gram in soil and aquatic systems around $10^4$ to $10^8$ virions per ml. Phage consists of proteins that coat the genome of RNA or DNA, and their structures may be either complex or simple. Bacteriophages are small viral while not affecting cell lines of other organisms but showing the ability to kill bacteria.

Due to the highly specific nature of the binding, the host range of a particular bacteriophage is often restricted to a single type of bacterium, and its genome is injected into the host's cytoplasm after bacteriophage attachment, where the genes are expressed. Their genomes may encode as many as hundreds of genes and as many as four. The use of bacteriophage as a therapeutic has been advocated since its conception due to the specificity of cellular hosts targeted for the treatment of chronic and acute infections with first breakthroughs in various applications.

In 2006, M13 virus based on metal oxides was introduced to biotechnology for the first time. Since that time, it has sparked the interest of scientists. And because M13 virus is genetically easy to modify, safe to humans, and easy to replicate, all of this

makes it an interesting biological model material [17]. M13 virus is a phage that uses E. coli, which is a bacterial host cell (Figure 2.1.).
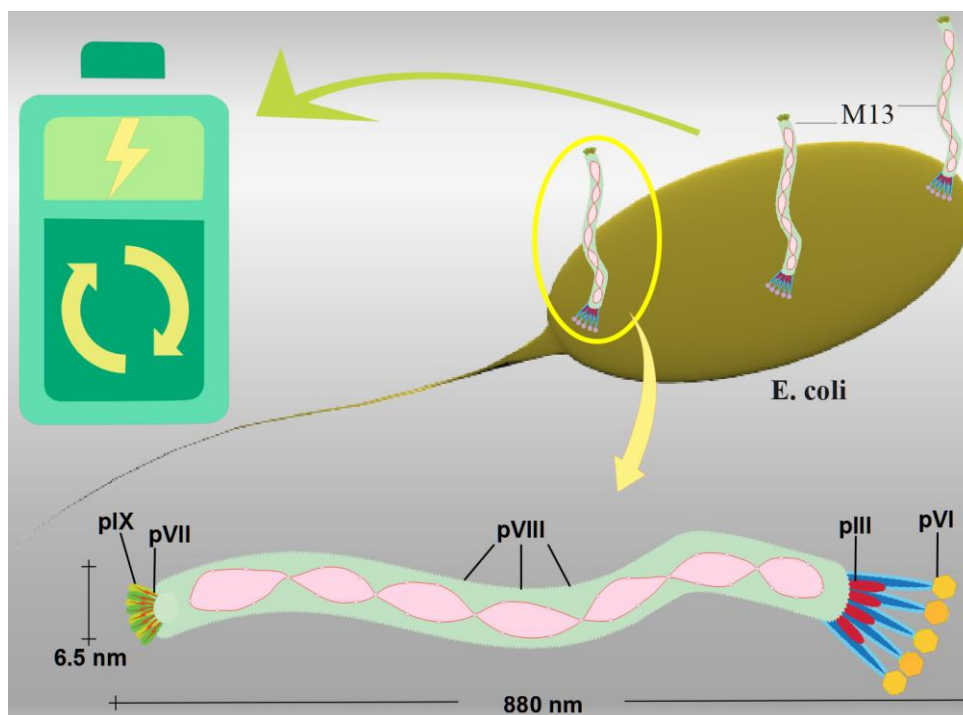


Figure 2.1. schematic image of wild type M13 bacteriophage.

E. coli usually lives in the colon of humans, mammals, and gram-negative bacteria in rodents. It could be grown fast on a minimum medium consisting of salts supplying nitrogen and carbon compounds like glucose, trace minerals, and phosphorous. E. coli multiply fast, so in a rich medium, it supplies bacteria cells with nucleotide precursors, vitamins, amino acids, and various metabolites to grow [18].

A limited number of cells are introduced into a volume of sterile medium first, and Escherichia coli grows at an aqueous medium. After several moments have passed, named the period of lag, Escherichia coli cells start dividing. The number of excellent strains will multiply at rich culture medium, every 30 or 20 min multiplication in numbers. So log stage is the phase of bacteria cells in a culture growing at an exponential rate. Finally, the bacteria cell density rises to the point that oxygen or nutrients start to consume the medium, and the cell waste products have reached concentration, inhibiting the rapid growth. In this stage, an ordinary

laboratory condition happens if the medium reaches $1–2 \times 10^9$ cells/ml density, the bacteria cells end the fast-dividing. Saturation is the name for this stage, The medium which has gotten such density has just been saturated.

Regardless of great expansion in brewer's yeast Saccharomyces cerevisiae as an active organism, Escherichia coli K-12 is still the preferred bacteria host of most molecular biological modifying. Several advanced studies for molecular biology start with the study of Escherichia coli and the phages (M13) and plasmids, which it is utilized as a bacterial host. Many of the reproduction techniques at present employ achievement facts for Escherichia. Coli K-12, its bacteriophages and plasmids, was studied in the 1970s and 1960s.

M13 virus is about 6.5 nm in diameter and 900 nm in length. The M13 virus consists of a single-stranded RNA nucleus coiled with 5 major proteins that coat it [19]. The pVIII protein has a serious effect on producing M13 viral metal oxide nanowires, as it is the most important among the 5 coating proteins. The amino acid residue (AEGDD) on the surface of the phage, at the amino end of the pVIII, is exposed. At pH 7, G&E amino acids carry a negative charge. Due to the negative surface charge, the M13 virus works with the metal by ion exchange. Therefore, ion exchange between metal and amino acids has a serious effect in preparing metal oxide coated nanowires. The researchers modified the structure of the pVIII protein so that instead of 1 glutamic acid, the surface contains 3. This structure provides a good binding among M13 virus and silver to improve the performance of M13 as template material for silver products [20].

The genetic modification provides multiple functions of the material and allows for a great increase in the interaction between the M13 virus and the metal. The M13 based electrodes can remarkably improve the metal oxide battery efficiency, significantly reducing the particle size of the materials. The M13 virus has already been used as template products for iron phosphate and cobalt oxide, which are very common electrode materials for a Li-ion battery [21].

To alter the DNA of the virus using gene editing technology so that the M13 virus carries four glutamic acids on the surface instead of one. Therefore, the genetically modified M13 holds four times more charge density than the wild M13 virus and this modification has remarkably enhanced energy efficiency generation. The generated electrical energy from the thin films of M13 virus can correspond to the number of glutamic acid on the surface. The small battery based on M13 phage can be used in different systems due to its excellent electrochemical performance.

The employment of M13 phages could be an ideal growth for the manufacture of new electrode materials and could provide a stable and ideal source of power for electronics and machinery. The M13 bio-design virus could be utilized in various applications like power generation, electrodes, energy conversion, and antibacterial materials. The M13 virus holds a negative charge at 7 pH due to aspartic acid and glutamic acid, as their traction on their side chains contains carboxyl groups. On the surface, the negative charge can contain an ion exchange reaction with the metal and the force of the reaction can be determined by Coulomb's law.

Rising the glutamic acid number on the protein's surface was the 1st way to increase the surface charge of M13 virus. This modification increased the interaction between the M13 virus and the metal and provided a binding force between the M13 virus and the metal.

### 2.2. M13 Phage As A Template For Electrodes

Since $MnO_2$ is a highly considerable material globally, the application of $MnO_2$ based electrodes can be ideal competitor electrode materials to Li battery. Moreover, compared to other electrode materials, $MnO_2$ electrode material is much cheaper. They altered the structure of the pIII protein so that the M13 virus has a binding force. A product with an M13 phage can be a very well catalyst because of its large surface area to the volume ratio.

Material developments provide very high energy rates, which are significant apps utilizing much energy, like hybrid electric automobiles, electric cars, also mobile electronic devices. It has been approved in many research that M13 phage-based materials could remarkably improve the efficiency of the metal oxide battery and dramatically reduce the material particle size due to the phage template use. M13 viruses have been applied as template materials for iron phosphate and cobalt oxide, which is a very common material in Li-ion battery electrodes.

In the case of Lithium-ion batteries, decreasing the size of the materials can increase the electron and $Li^+$ transfer in the electrode of the nanostructures. Two genes of M13 phage was manipulated by Lee's group, and the phage was fitted with 1 end peptide that can nucleate noncrystal a $FePO_4$ over peptide groups and on peptide groups (Figure 2.2.) [22]. It has the ability to be attracted SWCNTs (single-walled carbon nanotubes) merged to the major phage protein of the coat. The virus replicates with the largest bonds with a single-walled carbon nanotubes energy performance ($FePO_4$) similar to c-$LiFePO_4$ (crystalline lithium iron phosphate). The as-prepared electrode indicated good capacity retention for lithium ion batteries at the rate of 1C. Electrical appliance improvements have raised the need for a stable and continuous energy supply. Nevertheless, the development of new energy supply progress is away behind improving electrical appliances. For that, manufacturing suffers from providing few energy sources to meet these vast requirements.
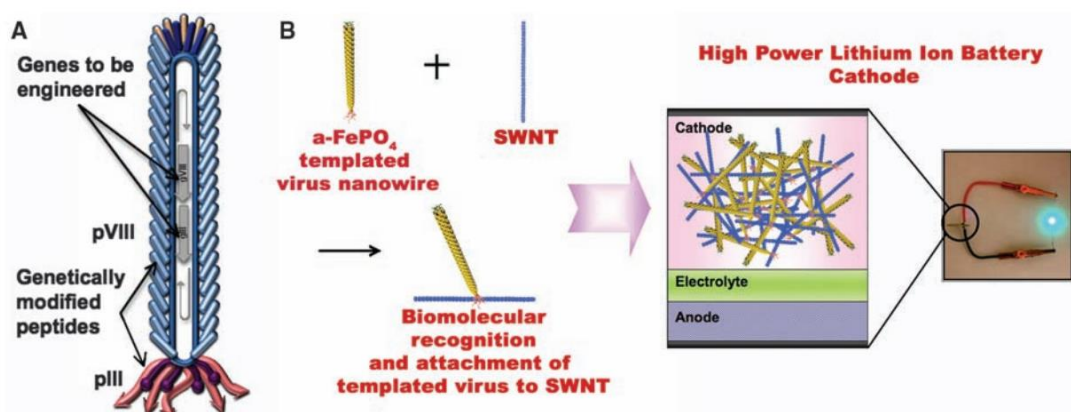


Figure 2.2. The schematic diagram shows the genetic modification of M13 (A) and assembling of $FePO_4$ on the surface of M13 virus and attachment of SWNT into a tip of M13 phage (B), and applied for Li-ion batteries [22].

Moreover, Lee's group reported that the piezoelectric energy was generated by the thin film of the M13 virus due to the liquid crystal properties and the piezoelectricity of the M13 viruses to generate energy [23]. To increase the energy generation efficiency to maximum, Lee's research team used gene modification technology to alter the virus's DNA, so the M13 virus, instead of one glutamic acid (E) on the surface, would contain four glutamic acids. For that, the transgenic M13 phage holds a charge density four times greater than the wild M13 phage, and this change has remarkably enhanced the efficiency of energy generation. Figures 2.3 and 2.4 showed the overall observation of the piezoelectric characteristics of a single-layer bacteriophage-based texture, by manufacturing the self-assembly of a single-layer bacteriophage thin film, designed as small rows, in a golden substrate. And the virus net dipoles in its axial direction, which makes the cantilever keep bending in the opposite direction when checking viruses that are opposite to the other direction, and the helical progression of the dipole causes the radial complex, which is the independent direction.
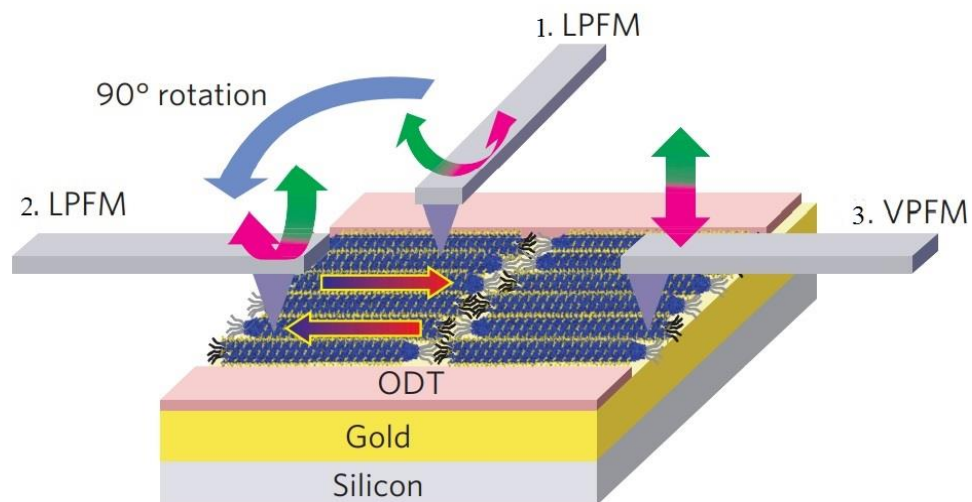


Figure 2.3. One-layer piezoelectric bacteriophage thin film features. This Figure shows the measures of the piezoresponse force microscopy. A single layer of viruses was gathered on molecularly patterned converging golden substrates, and piezoresponse force microscopy was characterized with vertical piezoresponse force microscopy (VPFM, 3) and side piezoresponse force microscopy (LPFM; 1-2) techniques [23].
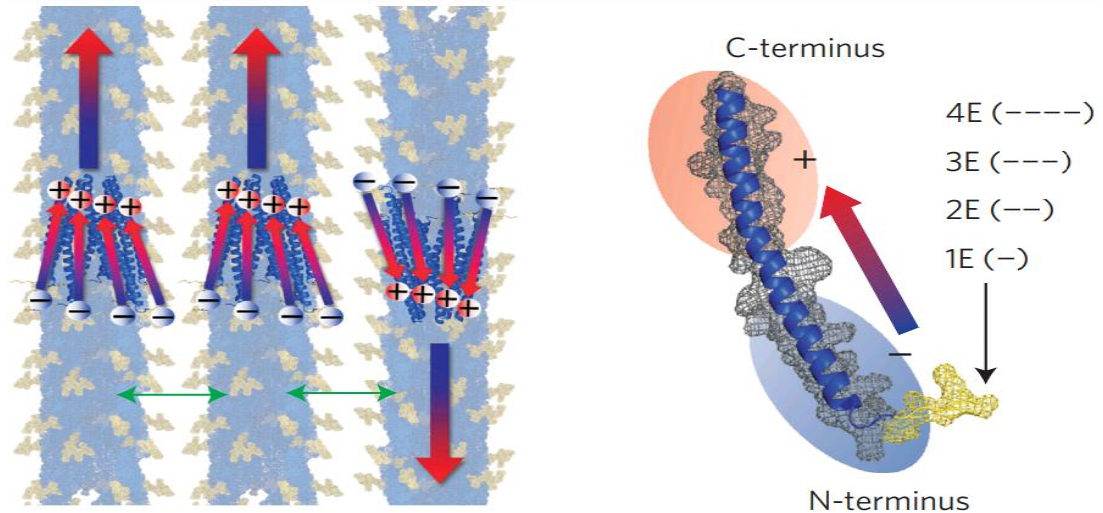
Figure 2.4. Shows bacteriophages with indiscriminately different dipoles by axial rotation of the single layer, that both directions are shown in blue and red arrows, then green arrows indicate the dipole selections of radial complexes. It also shows a dipole-density mononuclear pVIII protein which can be tuned via modifying the yellow fraction of glutamate (1E) at its N-terminus [23].

The appliance transforms the energy from the mechanical energy in the film into electrical energy by utilizing the dipole moment of the M13 virus. It is among the most important achievements of M13 bacteriophage application studies to date. This explains that the generation of electrical energy from the surface of the M13 bacteriophage film could be bind with several glutamic acids.

For example, the M13 phage 4E genotype synthesized approximately 3 times higher electrical energy than the wild bacteriophage 1E under the same circumstances. Depending on the amino acid negative charge, the M13 virus could successfully convert energy from mechanical energy to electrical energy [24].

This product is safe for the environment as the low temperature biological scaffold can ease the production of electrodes from materials that are not once embedded due to low electronic conductivity.

Once again, the Belchers team reported the production of bacteriophage-based M13 electrode microscale batteries [25]. The main challenge in producing small batteries is to decrease the amount of the electrically passive part. For an ordinary battery, the electrically inactive parts are taken approximately half the mass. They solved the

issue by utilizing M13 bacteriophage self-assembly on a PAA / LPEI polymer. After the bacteriophage M13 metallic oxide compound was accomplished on the polymer, a small phage-based battery was produced. General battery images are shown in Figure 2.5.

The M13 phage based small battery showed excellent electrochemical performance and could be utilized in various devices. Bacteriophage-based electrodes could be utilized in devices that require a great deal of flexibility. Producing small batteries is a successful way to integrate nanotechnology, biology, polymer science, and interface phenomena. The employment of M13 bacteriophage could provide a stable and large power source and could be a significant increase in the production of new small electrode material for electronics and small machinery.
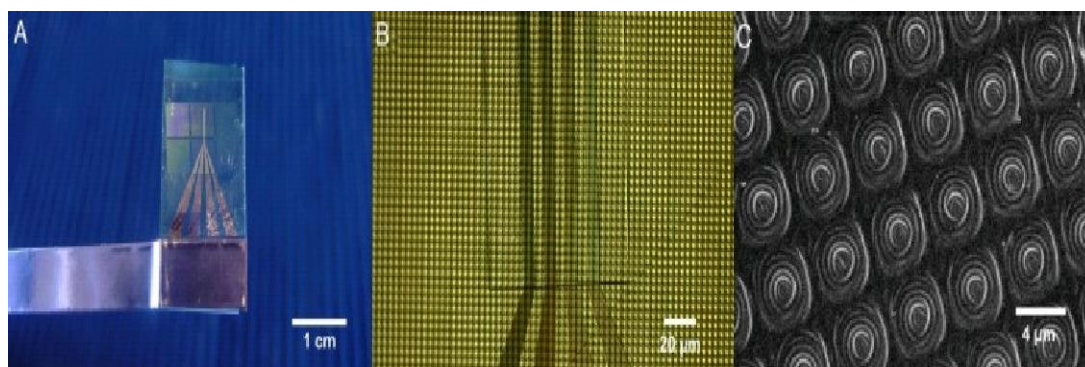


Figure 2.5. The electrode based on the M13 phage, self assembling and sealed small battery (A) shows Pt current collector of a small battery. (B) The electrodes of the small batteries are shown under the optical microscope on the 4 Pt current collector. (C) A sealed electrode of the small batteries is shown under the SEM [25].

# CHAPTER 3. LITHIUM-OXYGEN BATTERIES

## 3.1. Introduction To Lithium-Oxygen Batteries

The chemistry concept of Lithium-air batteries was originally released for the first time in 1976, but it received much attention by Abraham et al. in 1996, and a non-aqueous electrolyte battery system has been introduced and in 2006 by Bruce et al. [26].

The typical non-aqueous Li-$O_2$ batteries work by $Li_2O_2$ formation during $O_2$ reduction reaction (ORR) process, and deposit on the cathode (Discharging), and $Li_2O_2$ decomposes through oxygen evolution reaction (OER) into Lithium-ions (Charging). However, because air contains carbon dioxide and $H_2O$, new studies in lithium-air batteries generally concentrated in oxygen gas rather than air, which also causes the ideal chemical structure to be disrupted [27, 28]. The current Lithium-air battery still has a low effective energy density comparing to theory of energy density or to a gasoline-powered automobile combustion engine [29]. With excellent theoretical performance, the implementation of Li-$O_2$ batteries continues to be hampered by low energy efficiency, poor cycling ability, and safety concerns with metallic Li-$O_2$ anode.

It has been found that the major reasons for the accumulation of dissolvable discharge products and the unwanted generation of by-products are to cause serious decay of electrochemical performance by hindering the reversible redox reaction (ORR/OER) [30].

To enhance the Li-$O_2$ batteries' performance, the development of electrocatalytic cathode materials while reducing the formation of by-products is critical as both

ORR and OER occur on oxygen electrode of Li-O$_2$ batteries facilitating the ORR / OER process [31]. Various factors, including surface structures, heteroatom stimulants, and hybridization of electrochemical catalysts, were associated with ORR / OER efficiency. To mature this novel electrochemical energy system, many basic and systematic studies are needed. Although these factors are interrelated and interdependent, the structure of the catalyst essentially limits both retention of discharge products as well as the absorption of oxygen to the air electrode, while the hybridization and heteroatom doping of the heteroatom determine the oxygen-reduction kinetics associated with the ORR / OER reactions [32, 33]. In the future, for the next generation of energy sources, there is no doubt that the Lithium-air battery has a focal area of study that could make electric cars more accessible to the general public market. Four Li-O$_2$ battery architects are currently developing using a different form of electrolyte the aprotic, the aqueous, the hybrid, and all-solid-state electrolytes (Figure 3.1) [34].
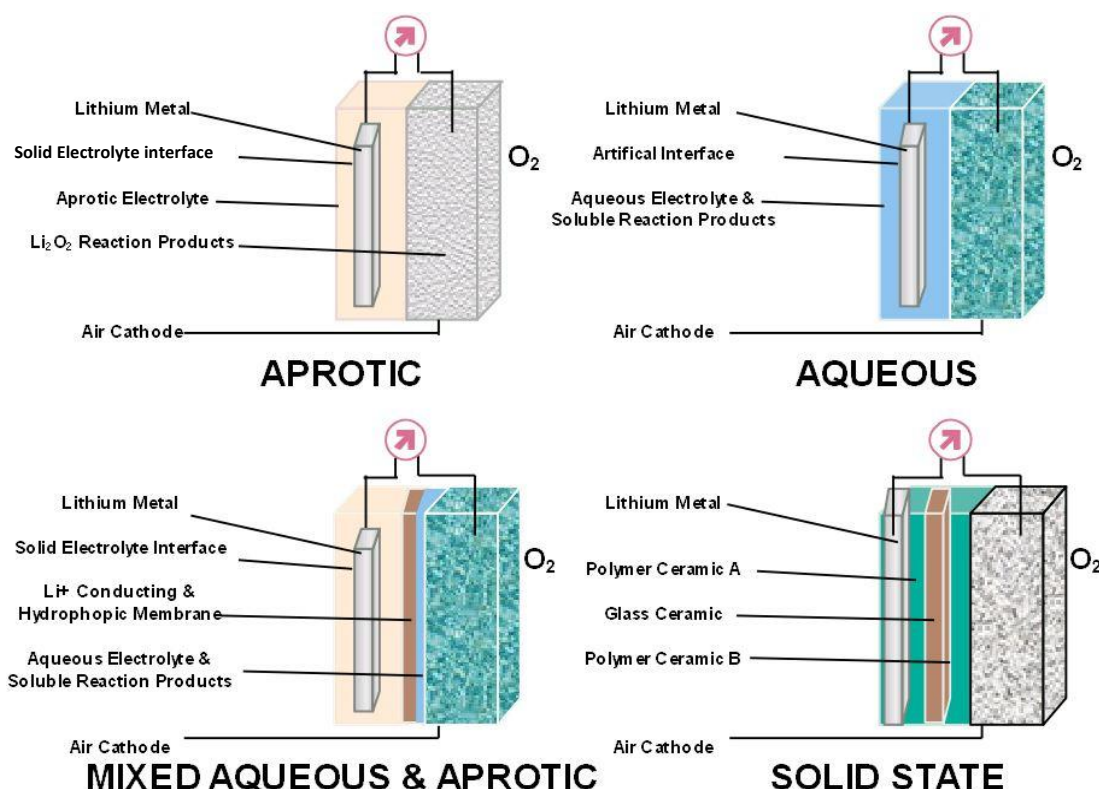


Figure 3.1. Architectures of four different Li-O$_2$ batteries, all of which assume the anode using lithium metal. The three structures of liquid electrolytes are an aqueous, non-aqueous, and mixed aqueous-aprotic system. In addition, the fully solid state structure is also provided. In the Figure, the main components are classified.

The electrolyte for the solid-state structure is made of polymer and glass ceramics, while all the Aprotic, aqueous, and mixed structures use liquid electrolytes [35]. The aprotic system is advantageous. Since the $Li_2O_2$ reduction system has been demonstrated to be beneficial, it can be converted back to the chemicals used in the $O_2$ reduction process (ORR) reagents.

The oxygen evolution reaction (OER), which refers to the recharging capability of the aprotic Lithium-air battery, is appropriately named because only the Lithium-air battery demonstrated the promise of electric recharging potential, as shown in (Figure 3.2.).

The aprotic cells have the advantage over aqueous and mixed with electrolyte structures, which are characterized that the electrolyte is in physical contact with the metallic Li anode. Thus, somewhere at anode, an oxidation process takes place. (Li $\rightarrow$ $Li^+$ + $e^-$) while discharging an aqueous lithium-air cell; somewhere at cathode, those lithium ions are produced to interact with $O_2$ to yield $Li_2O_2$ (and perhaps $Li_2O$), and electrons flow through an external circuit [36, 37].
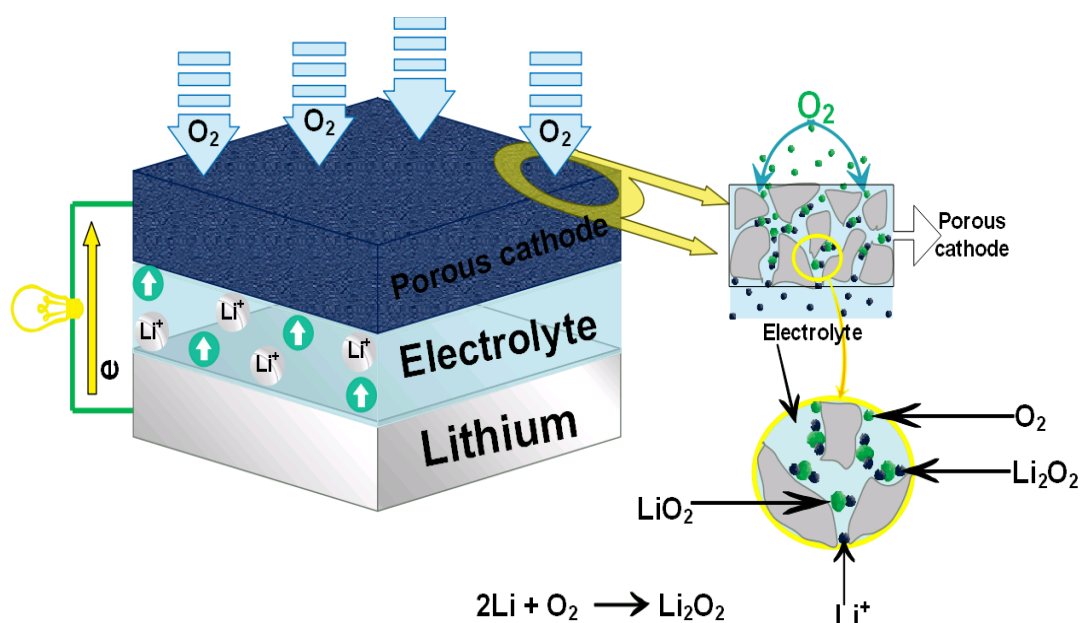


Figure 3.2. Schematic of uncommon Li-$O_2$ batteries and cathode structure.

The $O_2$ gets reduced at the air electrode either in a two-electron or four-electron mechanism like demonstrated in the ½ cell processes below:

$$O_2 + 2e^- + 2Li^+ \rightarrow Li_2O_2 \qquad (3.10 \text{ V}) \qquad\qquad (3.1)$$

$$2O_2 + 4e^- + 4Li^+ \rightarrow 2Li_2O_2 \qquad (2.90 \text{ V}) \qquad\qquad (3.2)$$

The aqueous and mixed electrolytes should use a $Li^+$ permeable membrane between Li electrodes and the aprotic electrolyte to prevent the water from interacting with the lithium metal [38]. For this reason, this thesis will cover the Li-$O_2$ cells using non-aqueous electrolytes. The potentials of reactions (3.1) and (3.2) are close; as a result, that after discharge mechanism, $Li_2O$ and $Li_2O_2$ have been the most common reduction results. With applied external potentials, the preceding reaction is expected to be reversal; that is, metallic lithium is placed just on Li electrode, and $O_2$ is produced or created at the air electrode. However, based on studies with Raman spectroscopy from Bruce et al. and Abraham et al., The $Li_2O_2$ reaction was identified as the predominant reducing product, and its intermediates were formed after degassing.

Moreover, due to the fact that $Li_2O$ is thought to be electrochemically not reversible, $Li_2O_2$ exhibits better rechargeable capacity than $Li_2O$. $Li_2O$'s stable surfaces, on the other hand, are non-magnetic and dielectric. Despite the fact that both $Li_2O_2$ & $Li_2O$ constitute nonconductive, a new investigation found that sustained $Li_2O_2$ surfaces are semi-metallic.

Given that for a non-aqueous lithium-air rechargeable battery, $Li_2O_2$ is preferable, the actions of charging/discharging reactions currently at non-aqueous lithium-air batteries are reductions/oxidation involving lithium peroxide formation [39]:

$$\text{Charge:} \qquad Li_2O_2 \rightarrow 2Li + O_2 \qquad\qquad (3.3)$$

$$\text{Discharge:} \qquad 2Li + O_2 \rightarrow Li_2O_2 \qquad\qquad (3.4)$$

The electrical and chemical reflection of cells containing $Li_2O_2$ as such degassing production, as well as the nonreversibility for cells discharging the $Li_2O_2$ as the discharge production, may be explained by the different physicochemical characteristics of these compounds [40]. To better understand the chemical processes, a possible mechanism that occurs during discharge at the air electrode has been proposed.

$$O_2 + e^- \rightarrow O_2^- \tag{3.5}$$

$$O_2^- + Li^+ \rightarrow LiO_2 \tag{3.6}$$

$$2LiO_2 \rightarrow Li_2O_2 + O_2 \tag{3.7}$$

Over the past years of studying the mechanism, many potential ways for decreasing $O_2$ in $Li^+$ electrolytes have been suggested. In the non-aqueous electrolyte, in the existence of $Li^+$ ions, $O_2$ is initially reduced to $O_2^-$, and on the surface of the electrode, the produced $O_2$ binds to $Li^+$ to form $LiO_2$ [41]. As illustrated by the reaction, $LiO_2$ was not stable also disproportionate to much more stability of $Li_2O_2$ (3.7). As a result, $Li_2O_2$ has been the final discharge production.

Moreover, according to Bruce et al., their charging action mechanism is based on a straight breakdown, as shown below:

$$Li_2O_2 \rightarrow 2Li^+ + 2e^- + O_2 \tag{3.8}$$

## 3.2. Challenges In Li-O$_2$ Batteries

Lithium-air batteries have a large actual capacity, specific energy based on lithium since starting with lithium (0.006941 kg mol$^{-1}$), the steady state voltage is 2.96 V, and the theoretically specific energy is 11,431Wh kg$^{-1}$.

$$\text{Spec.E} = \frac{2.96 \text{ V x } 96500 \text{ C/mole}}{3600 \text{ C/Ah X } 0.006941 \text{ Kg/mol}} = 11,431 \text{ Wh/Kg}$$

Since the Li-air battery significantly increases specific energy upon the Lithium-ion, it is considered the "new hope" for battery technologies. In a typical Li-$O_2$ battery, electrons are enclosed to the electrode, and $O_2$ is present in forms of the gas and solution, while Li ions are present in the electrolyte [42]. Currently, the specified theoretical energy for non-aqueous Lithium-air systems is higher than the practical energy. Battery constituents, such as electrolytes (lithium salts and solvents), cathodes, and anodes, are unable to meet the demands of actual applications.

However, from the previous sections, it becomes clear that Li-air batteries are a very complex system in which each component hosts a set of challenges and difficulties (Figure 3.3) before it is implemented for commercial applications [43].
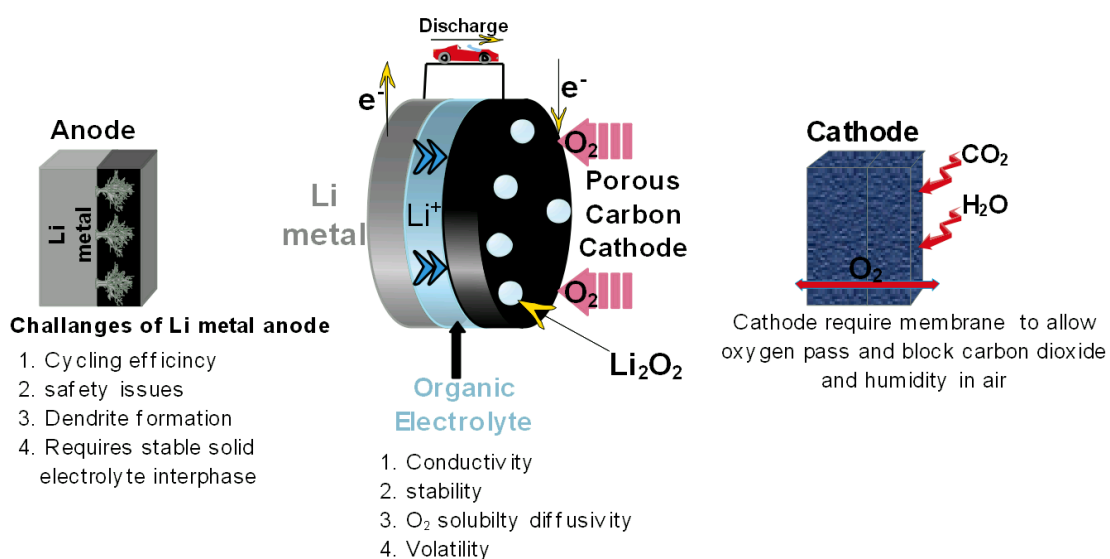


Figure 3.3. Challenges are facing aprotic lithium-air batteries. The use of electrolytes for the ether and more stable carbon electrodes reduces amplitude fading, although it does not eliminate it.

To conduct the half-cell reaction, oxygen molecules take electrons from the cathode and interact with lithium ions during discharge. Each reactant overcomes its limits resulting in a slow kinematic reaction to complete the set, thus affecting the overall

performance of the batteries. Moreover, these components overlap, rendering the analysis of each particular component more complex. However, it has been shown that the characteristics of the cathode strongly determine the performances of the batteries; Thereby, our aim is mainly on the issues of cathode for the Li-air battery.

The main challenges still facing the current state of the Li-$O_2$ battery are instability/degradation of non-aqueous electrolytes and the high overpotential (low-efficiency round trip) due to the slow kinetics of OER / ORR reactions, which causes side reactions that lead to poor reversibility and poor life cycle. The major issues for non-aqueous systems are electrolyte decomposition, moisture contamination, and the high polarity of the charge and discharge processes [44-46].

One of the cathode challenges is the accumulation of reaction products, reducing oxygen's limit absorption and transport, and the lack of a consistent three-phase electrochemical surface, which is directly examined by the air electrode's structures and materials. It is now widely acknowledged that carbonate-based electrolytes are very unstable in the existence of $LiO_2$ and $O_2$ and thus have been abandoned in favor of more stable electrolytes, such as ILs, TEGDME, and DMSO [47].

While for the aqueous system, the main problem is the fabrication of a water-resistant electrode in which the Li anode is covered with lithium ions conducting solid electrolyte so that it does not interact with water. Because the discharge product, $Li_2O_2$, is insoluble in the electrolyte solution, it will accumulate on the electrode surface. However, to understand the discharge products formed from these electrolytes, more research remains to be done. Since liquid organic electrolytes are used, the main problem in the Lithium-air battery is safety, electrochemical performance, and reliability. In addition, it is in flux and has a volatile and combustible nature.

The battery's discharge is terminated when the $O_2$ transport channels are covered then the electrode pores are blocked. Therefore, to improve the discharge

performance, the development of new electrode structures and materials with optimal oxygen transport channels may alleviate the pore occlusion issues.

In addition, to increase the cell's round-trip efficiency and rate capabilities, much work has to focus on the air cathode, specifically the use of catalysts and alternative electrode materials. The increase in overpotential results in a significant reduction of round-trip efficiency [48]. The cell voltages for ORR and OER are 2.96 V and 3.1 V, respectively, in terms of thermodynamics. The real ORR voltages, on the other hand, are usually between 2.5 and 2.8 V. The OER voltage is higher, frequently surpassing 4.0 volts. Another key difficulty is the restricted electrical efficiency caused by overpotential or polarization degradation at the cathode during charging and discharging. The discharge potential is about 2.5 V, while high charging potentials (4.5 V) are required for the porous carbon electrode [49]; Because of the large gap between these two values, the round-trip efficiency is low.

Not only pure $O_2$, but the biggest pressure to overcome is also electrode stability in an ambient environment. If fully discharged, the life cycle of a $Li$-$O_2$ battery is restricted towards less than ten cycles, and its coulumbic efficiency is extremely poor. However, by applying effective catalysts, an improvement in this efficiency can be expected. Since trace amounts of moisture can degrade lithium metal, the main difficulty here is to isolate the electrochemical system from moisture in the air.

However, recent reports question the efficacy of electrocatalysts in a non-aqueous Li-air battery considering the decomposition of the electrolyte solvent; according to the majority of findings, using catalysts improves ORE during charging and ORR during discharge, a significant increase in the round-trip efficiency, thus increasing battery performance [50].

One of the main challenges in developing a Lithium-$O_2$ battery is to reduce the overvoltages during charging. Large overvoltage when charging, even when current densities are relatively low, can result in extremely low round trip efficiency ($<60\%$), short lifetime, and poor power capacity [51].

There are problems with using lithium metal as an electrode, involving limited coulumbic efficiency and uncontrollable lithium dendritic growth while cycling. In addition, dendritic growth may shorten the batteries. However, dendrite formation of lithium metal is formed in anode material in the Lithium-air battery due to its high specific energy (11,680 Wh $kg^{-1}$), low negative potential, and deficient weight [52].

In a non-aqueous Li-air battery, the interactions at interface between the electrolytes and the lithium anode become more complex because of the oxygen, by-products, water junction. Therefore, it is often important to protect the Lithium anode with passivation films or suitable electrolytes.

Carbon was mainly used for the porous cathode in the lithium-$O_2$ battery. Pore blockage is the major current problem in developing Li-$O_2$ batteries at the cathode. A serious problem of incomplete discharging due to clogging of a porous carbon cathode with a discharge product such as lithium peroxide resulting in reduced cyclability and efficiency of batteries to provide the necessary lithium ions [53].

It is important the liquid electrolyte easily penetrates the pores of the air electrodes. The diffusion of oxygen is limited while the pores at the air electrode are entirely filled with liquid electrolytes. This results in high polarization, safety issues from anode corrosion, poor reversibility, and poor rate capability due to electrochemical reactions that depend only on the dissolved oxygen in the electrolyte. This also prevents these batteries from spilling into the surrounding humid air. The porous electrode of Li-$O_2$ batteries should support the diffusion of oxygen gas so that oxygen is transported to the electrolyte/electrode interface as far as possible through the gas phase instead of slowly diffusing into the electrolyte [54].

Due to the electrolyte decomposition result, the most byproducts, at a non-aqueous battery, the pore occlusion by $Li_2O_2$ (lithium peroxide) was less problematic.

### 3.2.1. Electrolyte

In the Li-air battery, electrolytes were utilized to mitigate $Li^+$, oxygen gas is reduced, transported to reaction sites, and the lithium anode must be preserved. In the beginning, organic carbonates were applied to the Li-air battery, and they achieved excellent performance of the batteries. To achieve a long cycle life, the electrolyte is a critical component. However, it was later found that the reactions were due to electrolyte degradation rather than OER-ORR. What encouraged the researchers to explore new electrolytes for a non-aqueous Li-air battery was this finding.

The main challenges to be overcome for non-aqueous electrolyte, stable solvent, and lithium salt and their stability in an oxidation environment are, for the time being, to have good lifecycles. The research stream focuses on electrolytes in a Lithium-air battery in five domains of dimethyl sulfoxide electrolytes, amide-based electrolytes, ionic liquids, ether-based electrolytes, and sulfone-based electrolytes.

The ideal non-aqueous electrolytes in Li-air batteries composed of the following elements: - To effectively transport oxygen, it must be highly soluble for oxygen, there should be no concentration polarization and charge accumulation, and it must be an electronically insulated and well conductive of ions Lithium, it must be thermally stable, it must be chemically compatible with the battery electrodes, and it is components, and the overvoltage window must be stable.

As an alternative to organic carbon, ethers attract a lot of attention due to their safety, low volatility stability, a good wetting property of electrodes, towards reduced $O_2$ and $Li_2O_2$, and low cost. They resulted in this impaired recycling performance due to carbonate-based liquid electrolyte solvents, including ethylene carbonate and propylene carbonate, which were initially applied in a non-aqueous Lithium-air battery.

However, after long cycles, electrolyte decomposition is still presented in an ether-based electrolyte such as $HCO_2Li$, $CH_3CO_2Li$, and $Li_2CO_3$. Some ethers including

dimethoxymethane($CH_3OCH_2CH_2OCH_3$;DME), tetraglyme($CH_3O(CH_2CH_2O)_4CH_3$), polythyleneoxide (PEO), and tetraethylene glycoldimethyl ether (TEGDME) [55].

Resulting in the high stability concerning superoxide anions and oxidative potentials, TEGDME has been widely used and is an ether-based solvent. Despite the disadvantages, the most used electrolyte in non-aqueous Li-air systems is still ether-based electrolyte.

Another solvent is dimethyl sulfoxide (DMSO). However, the chemical reaction between $Li_2O_2$ and DMSO can decompose to $DMSO_2$ and form LiOH and thus affect the reversibility. Therefore, in recent years, other organic electrolytes in the Lithium-air battery have also been investigated, such as ethyl methylsulfone (EMS), dimethyl sulfoxide (DMSO), and dimethylformamide (DMF) [56].

In the electrolyte system, lithium salt selection also plays an important role. Peng and colleagues reported a very stable secondary air lithium battery among all potential electrolytes with DMSO / $LiClO_4$ as an electrolyte and nanoporous gold as a cathode. To enable ion transport, the ideal lithium salt should be neutral to the solvent and other battery constituents and have a high solubility in the solvent, especially toward the oxygen reduction reaction [57].

The salts commonly deployed in non-aqueous Li-air cell are $LiCF_3SO_3$, $LiPF_6$, lithium bis(trifluoromethanesulfonyl)imide (LiTFSI), and $LiClO_4$. A redox mediator, tetrathiafulvalene (TTF), was introduced at the downstream stage to reduce the high charging potentials by the same group. To stabilize the electrolyte, it is important to compatibility the solvent with lithium salts. However, batteries can only be charged to 4 V due to DMSO instability, or the electrolyte will degrade [58].

Ionic liquids (ILs) are another electrolyte candidate for a Lithium-air battery. Ionic liquids possess many advantages; it is liquid salts at room temperature, including non-flammability, large comparable electrochemical windows, stable chemical property, importantly low vapor pressure, and low toxicity.

In 2005, the first research by Kuboki and colleagues on ILs was reported in the Lithium-air battery, applying EMITFS electrolytes to demonstrate the applicability of ILs in a Lithium-air battery. Then, promising performance from Lithium-air was presented using ionic fluids that were used as mixtures with other organic solvents or electrolytes alone. However, further investigations are required for further applications, as the high viscosity of ionic liquids impeded their application in the Li-air cell [59].

### 3.2.2. Lithium anode

Due to energy density, high weight cathodes, and electrolytes controlling the total mass, the low specific capacitance of the interpolation-based anodes is acceptable for a Lithium-ion battery. Furthermore, lithium is the lightest element of the alkali metals, and among all the metals, it has the smallest atomic radius due to its fast transport nature and high capacity [60].

However, the lithium metal anode can provide the capacity requirement for an air cathode with an specific capacity of 3862 mAh $g^{-1}_{Li}$. The lower weight of the Lithium-air cathode requires a more energy-dense anode. Like other alkaline metals, lithium reacts slowly in dry air and has high reactivity.

Safety concerns grabbed global headlines, while the high energy density of lithium metal makes it an attractive anode. Upon the discharge, the anode oxidizes to release lithium ions to the electrolyte providing ionic conductivity as it reacts with reduced oxygen on the cathode surface, forming $LiO_2$. With a tiny amount of water, lithium rapidly oxidizes.

The main cause for concern is dendrites; it can cause a malfunction that strongly reacts with contaminants in the battery leading to thermal runaway and fires. Among all the currently known electrode materials, the lithium anode has the most negative potential. When an organic electrolyte is applied to the lithium metal, an automatic and instantaneous thin film consists of a conductive Lithium-ion known as the solid

electrolyte interface at the interface, creating a corrosion-resistant lithium salt barrier, as in the schematic diagram (Figure 3.4.) [61].
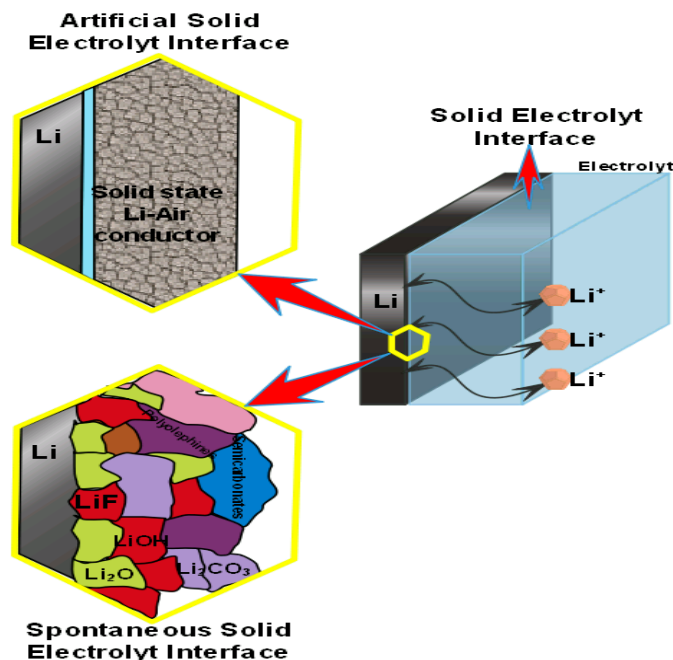


Figure 3.4. shows a schematic diagram of Li-metal electrolyte interface options. The complex of a synthetic solid electrolyte interface is formed by reducing the electrolyte and a natural solid electrolyte interface, such as a ceramic conductive of a lithium ion.

The instability of the lithium metal encountered an electrolyte (inorganic and polymer electrolyte, non-aqueous and liquid-liquid electrolyte) in a rechargeable battery is due to the high reactance and extremely low potentials. Hence, these safety concerns must be addressed before the mass production of commercial Lithium-air batteries [62].

During the charging and discharging of batteries, the lithium anode passes through plating and stripping, causing defects in the brittle nature of the solid electrolyte interface. However, to obtain a good reaction, a $Li^+$ is required. During plating, preferential precipitation will be generated from the lithium metal, forming the dendrites and thin films by the irregular deposition resulting from the uneven distribution of the current at the interface of the metal with electrolyte.

### 3.2.3. Cathode

The cathode of a Lithium-ion battery is fundamentally different from that used for a Lithium-air battery. Many cathodes have been used so far for the Lithium-air cell. The porous cathodes, which are where reactions happen throughout the charging and discharging operations, are the most important part of a Lithium-air battery. For a non-aqueous Lithium-air cell, an active electrocatalyst is essential, but if the conductivity is low and the volume change is large during the cycling processes, this will impede the battery performance improvement [63].

During the Lithium-air battery cycle, instead of the intercalation reaction, as in Lithium-Ion, the discharge products formed and decomposed on the electrode's surface, especially $Li_2O_2$. Lithium-air cathodes' most common porous conductive material is carbon because of its easily adjustable surface area, high electronic conductivity, pore sizes, and low cost [64].

In the Lithium-air cathode, the reason for the termination of the discharge reactions is that the oxygen limits exposure to the inner side of the electrode due to pore blockage and volume reduction caused by the discharge residue covers on the surface of the electrode carbon material.

In Lithium-air systems for cathode materials, porous carbon with and without various catalysts has been frequently used. Therefore, to determine the discharge performance, a key element is the design of the Lithium-air battery electrode [65].

This work explores the synergistic effect between metal and metal oxide doped graphene and investigates a series of nanocomposites of graphene saturated with palladium, ruthenium, and $\alpha$-MnO$_2$.

The following characteristics should be in an ideal cathode: to provide a three-phase interphase oxygen-cathode-electrolyte, transport channels for rapid diffusion of oxygen, and form the discharge products sufficient space [66,67].

The carbon usually showed good initial discharge capacities but a poor life cycle. Due to the low prices and abundance of carbon black products, They have been utilized for many years as cathode materials [68]. Besides carbon as the cathode material of the Lithium-air battery, various other carbon structures such as graphene and its derivatives, mesoporous carbon, and carbon nanotubes (CNTs) were investigated.

To increase ORR-OER activity, a Lithium-air battery cathode generally includes a mixture of catalyst, carbon for a high surface layer and gas diffusion, a binder, and a current collector. For Lithium-air batteries, carbon nanotube cathodes are attractive due to the possibility of making a freestanding cathode consisting of only carbon nanotubes, which eliminates the need to increase the weight of the bonding materials. Hence, considerable work has been done in researching new materials and designs for cathodes. For an electrode in a Li-air system, Ding et al. used Various carbon materials, as shown in (Figure 3.5.) the initial discharge/charge voltage profiles.
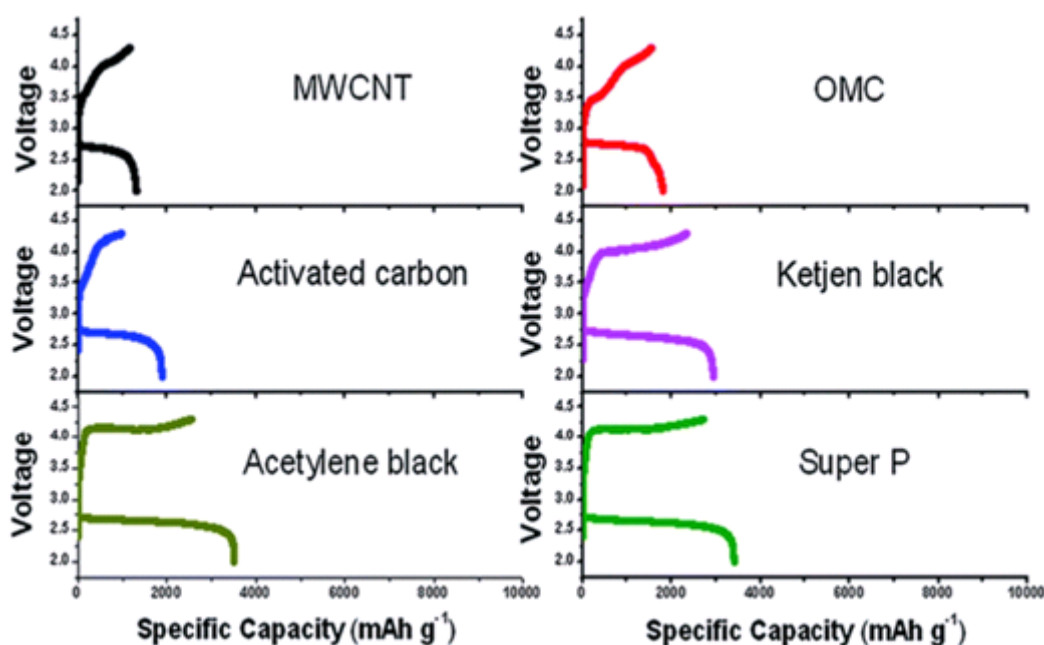


Figure 3.5. The full charge and discharge profiles of different carbon materials [33].

The mesopores' specific surface area was the most important measure for evaluating the battery's performance that determined the parameters that were found to have an

impact on the battery's performance. At the same time, the oxygen-carrying functions, introduced during contact with air or by heat treatment after pyrolysis, had low or no effect on the efficiency of batteries.

According to Ding et al., Multy Wall Carbon NanoTube provides 1300 mAh $g^{-1}$ capacity, followed by Ketjenblack, Acetylene Black, and Super P electrodes with a discharge capacity of 2865, 3512, and 3399 mAh $g^{-1}$, respectively.

Cathode materials like metal oxide, TiC, carbon nanotubes, and gold have been explored to improve cycle life and battery capacity. Moreover, several research efforts have been dedicated to enhancing Li–$O_2$ batteries' performance like; more stable cathode materials have already been used to avoid or reduce side reactions related to the decomposition of the electrode. Instead of classical organic electrolyte, have been used the solid-state and hybrid electrolyte to avoid attack by radicals of $O_2$, the carbon dioxide, and moisture has already been studied to understand a true ambient air of Li-air batteries, various efficient catalysts have been launched to boost the kinetics of $O_2$ evolution reaction and the oxygen reduction reaction upon the charge and discharge states [69].

Hence, in overall performance, the cathode structure plays a vital role in Lithium-$O_2$ cells. According to Wang, the cathode of hierarchically porous carbon, under oxygen, came with the stable performance of primary discharge of 11,060 mA $g^{-1}$, but with a constant life cycle of about 2000 mA $g^{-1}$ for 10 cycles [70].

However, in classical Li-$O_2$ cathode, the transfer of both oxygen gas and electrolyte happens within the carbon porous parts framework, which could result in unutilized of cathode active sites.

Moreover, the binders like PVDF (Polyvinylidene Fluoride), which are mostly utilized in the cathode, chemically react with some discharge products, for example, $Li_2O_2$, LiOH, $LiO_2$ and can decay the cycling performance. However, several reports have suggested a hydrophobic and free binder, densely packed 3D membrane of

graphene as an efficient cathode for the reversible and stable operation of lithium-$O_2$ batteries under ambient conditions [71].

The materials of cathode that are used in the non-aqueous lithium-$O_2$ battery must be a structure of durable porous in order to provide oxygen diffusion channels and store the discharge product. To meet the requirements for ion transport, the cathode must also have a high wettability over the discharge and charge operation.

Another important thing, the materials of cathode included catalyst, must have the capability to speed up OER and ORR kinetics [72]. The ideal material for cathode with optimized crystal forms, morphology, and structure can provide more space for discharge product storage and simplify the formation of electrode wettability and oxygen diffusion while improving its catalytic performance via OER and ORR due to the introduction of vacancies and defects [73].

The materials of carbon are used as upholding catalyst, electrode materials, and conductive agents in supercapacitors, fuel cells, and Li-ion batteries due to their large surface areas and perfect electrical conductivity.

In these years, the carbon materials field application has been reached for use in the lithium-$O_2$ battery as cathode materials and because of their convenient feature, so its interest is increasing all over the world. In non aqueous lithium-$O_2$ battery, generally, the carbon materials serve as air electrodes to produce a cathode with high porosity and act as catalysts for OER and ORR [74,75].

Graphene is a hexagonal-shaped crystal structure made up of a densely packed monolayer of carbon atoms. Since the discovery in 2005 of graphene by Novoselov et al., it has received quite an interest as a carbon candidate. Graphene has been broadly explored as an anode material in Li-ion cells and a metal-free catalyst or catalyst support in fuel cells because of its large surface area, advantages of high electron transfer rate, chemical and thermal stability, as well as high conductivity [76].

In recent days, graphene showed extraordinarily high discharge capacity and cycle efficiency as a promising air electrode in Li-$O_2$ batteries [77,78]. Although particular processes for the OER & ORR onto graphene in the nonaqueous lithium-$O_2$ battery remained not clear at the time, the features of graphene were pointed out to its unique structure and the ideal 3-phase electrochemical area as well as its oxygen and electrolyte diffusion channels [79,80].

Carbon nanotubes: recently, carbon nanotubes have been investigated, including multi walled carbon nanotubes and single walled carbon nanotubes, for cathode materials as a nonaqueous lithium-$O_2$ battery due to their high conductivity causes their unique structures, high flexibility, heat resistance, and thermal conductivity.

Minerals and metal oxides: to reduce the electrode overvoltage in the cathode of the lithium-$O_2$ battery, metal and metal oxides have been exceedingly utilized for catalysts during discharge/charging process and improve the overall battery performances. So far, the metal and metal oxides examined as catalysts could be categorized along with the transition metal oxides and metals [81]; Oxides of precious metals and metals; perovskite and perovskite oxides related; and manganese oxides.

Manganese oxides are the most effective catalyst that has been utilized in previous research in the cathodes of lithium-$O_2$ batteries, manganese oxides can increase the specific discharge capacity, and they can also enhance the batteries' recycling efficiency [82].

In recent research, manganese dioxide is generally applied as a marker to display for high and active catalysts; they are also utilized as cathode catalysts in the study of cathode mechanics and electrolyte performance [83]. Moreover, manganese dioxide would also function as a prominent key in composite materials [84,85].

In 2006 Ogasawara et al. electrolytic manganese dioxide was applied for the cathode of the Li-$O_2$ cell [86]. In addition, the same group investigated the comparison of the

performance of different manganese oxides as cathode catalysts, like commercial manganese dioxide, $Mn_3O_4$, $Mn_2O_3$, $\gamma$ $MnO_2$, and $\lambda$-$MnO_2$, both -$MnO_2$ and $\alpha$-$MnO_2$ in nanowires and bulk shapes. The nanowires of $\alpha$-$MnO_2$ can have the maximum discharge capacity 3000 mAh $g^{-1}$ at a discharge potential of about 2.6 V and a current density of 70 mA $g^{-1}$ and a charge potential of around 4.0 V versus $Li^+$: Li. Subsequently, several studies were done on manganese oxides as the active catalyst in a lithium $O_2$ cell.

Generally, manganese oxides occur in many crystalline forms, like the three-dimensional spinel phase, the two-dimensional structure, and the one-dimensional tunnel.

In the published literature, several intensive researchers have confirmed that the device's electrochemical performance can be highly influenced by the morphology and crystal phase of manganese oxides used. In lithium-$O_2$ battery as the most overly investigated manganese oxide, $MnO_2$ and various forms have been broadly classified as cathode catalyst in different crystal stages [87,88].

# CHAPTER 4. GRAPHENE-BASED CATHODE MATERIALS

## 4.1. Graphene

Since graphene's discovery sparked widespread interest, researchers have concentrated on the material's unique electrical structure, where charge carriers simulate relative massless particles. However, the physical graphene structure made entirely of two dimensional (2D) carbon atomic sheet is a colossal attempt to develop dependable strategies for obtaining mass amounts of this extraordinary substance [89].

Graphene is made up of a single layer of densely packed carbon atoms that forms a crystal lattice in the shape of a honeycomb. On the one hand, the hitherto established methods, separation of graphite in organic solvents, superaxial growth on silicon carbide, as well as CVD (chemical vapor deposition) of hydrocarbons onto transition metal interfaces, most notably the micro mechanical cleavage of graphite, present difficulties in obtaining large processing quantities of Graphene sheets, which hinders the utilizing all of its great features to the greatest extent possible. On the other hand, however, graphene showing a high crystalline purity that electrons can move sub micrometer distances with no dispersion appears to be a precisely 2D material [90,91].

rGO (reduced graphite oxide) is the promising alternative, easily scalable, and low cost, which is a layered material whose constituent layers of graphene with hydroxyl and epoxy groups are easily peeled off in the water [92].

According to experiment and theory, perfect 2D crystals are unable to remain in their natural state. However, the resulting monolayers of graphene oxide (GO) may be

placed at a controlled density on a wide range of substrates, allowing for the creation of conductive thin films on both ductile and brittle surfaces [93].

Nonetheless, the chemical reduction of graphene oxide near to being an insulator can improve the conductivity by up to four orders of magnitude, and the conductivity achieved thus far for rGO (reduced graphene oxide) lacks that of the original graphene a factor of 10:100. Furthermore, according to the theory, many experiments with thin films less than a certain thickness of tens of atomic layers have demonstrated that films become thermodynamically unstable unless they form an intrinsic part of a 3D system. There is a general consensus that through residual functional groups, the lowest electrical performance of graphene oxide remaining after reduction arises.

Graphene synthesis: since the first papers of Jim and Novoselov in 2004, Graphene has been the focus of several scientific studies, some of which were nominated for the Nobel Prize in Physics in 2010 and garnered much media attention.

As early as 1919, the first methylation of Graphene oxide is a material that can be used in a variety of applications, which appeared in the literature, and the scientific study of ultra-thin multilayer carbon came next. Graphene's single as a practically achievable material has been in use since 1962. The extraordinary physical properties of graphene, such as its extraordinarily heat resistance conductivity and tremendous strength, were studied using this catalyst of interest [94].

In 1924 the hexagonal structure of the entire layers of graphite was resolved by Bernal, and to measure the spacing between cleavage levels in graphite, Braggs used powder X-ray diffraction. Many inspired by the transparency, along with the flexibility and excellent electrical conductivity of the graphene sheets, envisioned graphene's prospective applications, which including wearable and aggregate electronics, as well as plenty of more applications in the actual world where graphene might find useful, such as polymer compounds, transparent electrodes, and energy storage materials.

One of the many carbon allotropes that are becoming more common is Graphene. Graphene synthesis can be classified into two types of approach; Bottom to top and top to bottom. The fabrication of graphene by bottom-up approaches involves alternative carbon sources, while the Top-down methods involve dismantling the stacked graphene layers to produce single sheets of graphene.

Graphene has many superior physical properties in addition to its electronic properties, so it has been used in corrosion inhibitors, in polymer compounds, in photoelectric cells as a transparent conductor, and in biological and chemical sensors [95].

The separation of the stacked sheets in top-down ways means that the forces that bind the sheets together (van der Waals) must be addressed; although the bonding energy between the layers is relatively low, it is not an easy task. The highest known elastic modulus shared with carbon nanotubes is the strong $sp^2$ bonds that each sheet should be bound together give graphene, and the thermal conductivity of graphene exceeds that of the diamond.

In this field, effective challenges include splitting the layers without destroying the graphene sheets and keeping the graphene sheets from being damaged and agglomerating graphene sheets again once the layers are peeled off. Graphene market improved devices were close to taking off but, up to this point, has hit the wall of graphene cost-synthesis, which is still inefficient alongside commercial purposes [96,97].

In general, the top-down method suffers from low products, many steps, and natural graphite has a common disadvantage and is a limited resource, and it requires mining and processing before use [98]. Graphene is synthesized from graphite. Since graphene is composed of a sub-component of graphite, direct separation from mass graphite would be the simplest and oldest method for its production [99].

For the bottom-up approach, high levels of the graph have to be optimized to assemble high-quality materials; as a result, these techniques usually necessitate high temperatures. It's worth noting that not all graphite was made equal in the beginning. Compared to the top-down approach, the procedures involved are usually straightforward, and the synthesized material can contain higher degrees of flaws. There are two important types of graphite, synthetic and natural.

The preparation of graphene nanostructures has been conducted by other methods such as the bottom-up approach. It can be used to construct large films of graphene sheets by growing on specific substrates. The peel-off or scotch tape is a mechanical cleavage method that involves peeling off graphite with duct tape to separate the sheets. It would be the first method of graphene isolation that was used.

Bottom-up methods:

1. Chemical vapor deposition.

2. Miscellaneous methods.

3. Epitaxial growth on silicon carbide.

Top-down methods:

1. Arc discharge.

2. Solvent-based exfoliation.

3. Micromechanical cleavage.

4. Exfoliation of graphite intercalation compounds.

5. Unzipping carbon nanotubes.

6. Electrochemical exfoliation.

7. Exfoliation of graphite oxide.

Benjamin Brodie, in an effort, measured the atomic weight of carbon; In 1859, he was one of the first individuals to do tests on the graphite chemical reaction. Reducing and exfoliating graphite oxide is the process for creating graphene that has gained the most attention. Benjamin Brodie observed that graphite would be extremely oxidized by repeatedly presenting it for several days to a mixture of potassium chlorate and nitric acid.

Historically, nearly a century later, while modifications to methodologies have been proposed for the first time, the Hummers method still is the most broadly used procedure. For example, graphite oxide has been synthesized by oxidizing graphite using strong oxidizers and concentrated acids in the Straudenmaier, Brodie, or Hummers methods [100]. At the end of his trials, he got a pale yellow material containing shiny, translucent sheets and went on to evaluate many of the properties of what we today call graphite oxide, which he called graphite acid.

Many different measures have been used to describe the structure of graphite oxide, and Dreyer et al. have also discussed it. The Lerf Klinowski model is a generally acknowledged model that graphite oxide describes with a sheet structure with epoxy and hydroxyl groups at base levels and carbonyl and carboxyl groups at the edges of the plate.

It is still a preferred method for in vitro to produce graphite oxide, Hammers. Graphite oxide is hydrophilic because of these oxygen groups and the existence of functional groups between the sheets depending on the amount of divided water also leads to a greater spacing between the interlayer of graphite oxide 6-12 Å than graphite 3.4 Å.

Plant extracts are used to reduce graphene oxide: In general, graphene oxide reduction involves using a poisonous and toxic substance which, regrettably, may be a major obstacle to the ability of this process to produce large quantities of graphene.

Hammer's approach using oxidants and concentrated acid remains the most productive procedure for producing GO (graphene oxide). However, the use of a hydrazine reducing agent, for example, despite the true result in a higher rate of oxygen removal from graphene oxide, may end up putting the workers' health in jeopardy but also lead to serious environmental problems if the applied reduction stage solvent is accidental in land or water source without a pre-set system for wastewater treatment. However, the main problem is the prepared GO sheets reduction to the rGO (reduced graphene oxide) for practical applications.

Many researchers working on plant extracts to meet this challenge have reduced graphene oxide to replace hydrazine with plant extracts as a major reducing agent. The traditional approaches of reducing graphene oxides, like chemical methods or thermal annealing, have been used several times. Plant extracts, due to its simplicity, are a viable possibility for future graphene oxide reduction, they are green sources, and with the necessary application of the synthesis process, they may provide a similar or greater average decrease than hydrazine. However, chemical reduction has disadvantages, like its high price, toxic nature, and harmful influences on both the user's body and the environment that make its use unfavorable. Extracts from plant parts such as leaves or roots can potentially reduce oxygen groups on the surface of graphene oxide.

Nevertheless, the problem of selecting a graphene oxide reducing agent and the hydrazine widely used is regrettably toxic, and thus the use of green reducing agents like bacteria, fungi, and plant extracts has been attempted and reported in multiple publications [101]. In addition, the high content of menthol and other content in some plants is useful as a reducing agent.

These plant extracts have no environmental effect, and in comparison with chemical reducing agents, they are available, cost effective, and have a suitable effect of reduced graphene oxide. Therefore, we believe that at least one content of these plant extracts can worthily reduce GO to rGO.

## 4.2. Graphene-Based Nanocomposites

Nanocomposites made of graphene have been studied extensively and used in Supercapacitors; for example, they are used in a variety of applications [102], energy storage [103], optical electronics [104], photovoltaic cells [105], as well as sensors [106]. Song et al. have reduced graphene oxide on Ni foam by a hydrothermal technique. Then, to increase the catalytic activity of graphene, the nanoparticles of Pd were electrodeposited to the rGO multi sheets. The rGO/Pd nanocomposites that were created showed excellent stability and performance for reduction of $H_2O_2$ [107].

Jeong and colleagues investigated the effecting cause by Pd, Pt, & Ru catalysts supported with rGO to the Li-air energy system, finding a significant reduction in charge overpotentials as well as strong cycle stability [108]. Furthermore, Because of the huge surface area of graphene support, the well built interaction among the $O_2$functional groups of the surfaces layers of graphene and catalysts may result in reduced accumulation and more dispersal into the catalyst on GO [109]. This improved connection results in Graphene's Fermi level changes, increasing catalytic activity [110]. According to the Shao-Horn team, OER & ORR because of their differences, they demand distinct catalysts according to it's differing actions processes, and Au & Pt were highly efficient in OER & ORR, in order [111].

As a result, numerous experiments have been conducted in order to develop bifunctional catalysts with better capacity and a lower possibility for fullcharge-fulldischarge [112]. Thapa and his team., for example, used a rechargeable lithium-air battery with a α-$MnO_2$&Pd catalyst as an air electrode energy storage and achieved strong of the reduction and the oxidation activity and non of by reaction

[113]. Guo et al. used graphene to decorate PtFe nanoparticles to enhance ORR's stability and catalytic activity [114].

# CHAPTER 5. EXPERIMENTAL SECTION

The compositions of all electrodes produced within the scope of the thesis are given in Table 5.1. As carbon materials are unstable in high charge voltage, which decomposed into lithium carbonate, catalysts with different weight % were applied to evaluate the electrochemical performance of electrodes. Besides, urchin virus-templated $\alpha$-MnO$_2$ nanowires were prepared to understand the impact of morphology on Li-O$_2$ cell performance.

Table 5.1. Composition of electrodes produced within the scope of the thesis.

| Electrode Composition | Graphene contents | Metals contents | $\alpha$-MnO$_2$ contents |
|---|---|---|---|
| Reduced graphene oxide | 100% | - | - |
| Ru/ $\alpha$-MnO$_2$ | - | 5% | 95% |
| Reduced graphene oxide /Ru/ $\alpha$-MnO$_2$ | 50% | 3% | 47% |
| Reduced graphene oxide /Pd | 75% | 25% | - |
| Reduced graphene oxide / $\alpha$-MnO$_2$ | 75% | - | 25% |
| Reduced graphene oxide /Pd/ $\alpha$-MnO$_2$ | 50% | 25% | 25% |
| Reduced graphene oxide /Virus-templated $\alpha$-MnO$_2$ | 75% | - | 25% |

## 5.1. Preparation Of Graphene Oxide And Reduction Of Graphene Oxide

From natural graphite powder, GO was synthesized by applying the modified Hammers method. In brief, 1 gram natural graphite flakes were dispersed in 50 milliliter H$_2$SO$_4$ concentrate in a flask (equation 5.1). Then, 1 gram NaNO$_3$ was added to the mixture with constant stirring at 660 rpm. The flask is transferred to an

ice bath in order to maintain the reaction temperature between 1 to 4 °C. After that, 6 gram $KMnO_4$ is added slowly by controlling the temperature of the mixture (equation 5.2, 5.3).

$$2H_2SO_4 + C \longrightarrow 2H_2O + CO_2 + 2SO_2 \qquad (5.1)$$

$$KMnO_4 + 3H_2SO_4 \longrightarrow K^+ + MnO_3^+ + H_3O^+ + 3HSO_4^- \qquad (5.2)$$

$$MnO_3^+ + MnO_4^- \longrightarrow Mn_2O_7 \qquad (5.3)$$
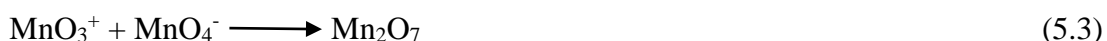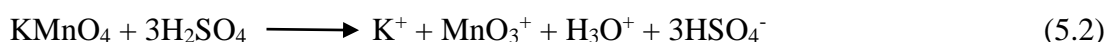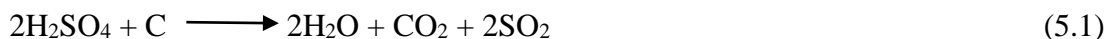
The resulting mixture is then stirred at 660 rpm for 20 minutes inside a freezing bath. Afterward, the solution is warmed to 36 degrees celsius and mixed overnight until a thick paste is formed. Then, the solution is transferred to an ice bath again and 48 ml of double-distilled (dd) water is added dropwise while stirring. After stirring the solution for 20 minutes at room temperature, a dark brown slurry was formed. Finally, 102 ml dd-water is added and subsequently, 10 ml 30% $H_2O_2$ is added into the mixture. By adding 10 ml of $H_2O_2$, a permanent yellow color is observed (Figure 5.1.) that shows the complete oxidation of graphite. The final solution is centrifuged and washed with 15% hydrochloric acid, then filtered and washed with dd-water several times until the pH is 5 and dried under vacuum at 70° C overnight. Graphene oxide is obtained as the final product.

Reduction of GO was completed by adding the various reducing agents ($NaBH_4$, Hydrazine, and Salvia O. extract for comparison). The suspension was refluxed overnight at 70 °C. The final product was filtrated, washed, and dried in an oven at 50 °C for 24 h. FESEM shows the changes in exfoliation graphite to reduced graphene oxide in Figure 5.2.
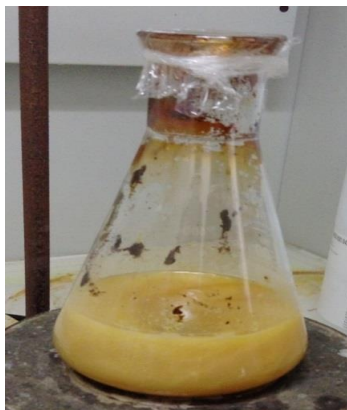
Figure 5.1. The yellow slurry of Graphite Oxide product after adding $H_2O_2$.
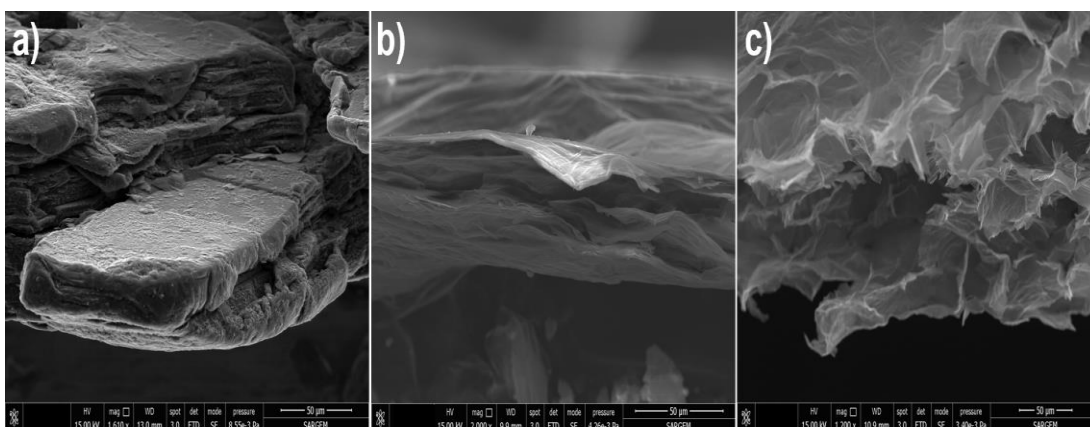


Figure 5.2. The exfoliation of graphite (a) to graphene oxide (b) and reduced graphene oxide (c).

## 5.2 . Hydrothermal Method For Producing α-MnO₂ Nanowires

300 mg of $KMnO_4$ and 500 mg of manganese sulfate ($MnSO_4.H_2O$) were used to fabricate α-MnO₂ nanowires where 39 mL d.d. $H_2O$ was added and swirled upto 120 min. The resulting brownish slurry were then put in the microwaved for 0.5 h upto 139.5 ºC. The end result were filtered and rinsed 3 times after cooling. The material were heated to dried @ 59.5 ºC for 16 h. α-MnO₂ particles were produced after they've been ground by hand using a mortar.

$$MnSO_4 + KMnO_4 + H_2O \longrightarrow MnO_2 + K_2SO_4 + H_2SO_4 \qquad (5.4)$$

### 5.3. Preparation Of Graphene Incorporated With Ru And α-MnO₂ Nanowires

The α-MnO$_2$ nanowires were synthesized via the hydrothermal method, as described in section 5.2. Then, 50 mg as-prepared α-MnO$_2$ product 50 mL was sonicated of distilled water and stirred at room temperature. Poly acrylic acid (PAA, Mw: 2,000 g mol$^{-1}$) was added and stirred overnight. PAA was applied to nucleate the metal nanoparticles and prevent agglomeration. The PAA-wrapped α-MnO$_2$ nanowires were collected and washed by centrifugation and dispersed again with 100 ml of distilled water. Ru precursor solutions (ruthenium (III) chloride, 20 ml of 10 mM) were added into the previous solution, and to reduce the metal ions, 3 ml of 100 mM NaBH$_4$ was dropwise added and stirred overnight at room temperature. The solution was vacuum filtered and washed with dd-water, and freeze-dried. A control experiment without PAA wrapping was performed to investigate the effect of PAA in the aggregation of nanoparticles.

Next, 50 mg rGO and 50 mg Ru/α-MnO$_2$ samples were ground with mortar and pestle. Then to enhance the bonding among rGO & α-MnO$_2$/Ru, ball milling was performed. The obtained nanocomposites were stirred in 100 ml water overnight. The product was washed through vacuum filtered, and freeze-dried.

### 5.4. Preparation Of Graphene Incorporated With Pd And α-MnO₂ Nanowires

The first step is, Pd was used to adorn GO sheets in the following way: A homogenous brown dispersion was achieved by sonicating the as-prepared graphene oxide (60 mg ml$^{-1}$) in 50 ml d.d. water. The GO solution was then given 25 mg of palladium (II) chloride (PdCl$_2$), followed by a dropwise addition of 1M NaBH$_4$ inside an ice bath, to be precise. After that, the solution was stirred at 25 ℃ for 16 h.. Finally, filtered, rinsed, and freeze-dried the finished product.

The resulting rGO@Pd & α-MnO$_2$ nanowires were then weighted to yield 75 wt% rGO@Pd and 25 wt% α-MnO$_2$, then sonicated in d.d. H$_2$O and stirred for 18 h. A

mechanical alloying approach was used to increase mechanical bonding between rGO/Pd & $\alpha$-MnO$_2$ nanowires.

## 5.5. Incorporation Of Virus-Templated $\alpha$-MnO$_2$ Supported On Graphene

Before growing M13, it is fundamental to advise the suitable safety data sheets, materials and tools, and the lab's Environmental Safety and Health place for appropriate treatment of hazardous materials and equipment utilized in the culturing procedures.

Purification and reproduction of M13 phages were performed to prepare the MnO$_2$ virus template. E.coli ER2738 (New England Biolabs Inc.) was used as a bacterial host for M13 virus infection. Virus replication was carried out by culturing 60 μl of Escherichia coli overnight in an incubator with 6 μl of M13 virus from stock (ATCC® 15669¬B1™) within 60 ml of Lennox broth (LB) contains tetracycline (0.06 g L$^{-1}$) and incubated at 36 °C for 19 h in a shaking incubator (190 rpm).

The medium of LB was included, 6 g L$^{-1}$ sodium chloride (pH 7.7), and 6 g L$^{-1}$ yeast extract 12 g L$^{-1}$ tryptone. For 9 min at 5 ° C centrifugation at 8,880 rpm, bacteria cells were harvested. Discarded bacterial cells were presented at the bottom of the pellet. By transferring the supernatant to a conical tube containing a 2: 8 volume ratio solution containing 21% cooled PEG-8000 / 2.6 M NaCl, the supernatant containing M13 viruses was purified and reversed to mix well. Thereafter, the tubes were preserved at 5 °C overnight. Viruses were precipitated and centrifuged for 22 minutes at 5 °C at 11,500 rpm. M13 viruses are observed as white pellets (Figure 5.2c). The suspension Pellet was dissolved in 2.5 ml of dd water.

Therefore, 2.6 M NaCl / 21% PEG-8000 solution, which is a volume ratio of 2: 8, was added and to mix it well by inverting. Afterward, the tube was incubated for 22 minutes at 5 °C. The tube was centrifuged for 15 minutes at 11500 rpm. Before transfer to an Eppendorf tube, the supernatant was mixed and discarded in 1.25 mL

of Tris-saline solution (TBS, PH 7.7, TBS, 153 mM NaCl, 51 mM Tris-HCl), and stored at 5 °C.

Using a spectrophotometer, the concentration of viruses was determined based on the absorption of phages in ultraviolet light at 320 nm and 269 nm. By the formula below, the virus concentration was calculated:

Virus particles / ml = (6 x $10^{16}$) x (A269-A320) / (the DNA number bases in the genome of virus).

An overnight plaque formation assay determined virus concentrations. By TBS buffer, virus specimens were diluted from $10^7$ to $10^{10}$ with serial dilution. Dilute 100 μl specimens of each were mixed with 200 μl E. coli culture medium containing 6 mM $MgCl_2$ to increase the M13 virus product, gently mixed, and for 15 min incubated at 36 °C. Using an autoclave, 200 mL LB medium was prepared with 15.5 g $L^{-1}$ agar powder and equally poured into Petri dishes.

When the media was solidified, all previously incubated specimens were added to 3.5 mL soft agar and poured onto the media in Petri dishes and incubated overnight at 36 °C. After about 5 to 6 hrs, plaques began to appear, indicating that infection with viruses slows down the growth rate of the bacteria.
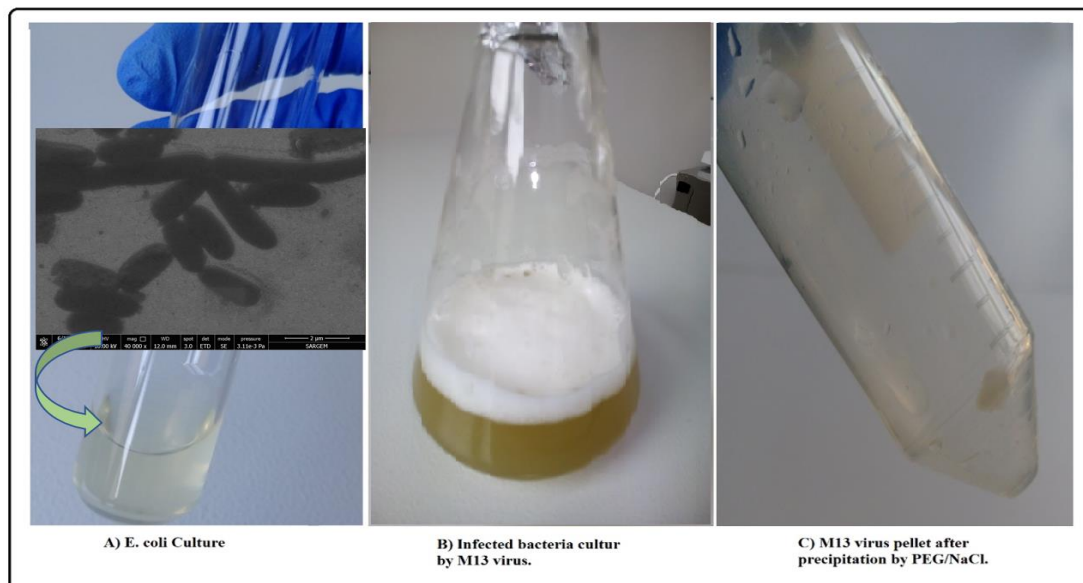
Figure 5.3. Wild-type M13 virus propagation by infecting E.Coli as host.

Virus-templated α-MnO$_2$ nanowires were prepared in a cold incubator, with the virus concentration optimized and the pH of the starting solution regulated to 10 during the reaction. The virus-templated MnO$_2$ was produced by a redox process similar to the one described by the Belcher group [115]. In a 50 ml conical tube, 50 mM manganese sulphate solution was applied to 30 ml DI water (pH fixed to 10) in a conventional synthesis. The wild-type M13 phage (1.2 × 10$^{13}$ pfu ml$^{-1}$) was transferred to the mixture. The conical tube was rotated and positioned on an orbital shaker after the phages were added, then kept at 4 °C overnight. The mixture was then added to a 20 mM potassium permanganate solution, and the conical tube was rotated and incubated at 4 oC overnight. The resulting product was centrifuged at 3000 rpm for 7 minutes before being rinsed with dd water, vacuum filtered, and lyophilized.

25 mg virus-templated α-MnO$_2$ nanowires were added to rGO solution (75 mg ml$^{-1}$) and stirred overnight at 4 °C.

## 5.6. Electrochemical Tests And Cell Fabrication

90 wt.% the as-prepared active materials and As a binder, ten percent sodium carboxymethyl cellulose (CMC) was disseminated in $H_2O$ and physically alloyed for one hour in a Fritch P7 ball mill at 350 rpm (ball to powder weight ratio; 6:1). Then, A doctor blade was used to apply the slurry on the nickel foam current collector. The nickel foam was coated and cured at 90 ℃ in a vacuum oven for 20 h; then, cathodes were collected. The electrodes were cut into 18 mm. The average active material mass loading was around 0.8 mg. The weight of the whole mass of active materials is used to compute the current density and specific capacity.

To investigate the electrochemical performance of the cathodes, ECC air test cells (El-Cell Swagelok) were built in an Ar-filled glovebox (Figure 5.4). In the test cells, the prepared materials were utilized for the cathode, Li foil used as the anodes (precut lithium foil ,15.6 Dia*0.25mm Thick), and the electrolyte was 1M lithium perchlorate (LiClO$_4$, Sigma Aldrich, 99.99 percent) mixed in tetra ethylene glycol dimethyl ether (Sigma Aldrich, 99.0%). The electrodes were charged and discharged between 1.8 and 4.3 V at a constant current of 100 mA g$^{-1}$. Cyclic voltammetry tests for electrodes were carried out with a constant scan rate of 0.3 mV s$^{-1}$ to evaluate the electrochemical reaction of the cathodes. Electrochemical impedance spectroscopy (EIS) of the electrodes was tested before and after full discharge in the frequency range of 1000 kHz to 0.1 Hz with AC amplitude 5 mV to determine the resistance variation after generating discharge product on the cell for further electrochemical characterization.

| 1)ECC Air cell | 2)1st placing Li metal as anode | 3)Seprator | 4)adding electrolyte | 5)Plcing the prepared cathode | 6)Closing the air cell |
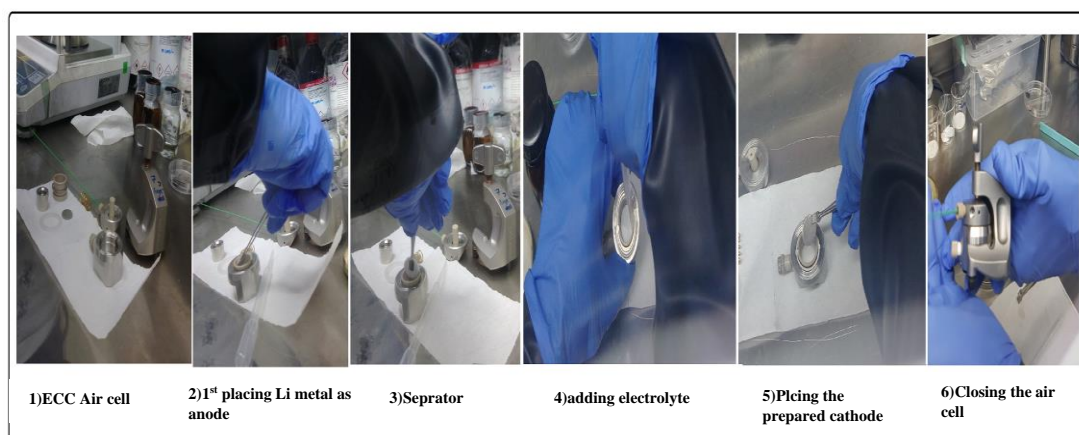
Figure 5.4. The Li-$O_2$ cell assembly.

## 5.7. Material Characterization

Using a field emission scanning electron microscope (FESEM; Quanta FEG 450) and transmission electron microscopy, the surface topography of the developed graphene, graphene-based nanocomposites, and discharge products of electrodes after full discharge were studied (TEM; Hitachi HT7800). The elemental composition of the structures was investigated using energy-dispersive X-ray spectroscopy (EDS). The distribution of hybrid structures in the composite structure was determined using EDS mapping. X-ray diffraction technique (Rigaku D/MAX 2000), Cu-K radiation (= 1.5418 A°) was used to describe phase structures of graphene-based materials and discharge products on the electrode surface. To discriminate GO and rGO in graphene-based nanocomposites and establish the development of discharge products on the electrode surface, Raman spectroscopy (RamanRXN systems with 785 nm laser excitations) was used. The loading amount of metals and $MnO_2$ on rGO sheets was measured by thermal analysis (TG) in an air atmosphere with a heating rate of 5 °C min1 to 1000 °C using a NETZSCH STA 449 F1. The chemical phase of Li, C, and O for discharged electrodes was evaluated using X-ray photoelectron spectroscopy (XPS) (Thermo Scientific K Alpha spectrometer with an Al K X-ray source).

# CHAPTER 6. RESULTS AND DISCUSSION

## 6.1. Morphological And Chemical Composition Study Of Graphene And Graphene-Based Nanocomposites

To prepare rGO various reducing agents have been used. When $N_2H_4$ (hydrazine) was used to reduce graphite oxide, the nitrogen atoms acted as donors to replace p-type pore carriers [116]. The following mechanism was reported by Stankovich et al. to reduce graphene oxide using hydrazine [117].
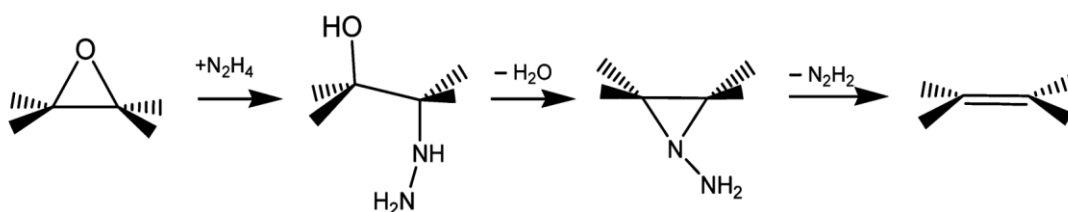


Figure 6.1. Schematic diagram mechanism of GO reduction by the hydrazine.

In sodium borohydride ($NaBH_4$) reduction, the interlayer space is initially expanded slightly via forming intermediate complexes of boron oxide and then contracted by removing the hydroxyl groups and boron oxide complexes with carbonyl groups. Therefore, most epoxy and carbonyl groups can be converted to hydroxyl groups in GO reduction using $NaBH_4$. The mechanism of GO reduction with $NaBH_4$ was proposed by Zhen et al. as follows [118]:
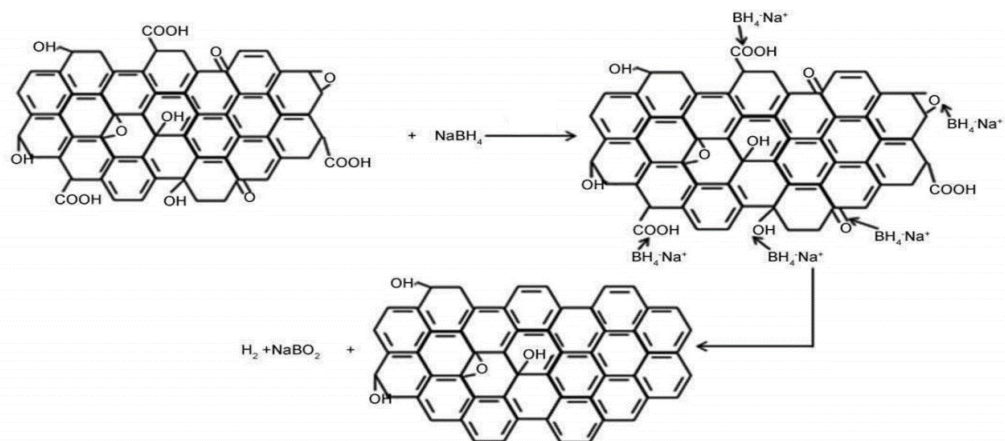
Figure 6.2. Schematic of the GO reduction mechanism by NaBH4.

GO reduction was performed with plant extract (Salvia officinalis plant extract). Salvia O. containing Diterpenes (ursolic acid, carnosol), monoterpines (borneol, beta pinene, alpha pinene, thujone, camphor), phenol acid (lithospermate B, caffeic acid, sulfianolic acid, luteolin 7-O-glucoside, rosmarinic acid), flavonoids (Hispidine, Apigenin), Triterpenes (Betulinic Acid, Olenolic Acid, uvole), etc. which contain polyphenol or carbonyl groups and polyhydroxy groups. The graphene (GO) oxide surface contains a variety of functional moieties, such as carboxylic, epoxy, and hydroxyl groups [119]. In Salvia, the carboxylic group undergoes condensation on reaction with reductive forms. Reduced graphene oxide formation showing ring opening due to further reduction. In the case of the hydroxyl derivative, the condensation to form the ring followed by the cleavage of the ring smooths, reducing the GO. The epoxy group causes the ring to open to a reaction in Salvia with the polyhydroxy groups then followed by cleavage and ring formation resulting in the GO reduction [120].

Figure 6.3 demonstrates the XRD spectra of premier graphite, GO, and Pd / rGO composite of various reducing agents. The formation of GO and rGO was confirmed by XRD data using different reducing agents. As revealed in Figure 6.3, the graphite powder at 26.2° represents a sharp central diffraction peak, with 0.33 nm d-spacing from the corresponding. By oxidizing graphite powder in an acidic medium, graphene oxide was synthesized, introducing hydroxyl, carboxyl, and epoxy groups onto graphene sheets [121]. The GO's XRD spectra exhibit a new peak at 11.7°, corresponding to C (002) with a 0.88 nm interlayer spacing because between the

graphite layers, there are intercalated species [122,123]. The graphene oxide's larger interlayer spacing comparison to graphite could be referred to as the insertion of the oxygen functional groups such as carbonyl, hydroxyl, and epoxy that formed over the process preparation [125].

Using the Scherrer equation, the layer numbers of graphene can be calculated, which is expressed by:

$$D = \frac{K\lambda}{\beta \cos\theta} \tag{6.1}$$

n (number of layers) = D/d spacing  (6.2)

When D represents crystal thickness (graphene thickness) or particle size, K represents the crystal-dependent constant shape (0.9), $\lambda$ represents the X-ray wavelength, $\beta$ represents FWHM (full width at half maximum) and $\theta$ represents the scattering angle.

The thickness of graphene layers reduced by hydrazine, $NaBH_4$, and plant extract was 15, 20, and 12 nm, showing the layer numbers 44, 60, and 33, respectively.

The XRD spectra shows a broad diffraction peak at 24°, 25.4°, 26° rGO by Hydrazine, $NaBH_4$, and by plant extract, respectively, and the diffraction peak at 11.7° indexed to GO was disappeared.

The shift and broadening of the rGO's characteristic XRD diffraction peak from 26° to 24° could be because of 2 factors: 1st, randomly ordered arrangement of rGO stacked sheets or a relatively short domain order in stacked and 2nd, the small size of sheets, each of these factors broadens the XRD peak [126].
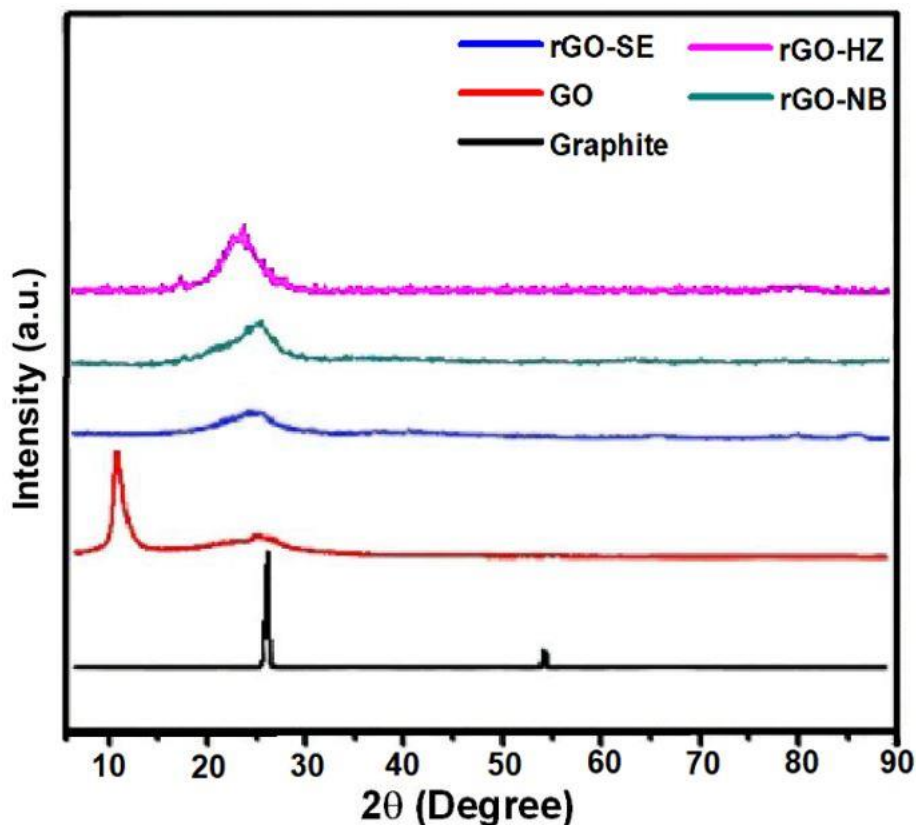
Figure 6.3. The XRD pattern of rGO with different reducing agents.

Raman spectroscopy shows information of graphene's quality and structure, including defect density, disorder, and defect structure [127,128]. Figure 6.4 Raman spectra comparison of rGO prepared using various reducing agents. The graphite powder shows the in-plane vibration of graphite lattice at 1579 cm$^{-1}$ (G-mode) and 1320 cm$^{-1}$ (D mode). The exfoliated GO appears in the spectrum of the G-band (1581 cm$^{-1}$) with another D-band at 1314 cm$^{-1}$. Usually, in GO the blue shift in the G band is indicated to the existence of isolated double bonds that resonate at a higher frequency than the G band of graphite [129]. The rGO spectrum synthesized by (NaBH$_4$) shows a red-shifted D band 1320.2 cm$^{-1}$ comparing to GO at 1314 cm$^{-1}$ showing the introduction of sample defect and disturbance of the sp$^2$ bands present in the plane [130]. For rGO by plant extract, there was high energy 2nd-order 2D mode, about 2606 cm$^{-1}$, and S3 mode at 2902 cm$^{-1}$, and this indicates better reduction [131]. The D-band to G-band intensity ratio is used to measure quality structures of graphite since the ratio for high-order graphite is about 0 [132]. The intensity ratio examination for the I$_D$ / I$_G$ domains may indicate the number of defects in the sample

that can be calculated by measuring the $I_D$ / $I_G$ density ratio. A higher $I_D$ / $I_G$ ratio means a higher disorder degree due to the removal of oxide groups from graphene oxide, indicating more defective GO. The $I_D$ / $I_G$ intensity ratio of the catalyst synthesized by the plant extract gives the lowest value of 0.62, which references that the number of defects is low while the $I_D$ / $I_G$ intensity ratio of the catalyst compounded by other reducing agents Hydrazine or NaBH4 is higher. This increase can be clarified in terms of perturbation input and $sp^2$ field defects [133]. The shape and position of the 2D peak depend on the number of graphene layers, so the 2D peak can be used to classify it into few layers, two layers and one layer. Furthermore, usually the 2D / G intensity ratio of single-, double-, triple and multi- (> 4) layer graphene is> 1.6, ~0.8, ~0.3, and ~0.07, respectively. Here also, all 2D / G ratio samples were found from the range of 0.45 to 0.7 (Table 6.1). This means that the sheets in the suspension mainly had double layers. Table 6.1 indicates the impact of reducing agents in reduction and properties of graphene as reported in literature.
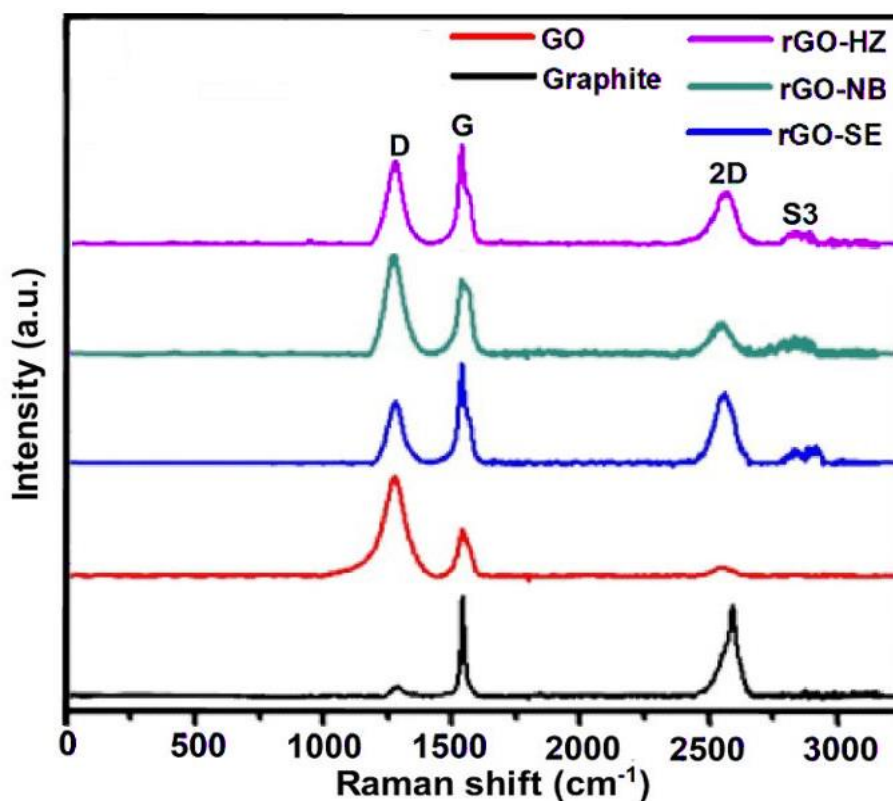


Figure 6.4. The Raman spectra of rGO with different reducing agents.

Table 6.1. A comparison reduction of GO with different reducing agents.

| Reducing agent | d-spacing | $I_D/I_G$ | $I_{2D}/I_G$ | Methode | Application | Ref |
|---|---|---|---|---|---|---|
| CRG/sulfur-containing compounds | 0.87 nm | 1.22 | - | low toxicity | - | [134] |
| RGO/ urea | 0.35 nm | - | - | green | supercapacitor | [135] |
| RGO/ aluminum powder | 0.375 nm | 1.81 | - | friendly | - | [136] |
| RG-Os/ HI–AcOH | 0.364 nm | 1.13 | 0.62 | toxic | flexible devices | [137] |
| CCG/NaBH$_4$ | 0.374 | 1.91 | 0.31 | toxic | various technological applications | [138] |
| Reduced GO/ Hydrazine hydrate | 0.34 nm | 1.1 | - | toxic | hydrogen | [139] |
| nHRGOs/ nascent hydrogen | | 1.88 | 0.6 | toxic | - | [140] |
| rGO-hydrazine | 0.34 | 1.32 | 0.45 | toxic | Li-O$_2$ | This Work |
| rGO-NaBH$_4$ | 0.33 | 0.83 | 0.50 | toxic | Li-O$_2$ | This work |
| rGO-plant extract | 0.36 | 0.62 | 0.70 | Green | Li-O$_2$ | This work |

FESEM is used to investigate the morphology of materials. The FESEM image of rGO (Figure 6.5a) exhibits a wrinkled structure of graphene nanosheets, while the cross-section view (Figure 6.5b) illustrates rGO 2D layers structure. The EDS spectra of rGO show that the sample is comprised entirely of C and O. Table 6.2 shows that the atomic fractions of C and O are 82.88 percent and 17.12 percent, respectively. Higher conductivity and improved electrochemical performance in batteries can be achieved by raising the carbon to oxygen ratio, demonstrating the efficacy of GO reduction in the sheets. Figure 6.5c depicts a one-dimensional nanowire with a tetragonal open end and length and width of about 1 μm and 10-50 nm , respectively, while Figure 6.5d represents the dispersion of α-MnO$_2$ nanowires over the surface of rGO sheets.
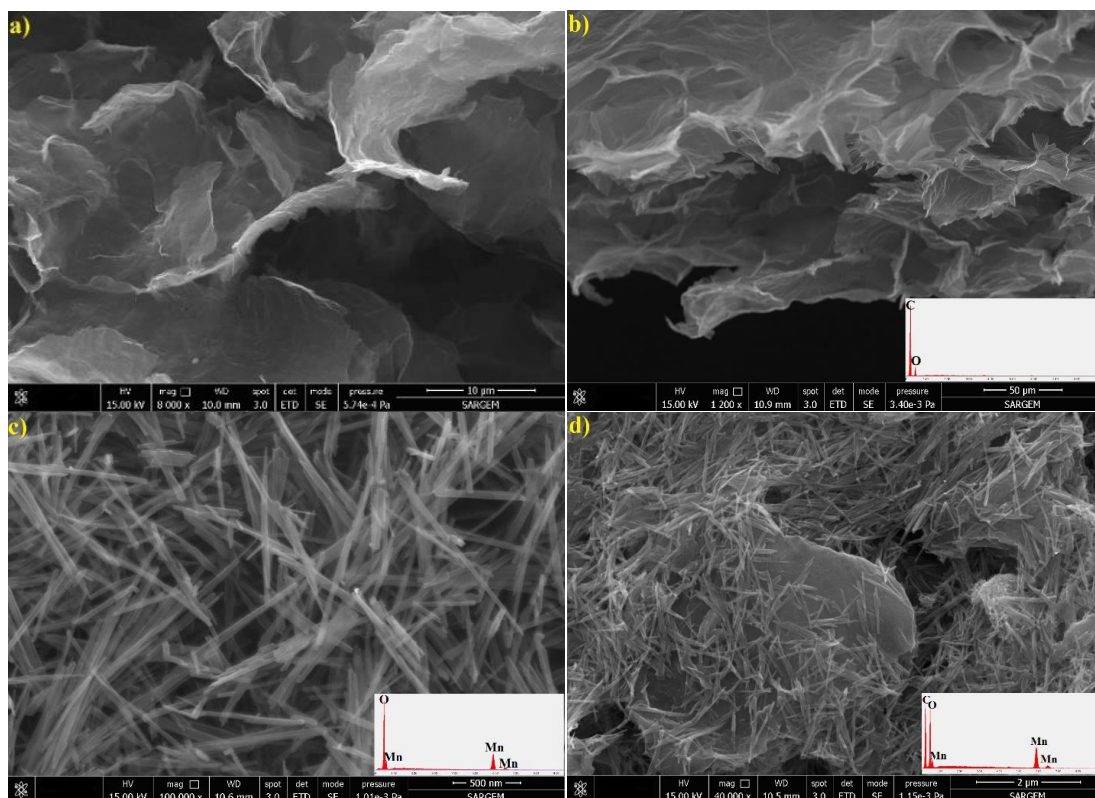
Figure 6.5. FESEM images of rGO surface (a) and cross section of rGO (b), $\alpha$-MnO$_2$ nanowires (c), and anchored $\alpha$-MnO$_2$ nanowires on the surface of rGO sheets (d).

rGO/Ru/$\alpha$-MnO$_2$ nanocomposites were synthesized by designing the Ru nanoparticles on PAA-wrapped $\alpha$-MnO$_2$ nanowires and dispersed on the surface of rGO sheets. To nucleate the Ru nanoparticle, polyacrylic acid (PAA) was coated around the MnO$_2$ nanowires. During the synthesis, the PAA-wrapped nanowires boosted the aqueous solubility of the nanowires, resulting in a more uniform solution of $\alpha$-MnO$_2$ nanowires (Figure 6.5b). The control experiment without PAA wrapping resulted in aggregated Ru nanoparticle formation on the surface of $\alpha$-MnO$_2$ nanowires, as shown in Figure 6.6a. To nucleate Ru nanoparticles on PAA-wrapped $\alpha$-MnO$_2$ nanowires, NaBH$_4$ was utilized as a reducing agent to interact with Ru raw material (RuCl$_3$). In order to improve the conductivity and surface area of the Ru/ $\alpha$-MnO$_2$ electrode, they were dispersed on the surface of rGO sheets. It is expected that the rGO channels provide a smooth pathway for Ru/$\alpha$-MnO$_2$ nanowires to interact rapidly with Li$^+$ and O$_2$ and generate Li$_2$O$_2$. It is noted that effective catalytic activity is expected to be associated with a high surface area of the active catalytic sites, as in fact provided here by the well-separated nanoparticles of Ru on $\alpha$-MnO$_2$ nanowires [141,142]. Furthermore, the presence of carbon, manganese, ruthenium, and oxygen

was verified by the energy-dispersive X-ray spectroscopy (EDX) images shown in the insets of Figures 6.6b and 6.6c. The homogeneous distribution of Ru nanoscale particles on the surface of $\alpha$-MnO$_2$ nanowires and rGO was observed by EDS elemental mapping in Figure 6.7 and approve the existence of Ru nanoparticles decorated on $\alpha$-MnO$_2$ nanowires.
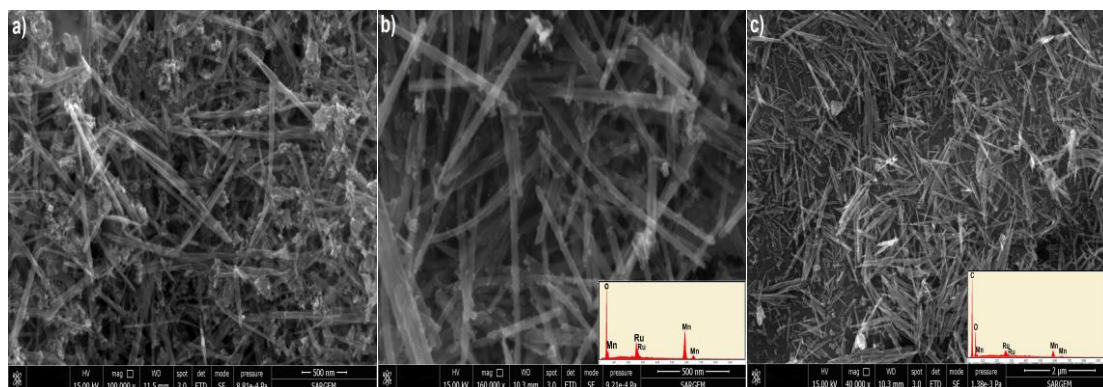


Figure 6.6. FESEM images of Ru/$\alpha$-MnO$_2$ a) and wrapped-PAA Ru/$\alpha$-MnO$_2$ nanowires b) and rGO/Ru/$\alpha$-MnO$_2$ nanocomposites c).
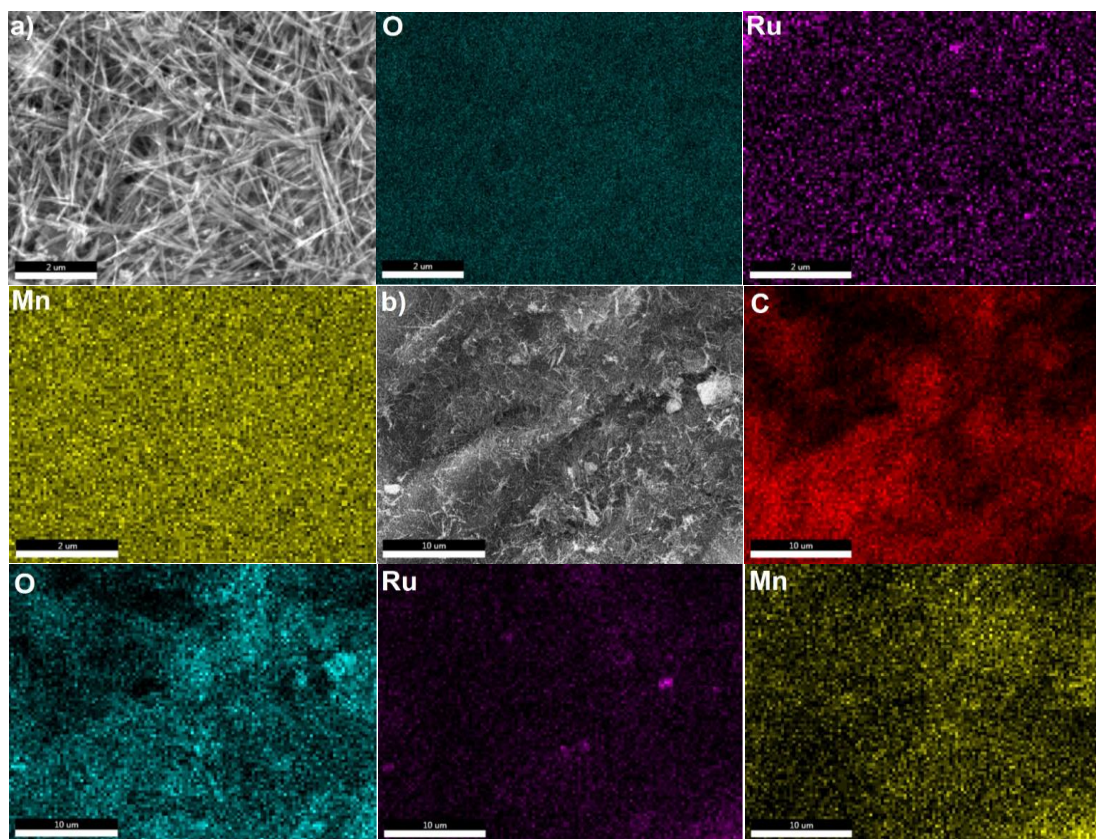


Figure 6.7. EDS mappings of a) wrapped-PAA Ru/$\alpha$-MnO$_2$ nanowires and b) and rGO/Ru/$\alpha$-MnO$_2$ nanocomposites.

The crystallographic structure of Ru/α-MnO$_2$ nanowires and rGO/Ru/α-MnO$_2$ were investigated with X-ray diffraction (XRD) (Figure 6.8). First, the XRD pattern of both samples showed peaks centred at 2θ of 12.6º, 18.0º, 28.8º, 36.7º, 38.7º, 41.7º, 49.7º, 56.3º, 60.4º, 65.5º, 69.6º and 72.9º matching to planes of α-MnO$_2$ (1 0 0), (0 0 2) and ( 1 0 2) (powder diffraction file number 44-0141). Three weak peaks were observed at 2θ of 38.3, 42.1, and 58º assigned to Ru (powder diffraction file number 06-0663), which confirmed the presence of metallic Ru along with α-MnO$_2$ in the Ru/α-MnO$_2$ and rGO/Ru/α-MnO$_2$ hybrids, respectively.

This work mainly emphasizes investigating the catalytic performance of the Ru/α-MnO$_2$ and rGO/Ru/α-MnO$_2$ materials to address the overpotential issues of the OER reaction in Li-O$_2$ cells. In this regard, the conductivity and well separated uniform distribution of the catalysts on the conducting support in our hybrid system are certainly essential properties.
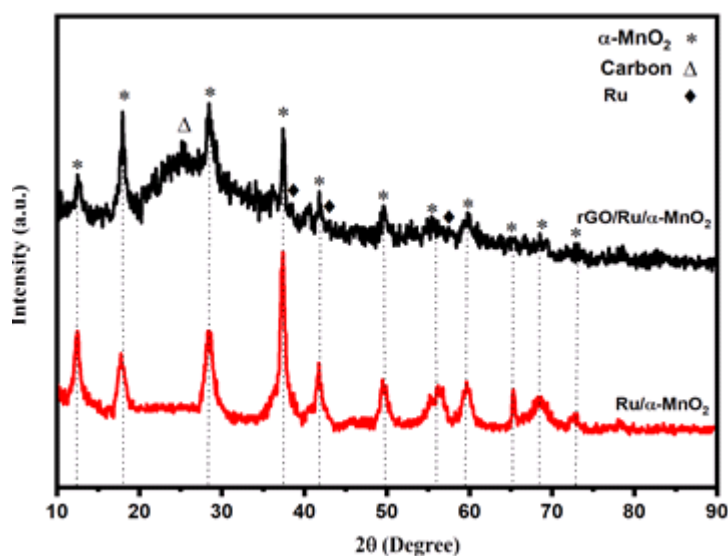


Figure 6.8. XRD spectra of Ru/α-MnO$_2$ and rGO/Ru/α-MnO$_2$.

The development system of the rGO@Pd@α-MnO$_2$ hybrid is shown in Figure 6.9. To begin, the modified Hummers process is used to prepare graphene oxide (GO). The oxidation of graphite flakes in an acidic dispersion results in the insertion of epoxy, hydroxyl, and carboxyl groups on graphene sheets, resulting in the formation of GO. These functional oxygen groups serve as excellent metal ion bonding anchor

sites. As a result, $Pd^{2+}$ may interact with functional groups and interact on the surface and edges of graphene oxide, resulting in higher palladium nanoparticle dispersion and reduced aggregation. Following that, $NaBH_4$ simultaneously reduces Pd nanoparticles and GO. In the last phase, $\alpha$-$MnO_2$ nanowires are combined with rGO@Pd and ball milled to strengthen the bonding between $\alpha$-$MnO_2$ and rGO@Pd and enhance the surface area of the rGO@Pd@$\alpha$-$MnO_2$ nanocomposite's electrochemical performance.
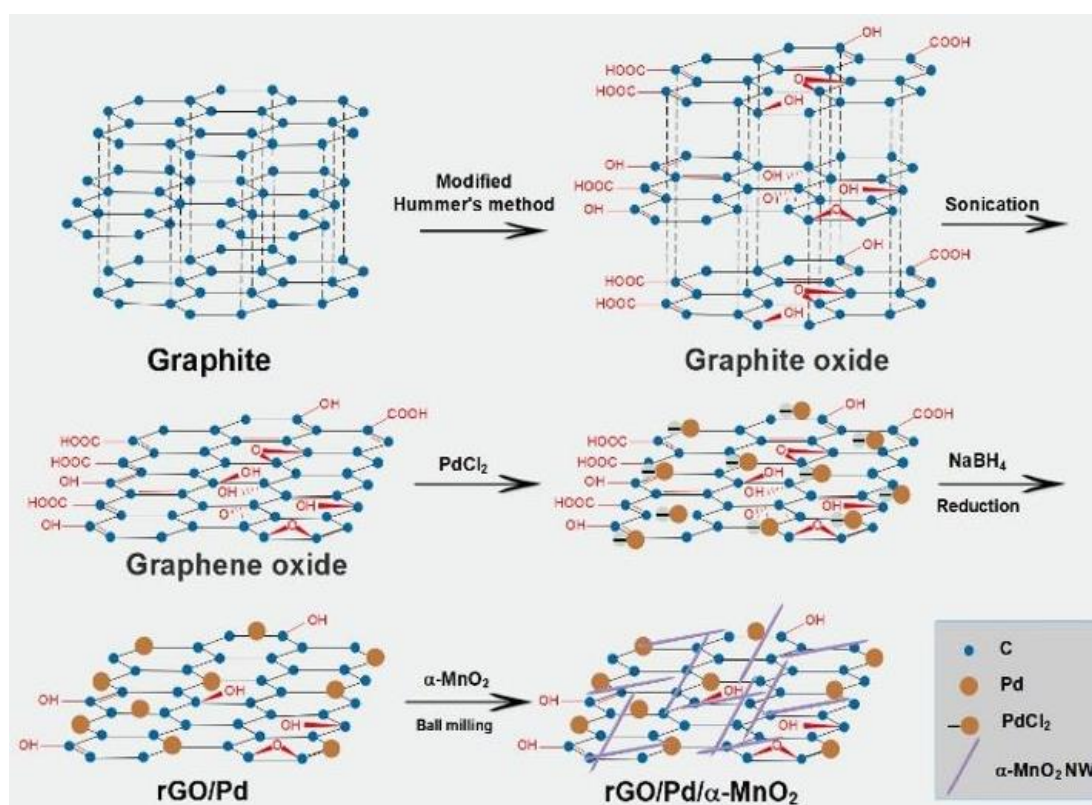


Figure 6.9. The preparation of rGO@Pd@$\alpha$-$MnO_2$ for an air cathode material is depicted schematically.

The $\alpha$-$MnO_2$ nanowires distribute on rGO sheets, and the produced rGO@Pd (Figure 6.10a and 6.10b) results in well-distributed Pd nanoscale particles with sizes ranging from 5 to 10 nm on the graphene sheets. The FESEM images of rGO@Pd@$\alpha$-$MnO_2$ (Figure 6.10c and 6.10d) show great interaction and high bonding of $\alpha$-$MnO_2$ NWs on the rGO surface because of the successful ball milling procedure.
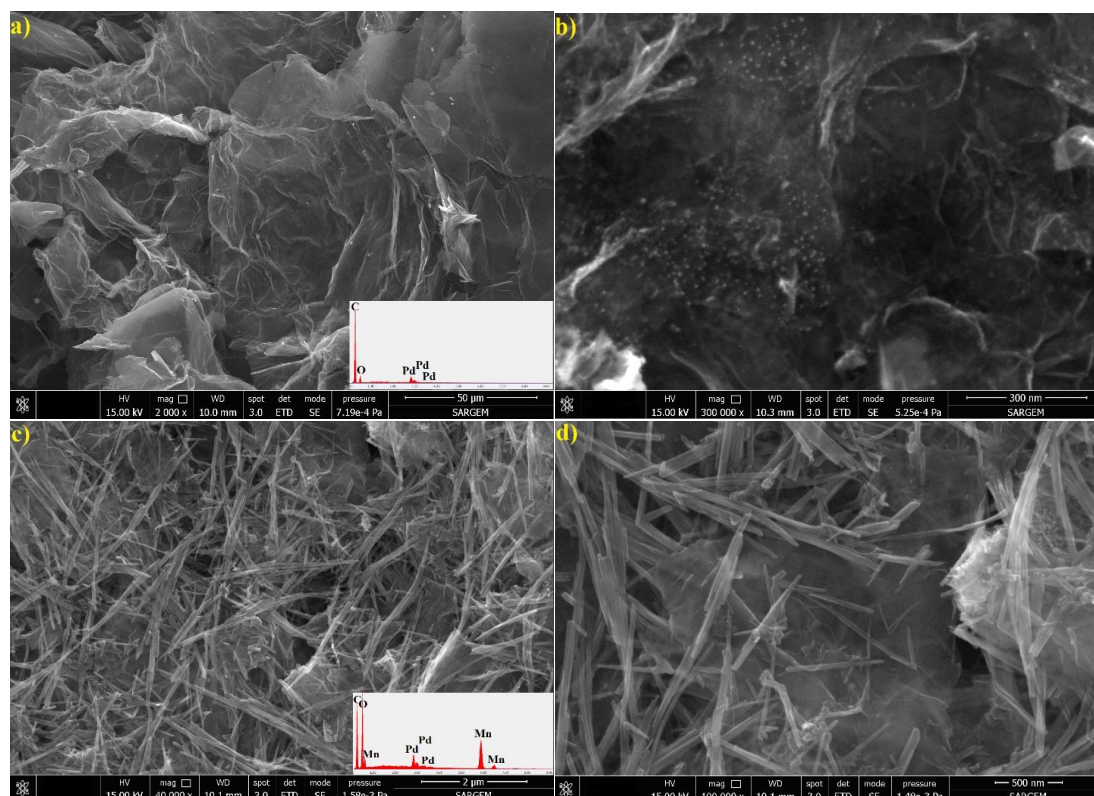
Figure 6.10. FESEM images of dispersed Pd nanoparticles on rGO sheet in low and high magnitude (a,b), and α-MnO$_2$ nanowires distributed and Pd nanoparticles incorporated graphene sheets (c,d).

Table 6.2. The weight % of elements in each sample according to EDS result.

| | Weight Percentage wt.% | | | |
| --- | --- | --- | --- | --- |
| | C | O | Mn | Pd |
| rGO | 78.42 | 21.58 | - | - |
| α-MnO$_2$ | - | 36.82 | 62.19 | - |
| rGO/Pd | 54.67 | 22.78 | - | 22.5 |
| rGO/α-MnO$_2$ | 47.69 | 31.14 | 21.18 | - |
| rGO/Pd/α-MnO$_2$ | 35.7 | 20.46 | 22.15 | 21.68 |

As shown in Figure 6.11a, EDS mapping was used to confirm the uniform distribution of Pd nanosize particles on rGO sheets. The mapping of rGO@Pd reveals three elements: carbon (C), oxygen (O), and palladium (Pd). This indicates that Pd nanoparticles are distributed uniformly over rGO sheets. Furthermore, even after α-MnO$_2$ dispersion in the nanocomposite structure, EDS mapping of rGO/Pd/α-MnO$_2$ reveals the homogenous distribution of Pd nanoparticles (Figure 6.11b).

The structure and dispersion of Pd nanosized particles and α-MnO$_2$ NWs on the rGO sheets surface are further verified using TEM characterization, as illustrated in Figure 6.12. Due to the presence of active sites (defects), which facilitate in the homogenous incorporation of Pd nanoscale particles on GO surface upon the co-reduction process, TEM images of rGO@Pd demonstrate an excellent dispersion of Pd nanoparticles on rGO product with no distinctive aggregation on the rGO surface (Figure 6.12a and 6.12b). Following α-MnO$_2$ dispersion, α-MnO$_2$ NWs are found decorated on the rGO@Pd surface, forming a good channel and interaction with catalysts (Figure 6.12c and 6.12d).
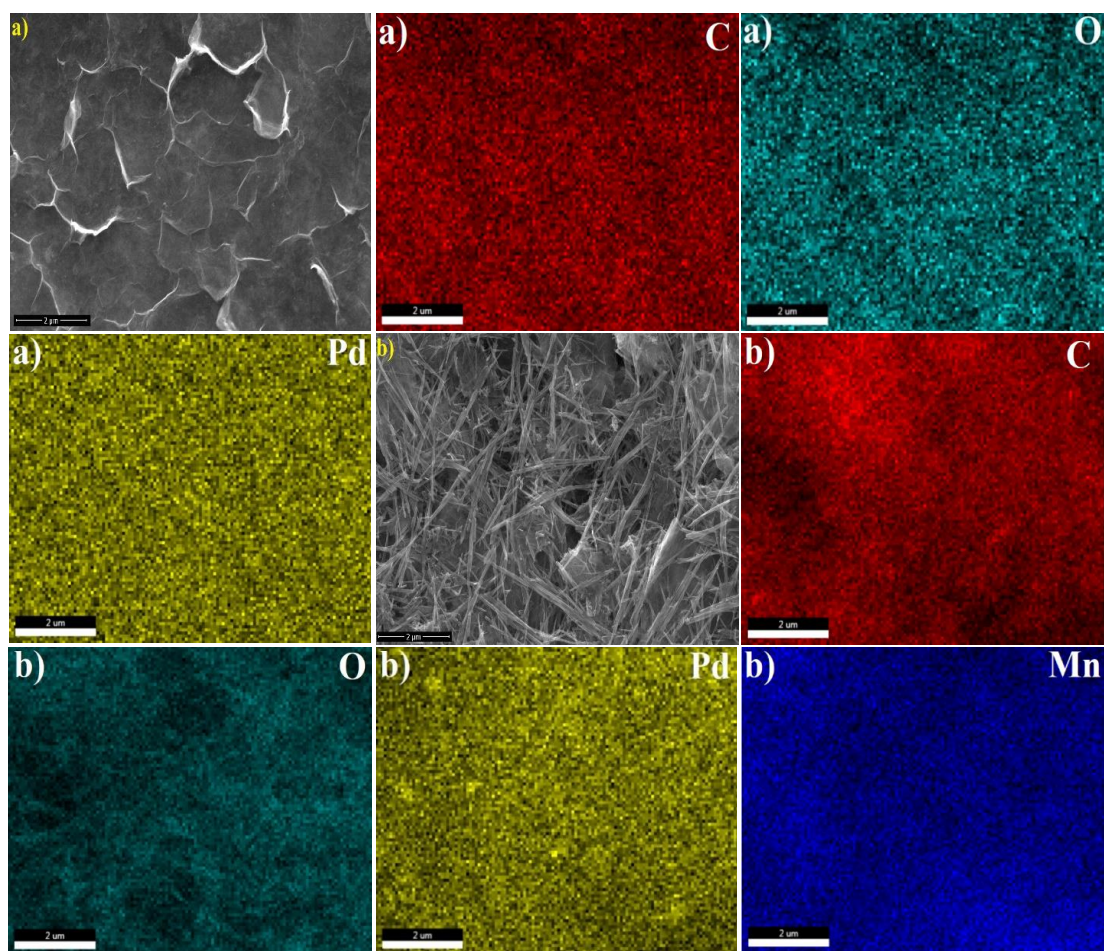


Figure 6.11. EDS mapping confirmed the well dispersion of Pd nanoparticles on rGO (a) and the presence of Mn on rGO/Pd nanocomposites (b).
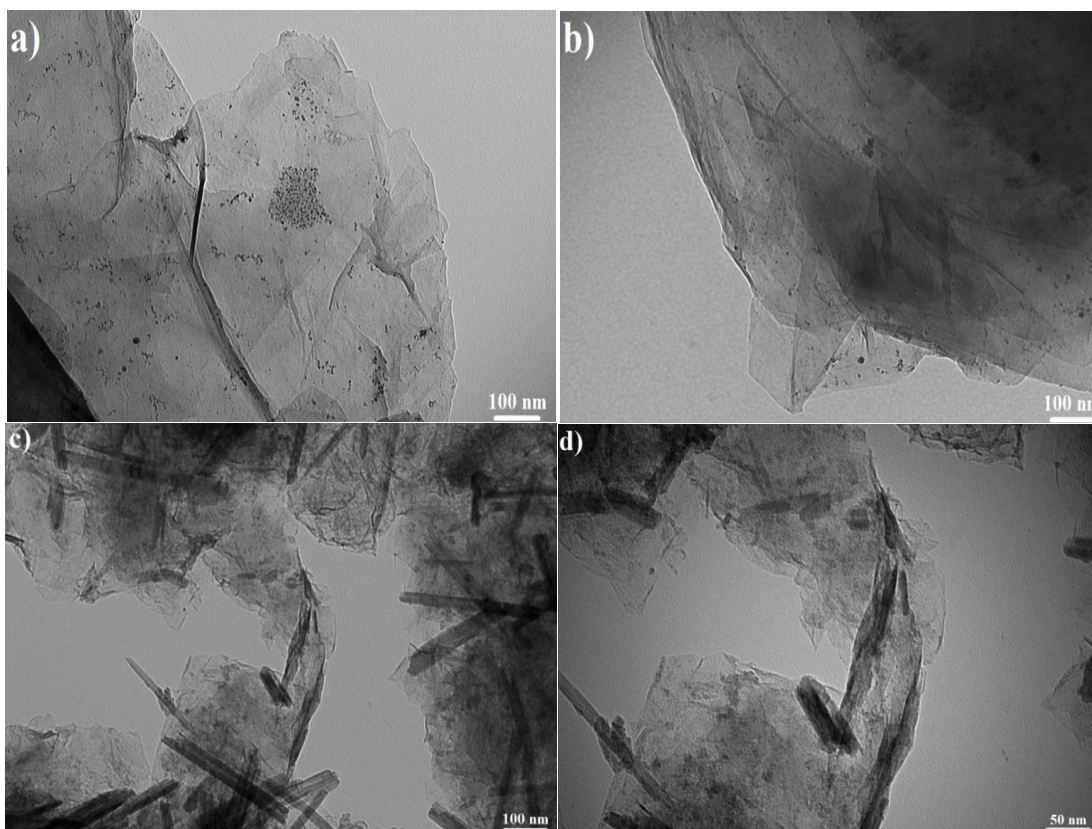
Figure 6.12. TEM images reveal the dispersion of Pd on rGO surface (a,b) and $\alpha$-MnO$_2$ nanowires anchored on rGO@Pd (c,d).

The crystallinity and phase purity of rGO, rGO@$\alpha$-MnO$_2$, rGO@Pd, and rGO@Pd@$\alpha$-MnO$_2$ are were investigated by XRD diffraction, as shown in Figure 6.13a. The distinctive diffraction peak of rGO can be seen at $2\theta=24°$, which corresponds to the (0 0 2) plane of rGO, indicating that graphene was successfully reduced in all samples. The strong peaks at $2\theta= 40°, 46.6°, 68.1°, 82.2°$, and $86°$ in rGO/Pd XRD spectra are assigned to crystalline planes of center faced cubic structures of Pd (1 1 1), (2 0 0), (2 2 0), (3 1 1), and (2 2 2) (JCPDS, Card No. 46-1043), respectively. The Pd reflection peaks can still be seen in the rGO@Pd@$\alpha$-MnO$_2$ XRD pattern. That suggests that the structure of Pd in both rGO@Pd and rGO@Pd@$\alpha$-MnO$_2$ is the same. The diffraction peaks of MnO$_2$ at $2\theta= 12.6°, 18.0°, 28.8°, 36.7°, 38.7°, 41.7°, 49.7°, 56.3°, 60.4°, 65.5°, 69.6°$ and $72.9°$ assigning to (1 1 0), (2 0 0), (3 1 0), (4 0 0), (2 1 1), (4 2 0), (3 0 1), (6 0 0), (5 2 1), (0 0 2), (5 4 1), and (3 1 2) planes which are in good agreement with $\alpha$-MnO$_2$ phase (JCPDS, Card No. 44-0141). Pd and $\alpha$-MnO$_2$ diffraction peaks can be observed in rGO@Pd@$\alpha$-

MnO$_2$, showing that Pd and α-MnO$_2$ nanowires are well assembled on rGO sheets [143].
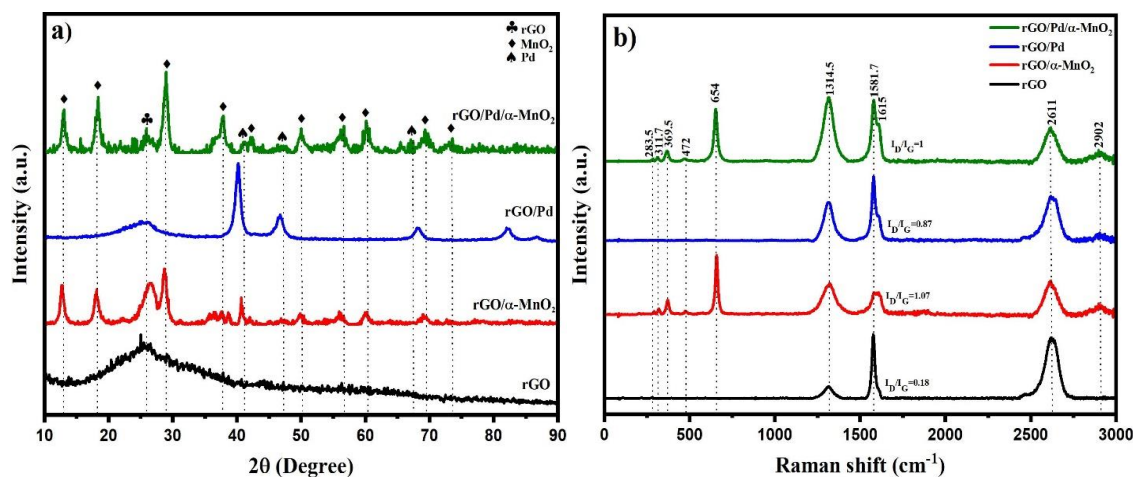


Figure 6.13. The XRD (a) and Raman spectra (b) for reduced graphene oxide, rGO@α-MnO$_2$, rGO@Pd, and rGO@Pd@α-MnO$_2$ samples.

Raman spectroscopy is used to determine the structure and quality of graphene, as well as the structure of disorder and defects, as presented in Figure 6.13b. The in-plane vibration of graphite lattice is indicated by the Raman spectra of rGO at 1582.3 cm$^{-1}$ (G-band) and 1324.3 cm$^{-1}$ (D-band), indicating the insertion of the defect in the sample. The high energy second order 2D mode is also seen for rGO about 2631 cm$^{-1}$ and S3 mode around 2910 cm$^{-1}$, indicating that graphitization is improving. The level of D mode increases in contrast to rGO due to the deposition of Pd on the surface of rGO, according to the Raman spectra of rGO@Pd. Due to the deposition of metal nanoparticles, which generate a chemical bond contact with defects in graphene sheets during the reduction process GO, the intensity of the D band is considerably increased compared to the G band, as previously reported [144]. The intensity ratio of D and G bands for rGO is 0.18, while this ratio for rGO@Pd, rGO@Pd@α-MnO$_2$, and rGO@α-MnO$_2$ are 0.87, 1.00, and 1.07, respectively. A higher intensity of D to G ratio in rGO@Pd@α-MnO$_2$ and rGO@α-MnO$_2$ can also be attributed to strong MnO$_2$ and rGO incorporation. Furthermore, an electrical interaction between Pd and rGO causes a shoulder in the G band at 1611 cm$^{-1}$ in both rGO@Pd and rGO@Pd@α-MnO$_2$ nanocomposites, which disappears in rGO and rGO@α-MnO$_2$ structures. Furthermore, the peak centered at 651 cm$^{-1}$ was linked to MnO$_6$ stretching

mode. The weaker peaks at 312.3 and 368.4 $cm^{-1}$ belonged to the bending mode of O-Mn-O and were formed by the production of $Mn_2O_3$ or $Mn_3O_4$. As a result, Raman peaks at 313.6 $cm^{-1}$, 361 $cm^{-1}$, and 653 $cm^{-1}$ in rGO@Pd@α-$MnO_2$ and rGO@α-$MnO_2$ nanocomposites reveal the α-$MnO_2$ nanostructures.

## 6.2. Electrochemical Performance Of Graphene And Graphene-Based Nanocomposites

The electrodes capacity performance was investigated using galvanostatic full charge-discharge experiments. The electrodes were fully charged and discharged at a current density of 100 mA $g^{-1}$ in the range of 2-4.2 V. Figure 6.14a shows that the rGO/Ru/α-$MnO_2$ air electrode has a specific capacity of 7800 mAh $g^{-1}$, a round-trip efficiency of 73.6 percent (the ratio of the discharge voltage of 2.8 V to the charge voltage of 3.8 V), and a nearly 100 percent coulombic efficiency, implying good charging efficiency. The Ru/α-$MnO_2$ electrode, in contrast, has a discharge capacity of 2400 mAh $g^{-1}$, a round-trip efficiency of 61.9 percent (2.6 V-4.2 V), and a coulombic efficiency of 71.4 percent, indicating poor $Li_2O_2$ dissolution. The findings suggested that graphene-supported Ru/α-$MnO_2$ contributes significantly to catalytic capacity [145]. Graphene's high surface area and porosity improved electron transport to the active sites of Ru/α-$MnO_2$ and allowed for a rapid interaction with $O_2^-$ and $Li^+$ ions to form $Li_2O_2$. During charging, the rGO/Ru/α-$MnO_2$ electrode revealed two charge voltages, indicating that $Li_2O_2$ was being decomposed in two stages. As a result, it is clear that rGO/Ru/α-$MnO_2$ hybrids contributed as an active catalyst in lowering the overpotential and increasing capacity. Furthermore, Table 6.3 mentions various carbon-based electrodes, suggesting that the rGO/Ru/α-$MnO_2$ electrode has the maximum capacity. This could be due to the high surface area and electronic conductivity that Ru and graphene have provided and enhanced oxygen absorption [146].

The cyclability of supported rGO/Ru/α-$MnO_2$ hybrids was explored in Li−air cells at capacity-limited conditions of 800 mAh $g^{-1}$ and compared with that of Ru/α-$MnO_2$ electrode. Figure 6.14b shows that the Ru/α-$MnO_2$ electrode was stable for 30 cycles

and had a comparatively high energy efficiency of 47 percent. After 40 cycles, the full discharge/charge potential plateaus of rGO/Ru/$\alpha$-MnO$_2$ were 2.8 V and 3.9 V, respectively. The charge potential was under 4.1 V (Figure 6.13c), indicating that rGO/Ru/$\alpha$-MnO$_2$ had good oxygen evolution reaction catalytic performance. After 40 cycles, the discharge/charge voltages for rGO/Ru/$\alpha$-MnO$_2$ were 2.25 V and 4.1 V, respectively, and the energy efficiency was 54.8 percent. The use of rGO/Ru/$\alpha$-MnO$_2$ resulted in a longer battery life cycle, which is assigned to the large surface areas and inherent porous structures of graphene, which provided good ORR and OER [147].

The catalytic activity was also evaluated by cyclic voltammetry (CV). CV curves of Ru/$\alpha$-MnO$_2$ and rGO/Ru/$\alpha$-MnO$_2$ hybrid are recorded in the potential range of 2−4.5 V and are given in Figures 6.14d and 6.14e. rGO/Ru/$\alpha$-MnO$_2$ shows a higher current density in comparison with Ru/$\alpha$-MnO$_2$ indicating improved electrochemical reactions during cycling. However, the current level of Ru/$\alpha$-MnO$_2$ was lower than that of the rGO/Ru/$\alpha$-MnO$_2$ electrodes, displaying a lower catalytic activity of free graphene. rGO/Ru/$\alpha$-MnO$_2$ CV curve indicated increased voltammograms, both anodic and cathodic scans, with a larger current density of the reduction and oxidation peaks. Because of the reversibility of Li$_2$O$_2$ formation/decomposition processes, the ORR and OER catalysis of rGO/Ru/$\alpha$-MnO$_2$ were enhanced, resulting in increased specific capacity, high cyclability, and low polarization. Furthermore, two peaks were observed during OER for rGO/Ru/$\alpha$-MnO$_2$, indicating the decomposition of discharge products in two steps. The onset ORR was detected at 2.7 V, which is higher than ORR potential of Ru/$\alpha$-MnO$_2$.

Figures 6.15a and 6.15b represent the electrochemical impedance spectra (EIS) of Ru/$\alpha$-MnO$_2$ and rGO/Ru/$\alpha$-MnO$_2$ before and after the first discharge and charge test. The EIS plot comprises three frequency regions; the high-frequency region relevant to the ohmic resistance (R$_s$) that links the electrolyte, separator, and current collector in the cell. The middle frequency resistance (R$_{int}$) ascribes to the charge-transfer between the interface of electrolyte and an air cathode. The low-frequency region represents the diffusion process that generates a Warburg tail. After discharge, the R$_{int}$ value of the rGO/Ru/$\alpha$-MnO$_2$ electrode increases from 215 $\Omega$ to 984 $\Omega$ due to the

formation of discharge products ($Li_2O_2$) on the cathode surface. After charge, $R_{int}$ reduces to 265 $\Omega$, which closes to the resistance of a fresh electrode that explains the good reversibility. Whereas, after first discharge, the diameter of $R_{ct}$ increased from 403 $\Omega$ to 640 $\Omega$ for Ru/$\alpha$-MnO$_2$ and after charge reduced to 528 $\Omega$. The EIS plot of Ru/$\alpha$-MnO$_2$ reveals poor reversibility, and the $R_{ct}$ after discharge is lower than the $R_{int}$ in Ru/$\alpha$-MnO$_2$, which also proves the high discharge product deposition results in higher capacity. The obtained results can explain that the higher surface area of rGO/Ru/$\alpha$-MnO$_2$ provides a higher space to deposit the discharge product.

Table 6.3. The carbon-based electrodes were reported in previous works.

| Material | Electrolyte | Current density | Capacity | Ref. |
|---|---|---|---|---|
| $\alpha$-MnO$_2$/carbon | 1M LiPF$_6$- PC | 70 mA g$^{-1}$ | 3000 mAh g$^{-1}$ | [148] |
| Mo$_2$C-WC | 1M LiTFSI-TEGDME | 0.1 mA cm$^{-2}$ | 5006 mAh g$^{-1}$ | [149] |
| GO\ activated carbon | 1M LiCF$_3$SO$_3$-TEGDME | 50 $\mu$A cm$^{-2}$ | 3200 $\mu$Ah cm$^{-2}$ | [150] |
| $\alpha$-MnO$_2$/N-GNF | 1M LiTFSI-DMSO | 0.1 mA cm$^{-2}$ | 5000 mAh g$^{-1}$ | [151] |
| Ru- rGO | 1:4M LiCF$_3$SO$_3$-TEGDME | 500 mA g$^{-1}$ | 5000 mAh g$^{-1}$ | [152] |
| Ru@MPG | 0.5M LiClO$_4$-DMSO | 200 mA g$^{-1}$ | 6433 mAh g$^{-1}$ | [153] |
| RuO$_2$-B-HRG | 1M LiTFSI-TEGDME | 0.1 mA cm$^{-2}$ | 4300 mA h g$^{-1}$ | [154] |
| Co–Ru@C | 1M LiTFSI-TEGDME | 0.1 mA cm$^{-2}$ | 2092 mA h g$^{-1}$ | [155] |
| rGO/Ru/$\alpha$-MnO$_2$ | 1M LiClO$_4$-TEGDME | 100 mA g$^{-1}$ | 7800 mAh g$^{-1}$ | This work |
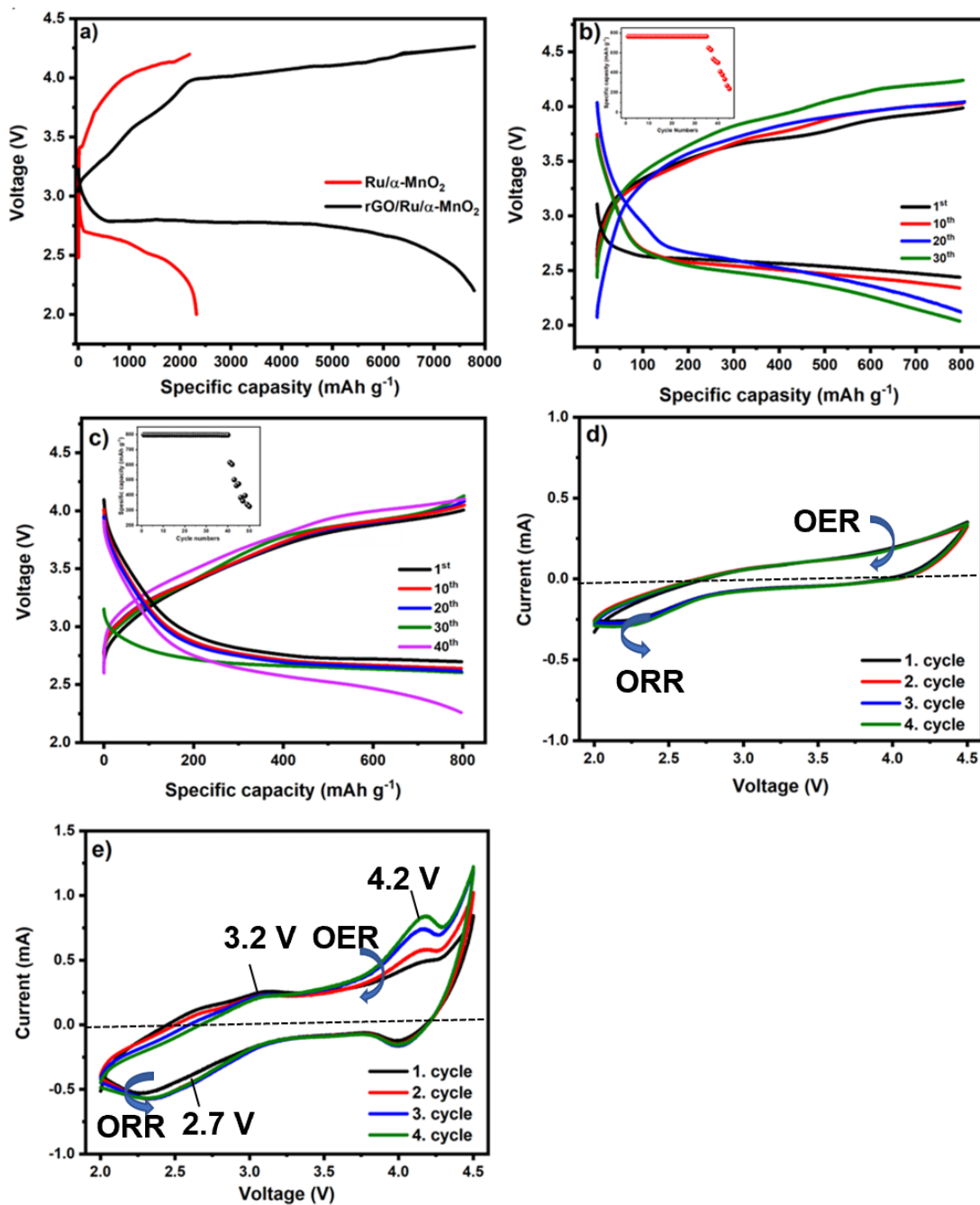
Figure 6.14. a) The initial full discharge/charge curves of Ru/α-MnO₂ and rGO/Ru/α-MnO₂ cathodes with a current density of 100 mA g⁻¹. Discharge/charge curves of the Ru/α-MnO₂ (b) and rGO/Ru/α-MnO₂ (c) cathodes at a fixed capacity of 800 mAh g⁻¹. Cyclic voltammetry scans of d) Ru/α-MnO₂, e) rGO/Ru/α-MnO₂ cathodes between 2.0 and 4.5 V with 0.3 mV s⁻¹.
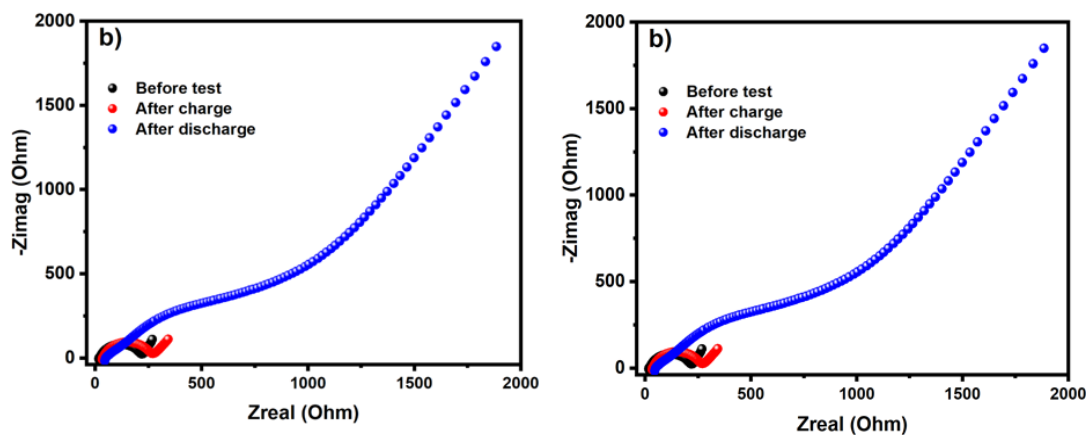
Figure 6.15. Nyquist plots of Li-O₂ cells with Ru/α-MnO₂ (e) and rGO/Ru/α-MnO₂ cathodes (f) before and after initial discharge-charge.

To understand the effect of graphene supported Ru/α-MnO₂ catalyst, the structures of cathodes were examined by FESEM after a full discharge. As shown in Figure 6.16a, MnO₂ nanowires are decomposed and covered by discharge products. In contrast, granular products are accommodated on the surface of rGO/Ru/α-MnO₂ electrode, and the structure of MnO₂ nanowires is sustained covered with discharge products (Figure 6.16b). These small particles cause easier decomposition and a high specific capacity. This shape can be due to the high surface area of graphene, which provided the smooth O₂ transport during the discharge state, and deposited Li₂O₂ would form particle on rGO/Ru/α-MnO₂. Therefore, the disintegration of the Ru/α-MnO₂ electrode resulted in insufficient Li₂O₂ decomposition, which could block pores and produce passivation of the electrode, resulting in irreversibility of Li-O₂ cell.

The XRD was carried out to air electrodes after first discharge to identify discharge products of electrodes. The corresponding XRD spectrum of rGO/Ru/α-MnO₂ (Figure 6.16c) showed peaks at 32.6º, and 40.6º were ascribed to the generation of Li₂O₂ and indexed well the reference XRD pattern of Li₂O₂ (JCPDS no. 09-0355). Also, a peak identified at 33.6º allocated to LiO₂ (JCPDS no. 77-2144) and two weak peaks at 21.2º and 31.3º were assigned to Li₂CO₃ (JCPDS no. 22-1141) due to reaction between graphene and Li₂O₂. Although, the XRD spectra of Ru/α-MnO₂ electrode indicated a weak peak at 32.2º indexed to Li₂O₂, and the peaks

corresponding to α-MnO$_2$ and Ru are not detected due to the decomposition of cathode materials, which is consistent with FESEM result.
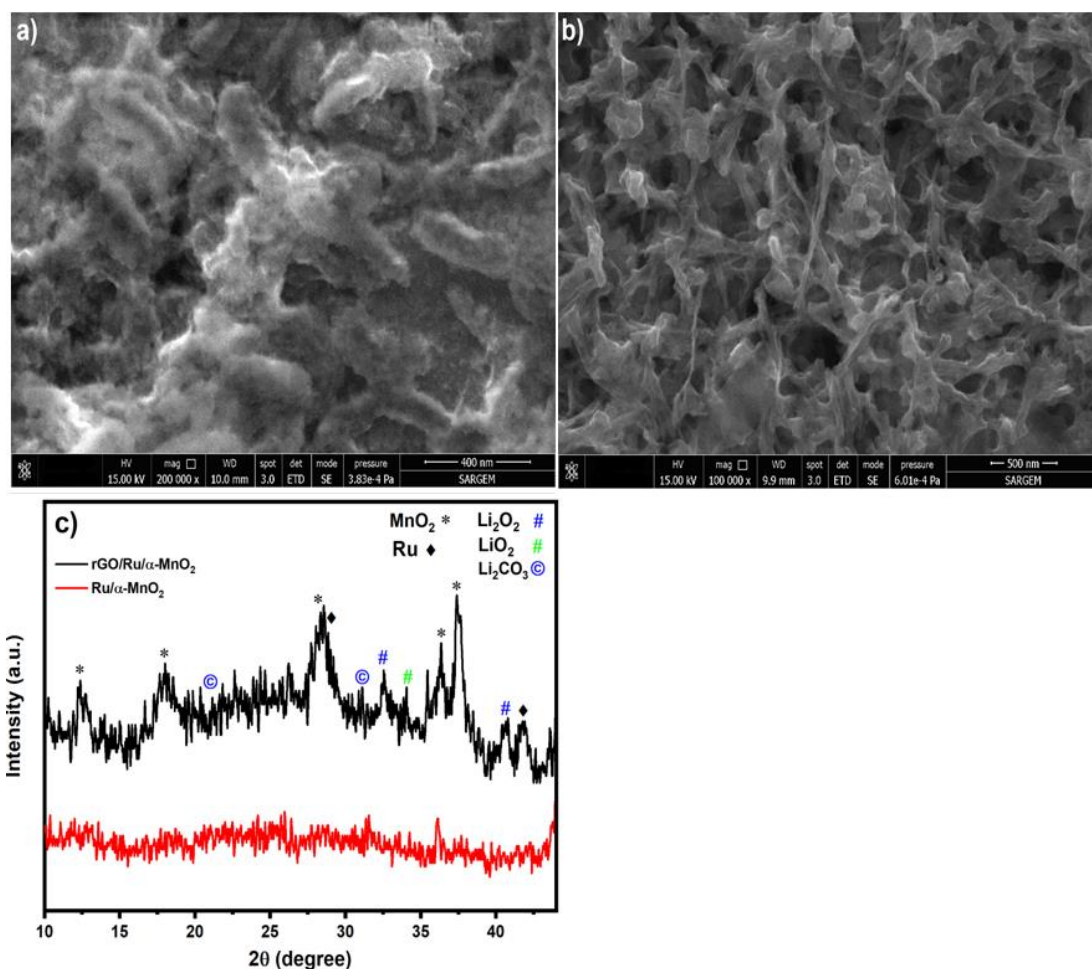


Figure 6.16. FESEM images of Ru/α-MnO$_2$ (a) and rGO/Ru/α-MnO$_2$ electrodes after a full discharge. The XRD pattern of cathodes after full discharge (c).

Thermogravimetric analysis (TGA) was performed for examining the thermal properties and constitution of graphene and catalysts in rGO, rGO@α-MnO$_2$, rGO@Pd, and rGO@Pd@α-MnO$_2$ samples. TGA curves of products exhibit the three parts of the decomposition in the existence of oxygen (Figure 6.17a). The TG curve of rGO@Pd@α-MnO$_2$ (green) indicates a 10% weight loss at temperatures below 110 °C, which is linked to the elimination of humidity and H$_2$O. The subsequent weight loss (10 percent) is caused by the elimination of oxygen-functional groups, and the final stage decomposition more than 200 °C is caused by the disintegration of the carbon structure, which results in steady weight loss up to

800 °C. At temperatures above 800 °C, the rGO@Pd@α-MnO₂ is relatively durable, representing about 50% of the mass of nanoparticles. The TG curves of rGO@Pd and rGO@α-MnO₂ show carbon skeleton elimination at temperatures of 400-850 °C and 410-550 °C, respectively. The attached Pd improves the thermal resistance of the rGO, resulting in a greater carbon degradation temperature in rGO@Pd. Last, the catalyst loading constituents in rGO@Pd, rGO@α-MnO₂, and rGO@Pd@α-MnO₂ samples are 25%, 25%, and 50%, respectively. Furthermore, carbon breakdown in the rGO@Pd@α-MnO₂ nanocomposite product is limited to lower temperatures than rGO@Pd and rGO@α-MnO₂ of a further increase in catalyst loading. The degradation of the carbon network causes a large weight loss for rGO nanosheets in the temperature of 310 to 510 °C, which is consistent with previous research [156,157].
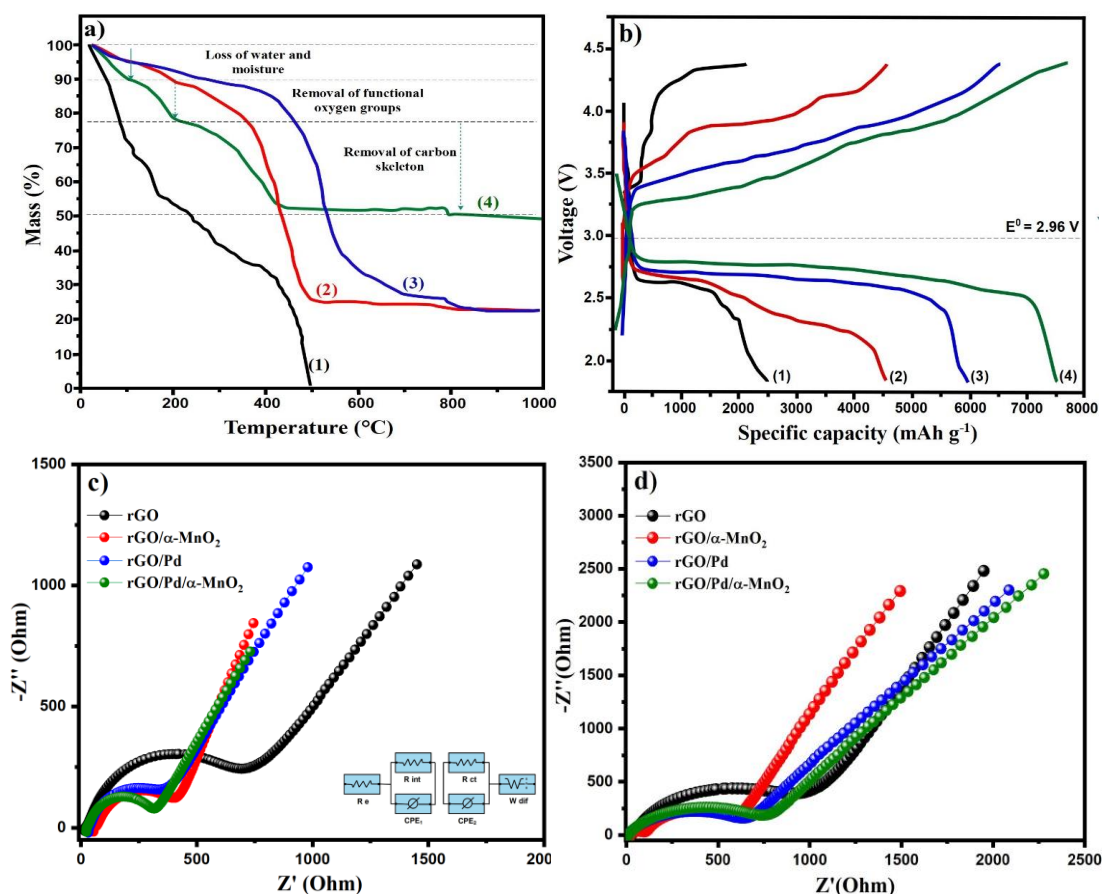


Figure 6.17. a) Thermal properties of rGO, rGO@α-MnO₂, rGO@Pd, and rGO@Pd@α-MnO₂ hybrids (4). b) At a current density of 100 mA g⁻¹, discharge/charge curves of rGO (1), rGO@Pd (2), rGO@α-MnO₂ (3), and rGO@Pd@α-MnO₂ (4) cathodes. The electrodes' electrochemical impedance data before (c) and after (d) first discharge (d).

In Li-air cells, the galvanostatic complete charge/discharge curves of rGO@Pd, rGO@Pd@$\alpha$-MnO$_2$, rGO@$\alpha$-MnO$_2$, and rGO are examined in the voltage window of 1.8-4.3 V (against Li/Li$^+$) with a current density of 100 mA g$^{-1}$ under an flowing oxygen. The initial discharge/charge curves of the cathodes in the lithium-air cell are compared in Figure 6.17b. The discharged rGO@Pd@$\alpha$-MnO$_2$ electrode has the maximum discharge capacity of 7500 mAh g$^{-1}$, while the discharge capacities of rGO@Pd, rGO@$\alpha$-MnO$_2$, and rGO are 6000, 4500, and 2500 mAh g$^{-1}$, respectively. For rGO, rGO@$\alpha$-MnO$_2$, rGO@Pd, and rGO@Pd@$\alpha$-MnO$_2$, the discharge plateau is 2.6 V, 2.7 V, 2.75 V, and 2.8 V, respectively. The charge potential drops in this order: rGO (4.3 V) > rGO/$\alpha$-MnO$_2$ (3.75 V) > rGO/Pd (3.4 V) > rGO/Pd/$\alpha$-MnO$_2$ (3.25 V). In addition, integrating nanosized Pd particles and MnO$_2$ enhances the capacity and oxygen reduction voltage of the cathodes from 2.6 V to 2.8 V, which is advantageous in reducing the cathodes' overpotential, as stated by Jung team [152]. According to Thapa group, both Pd and MnO$_2$ could inhibit charging voltage to 3.6 V and had a good capacity [157]. It is proposed that high the concentration of catalyst (50% wt) incorporated with rGO sheets improves graphene's catalytic performance, resulting in increased Li-ions transport and improved Li-O$_2$ cell electrochemical performance.

EIS measurements of rGO, rGO@Pd, rGO@$\alpha$-MnO$_2$, and rGO@Pd@$\alpha$-MnO$_2$ before and after discharge are shown in Figures 6.15c and 6.16d, respectively, using the Nyquist plot. On the equivalent circuit, all Nyquist results illustrate well-fitted curves (inset Figure of 6.17c). The circuit model consists of the electrolyte's ohmic resistance (R$_e$) and the separator's ionic resistance. R$_{int}$ refers to the electronic contact resistance at the interface of the current collector and the electrode, as well as capacitance (CPE$_1$). The transfer charge (R$_{int}$) and the constant phase element (CPE$_2$) attributed to the double-layer capacitance at the electrode surface correlate to the charge transfer (middle frequency semicircle). The Li$^+$ diffusion line could be defined in the low-frequency region [158]. The rGO/Pd/$\alpha$-MnO$_2$ cathode has a smaller R$_{int}$ diameter before discharge than the other cathodes, indicating good connectivity of component in the electrode and with the current collector. The diameter of the R$_{int}$ rises substantially after discharge because of the production of an

insulator discharge product. As a result, the diameter of the $R_{int}$ is altered from 750 to 900 Ω for rGO, from 450 to 603 Ω for rGO@α-MnO$_2$, from 325 to 700 Ω for rGO@Pd and from 305 to 760 Ω for rGO@Pd@α-MnO$_2$ after full discharge of the cells. The resistance difference before and after discharge was measured at 150, 153, 375, and 455 ohms, respectively. The high catalytic effect of α-MnO$_2$ and Pd results in a large amount of accomodated discharge residue, which results in a large resistance increased in the rGO@Pd@α-MnO$_2$ electrode after discharge.

The structure of electrodes following discharge is depicted in FESEM characterization, as seen in Figure 6.18. The structure of the discharge products was found to be a function of the catalyst on rGO sheets. FESEM images of after complete discharge, for the rGO and rGO@α-MnO$_2$ cathodes reveal the generation of a thin film-like coat (Figure 6.18a and 6.18b), whereas rGO@Pd shows the formation of toroid-like Li$_2$O$_2$ particles onto the rGO surface (Figure 6.18c). The morphology of Li$_2$O$_2$ formed in the rGO@Pd@α-MnO$_2$ system, on the other hand, is tiny particles (Figure 6.18d). Reduced carbon content and bifunctional catalysts play a key role in down sizing discharge particle size and inducing the oxygen reduction process [159]. As a result, the different shape of Li$_2$O$_2$ increases capacity while lowering charge potential. The presence of catalysts has been shown to affect the structure modes of Li$_2$O$_2$ from toroids to films or nansized particles [160,161].
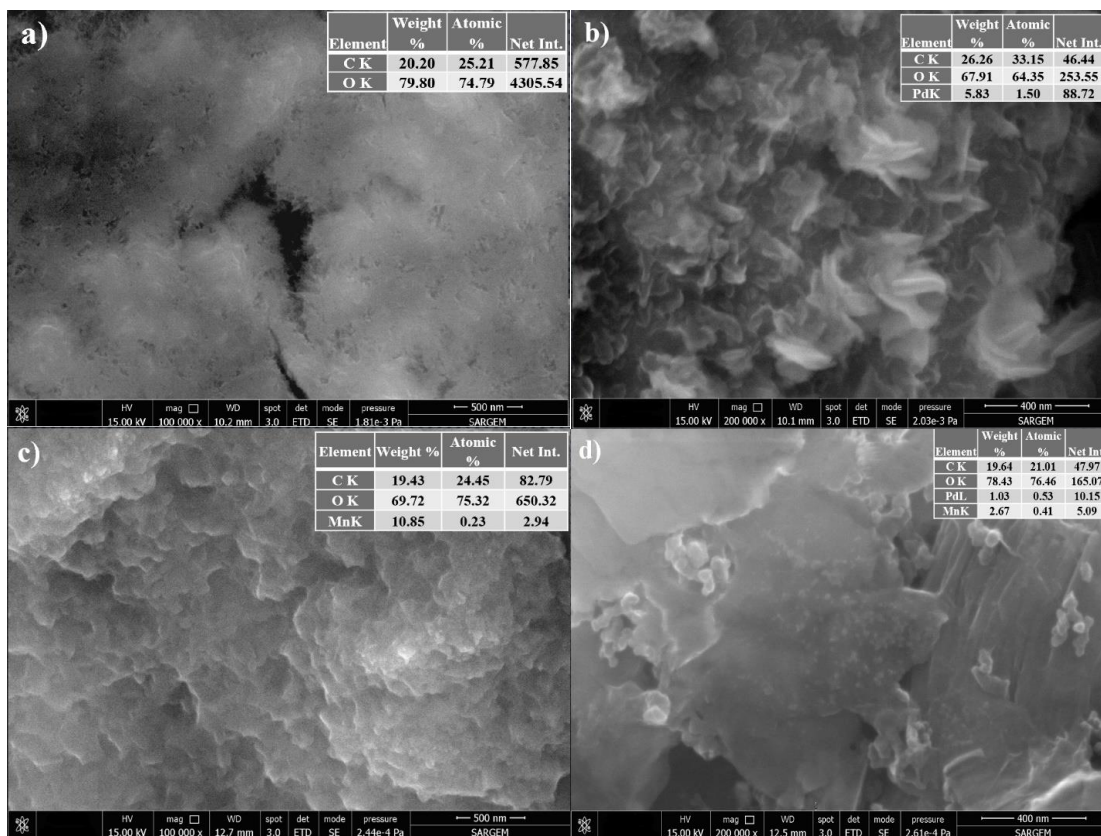
Figure 6.18. Surface analysis of electrodes after first discharge curve of a) rGO, b) rGO@Pd, c) rGO@α-MnO₂, and d) rGO@Pd@α-MnO₂ nancomposites air cathodes.

TEM was used to examine the morphology of the electrode surface for first discharge. The degradation of α-$MnO_2$ NWs enclosed by $Li_2O_2$ thin film is indicated by the surface of rGO coated with discharge products and rGO@α-$MnO_2$ electrodes, as shown in Figures 6.19a and 6.19b. The TEM image of toroid particles for the rGO/Pd electrode in Figure 6.19c is well match with the FESEM image in size range of 19-53 nm; comparable morphology has been observed in previous research [154]. Nanosized particles (11-22 nm) on the surface of rGO sheets and no signs of a change in the α-$MnO_2$ NWs structure are visible on the rGO@Pd@α-$MnO_2$ cathode surface (Figure 6.19d). On the surface of α-$MnO_2$, a thin film of discharge residue may be visible. It is possible that the emerging of Pd and α-$MnO_2$ increased cathode durability and prevented electrode breakdown due to lower charge-discharge potentials.
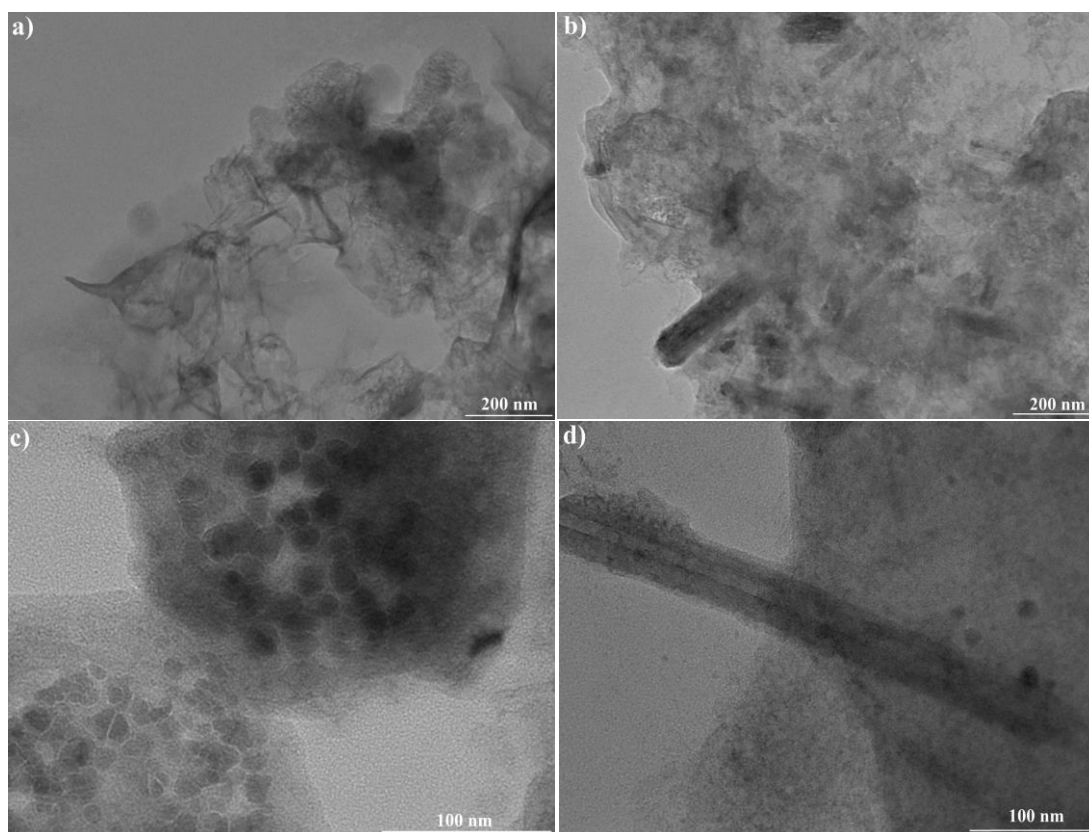
Figure 6.19. TEM images after initial full discharge for rGO (a), rGO@α-MnO$_2$ (b), rGO@Pd, and rGO@Pd@α-MnO$_2$ cathodes.

The generation of discharge products was confirmed by XRD patterns of the cathodes following full discharge, as shown in Figure 6.20a. Li$_2$O$_2$ (JCPDS, Card No. 09-0355), LiO$_2$ (JCPDS, Card No. 77-2144), and Li$_2$CO$_3$ (JCPDS, Card No. 22-1141) are the discharge product obtained once all cathodes have been fully discharged. The result shows the highest intensity peak of Li$_2$O$_2$ for rGO@Pd@α-MnO$_2$ among the as-produced cathodes, with 2θ values of 32.4$^o$ and 40$^o$, which are indexed to the planes of (1 0 0) and (1 0 0), respectively (1 0 2). At 21.3$^o$, 31.2$^o$, the weakest intensity peak was assigned to the planes of Li$_2$CO$_3$ (-1 1 0) and (0 0 2). Moreover, Raman spectral analysis of discharged cathodes confirmed the generation of Li$_2$O$_2$, Li$_2$CO$_3$, and LiO$_2$ with Raman shifts of 789, 1083, and 1133 cm$^{-1}$ for all discharged electrodes, respectively [162] (Figure 6.20b). On the other hand, rGO@Pd@α-MnO$_2$ electrode revealed a greater intensity peak associated with the Li$_2$O$_2$ component than rGO@Pd, rGO@α-MnO$_2$, and rGO, which is matched with the catalytic performance of the battery test.
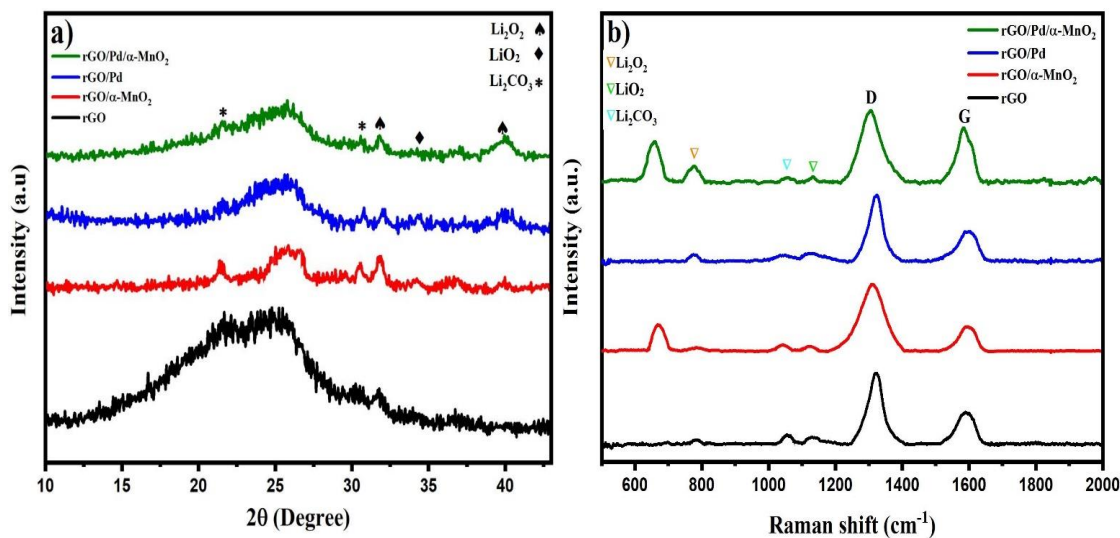
Figure 6.20. After full discharge electrochemical tests, the XRD pattern (a) and Raman spectra of cathodes.

XPS was used to analyze the composition of the discharge products further. The survey data of the cathodes after a initial discharge is shown in Figure 6.21a. The survey graph approved the presence of Li, C, and O. Pd and Mn peaks could be observed from the rGO@Pd@α-MnO$_2$ graph, which indicates the durability of the electrode upon the discharge. For all discharged electrodes ascribed to Li$_2$O$_2$, a peak at 54.3 eV binding energy can be observed in the high-resolution XPS spectra of Li 1s, which is in agreement at the binding energy of Li-O bond [163]. Because of the incorporation between Li and the rGO functional group, the peak identified at 55.2 eV is credited to Li$_2$CO$_3$. The highest intensity Li$_2$O$_2$ and Li$_2$CO$_3$ peaks in the Li 1s spectra corresponded to rGO@Pd@α-MnO$_2$ and rGO, respectively. To approve discharge residue, XPS O1s, and C1s data were evaluated. C 1s graph (Figure 6.21c) exhibited three parts that would allocate to the C–C bond derived from the rGO nanosheets, as well as to oxygen-functionalized components such as C–O (286 eV) and C=O (288.3 eV) modes, and a compound attributed to O–C=O bonds, showing the Li$_2$CO$_3$ formation. The strength of the O-C=O bond peak (289.7 eV) in the discharged rGO cathode's C 1s spectra is higher than in the C 1s graph of the other discharged electrodes. The O 1s graph of electrodes (Figure 6.21d) are match with the above data from Li 1s and C 1s. The production of Li$_2$O$_2$ and Li$_2$CO$_3$ is attributed to the peaks at 531.7 and 533 eV, respectively. Due to reduced polarization gab and very effective reaction kinetics by the distribution of Pd and α-MnO$_2$ catalysts, the

generation of $Li_2CO_3$ diminishes while $Li_2O_2$ formation increases in rGO@Pd@$\alpha$-$MnO_2$ electrodes discharged.

The cyclic voltammetry (CV) was performed to assess the additional catalytic performance of electrodes. CV scans of rGO, rGO@$\alpha$-$MnO_2$, rGO@Pd, and rGO@Pd@$\alpha$-$MnO_2$ cathodes were measured in the potential of 1.8-4.3 V, as given in Figure 6.22. CV scan of rGO@Pd@$\alpha$-$MnO_2$ air electrode (Figure 6.22d) indicates the ORR at 2.5 V and 2.9 V and two oxidative peaks detected at range 3-3.3 V and 3.6-3.8 V, suggesting the first charge voltage at 3.25 V due to discharge product decomposition and $Li_2O_2$ crystallites oxidation. Next, the second charge charge at 3.7 V was derived from bulk $Li_2O_2$ decomposition, and this peak in rGO is at 4 V. Simultaneously, the catalysts peak is moved toward a less charge voltage, as has been published by other teams. [164]. Furthermore, the current level of rGO@Pd@$\alpha$-$MnO_2$ in both cathodic and anodic scans was higher than the rGO (Figure 6.22a), implying increased formation and decomposition reaction kinetics of discharge products. The cathodic current level of rGO@$\alpha$-$MnO_2$ (Figure 6.22c) is almost less than the rGO@Pd cathode (Figure 6.22b), proposing reduced ORR activity of $MnO_2$ than that of rGO@Pd electrodes, while both reveal a high OER state.
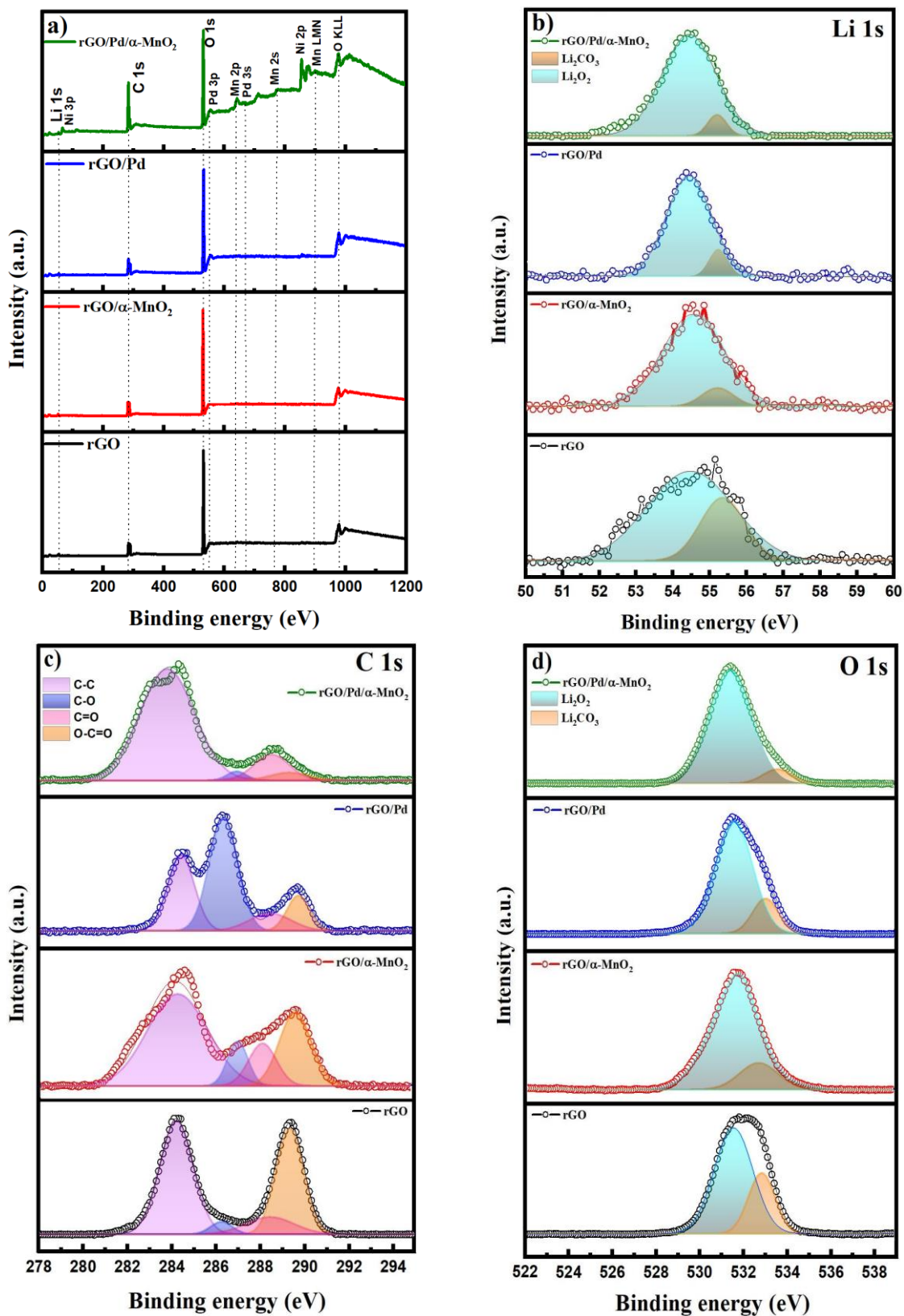
Figure 6.21. XPS data of electrodes after discharge, represets survey data (a) and high-resolution curve of Li 1s (b), C 1s (c), and O 1s (d).
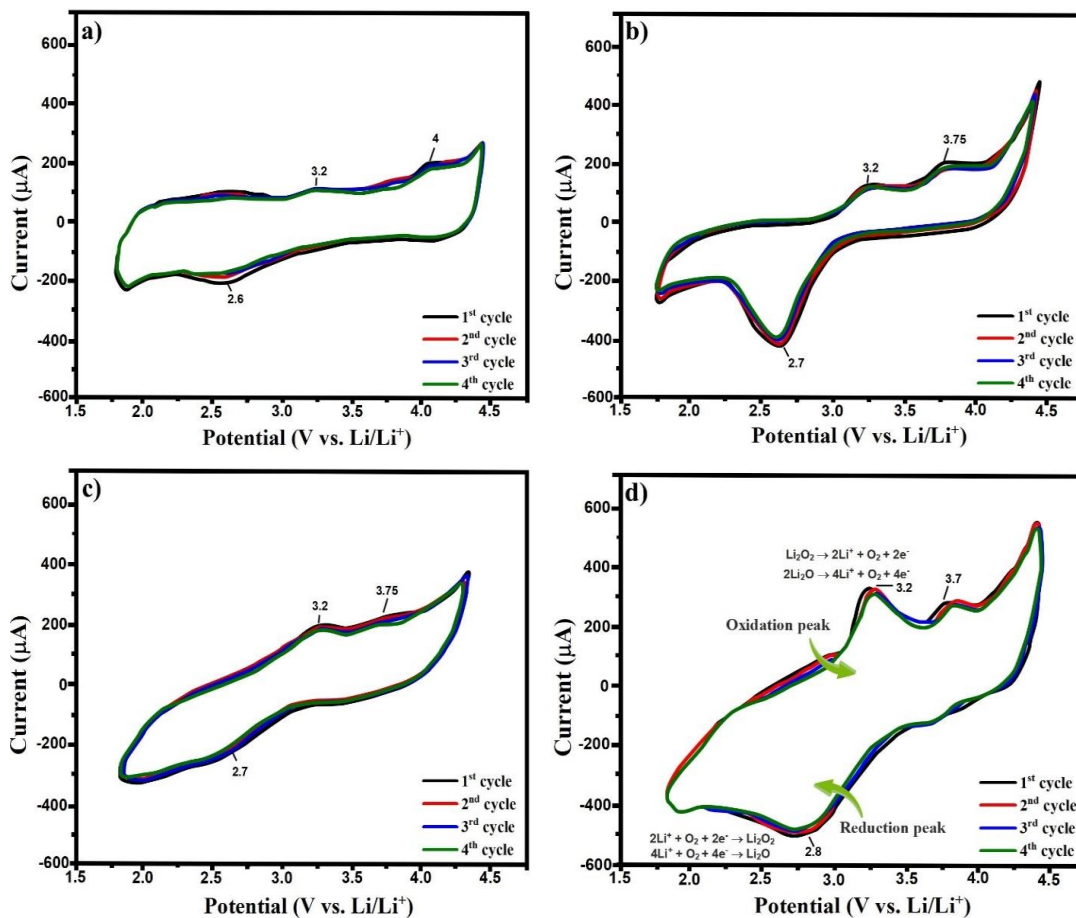
Figure 6.22. At a sweep speed of 0.3 mV s$^{-1}$, cyclic voltammetry of a) rGO, b) rGO@Pd, c) rGO@α-MnO$_2$, and d) rGO@Pd@α-MnO$_2$ electrodes was examined in the voltage between 1.8-4.3 V.

The charge/discharge profiles for the rGO@Pd, rGO@Pd@α-MnO$_2$, rGO@α-MnO$_2$, and rGO cathodes are examined at a fixed capacity of 800 mAh g$^{-1}$ with a constant current density of 100 mA g$^{-1}$ and is illustrated in Figure 6.23. As shown in Figure 6.23a. During the discharging-charging process, the rGO cathode shows low cyclability and a significant overpotential, resulting in the generation of parasite reactions such as Li$_2$CO$_3$. As a result, the cell's performance may decline. For OER at 4.2 V and ORR around 2.7 V, rGO@Pd and rGO@α-MnO$_2$ cathodes have lower polarization values (Figure 6.23b and 6.23c). Furthermore, the charge-discharge durability was maintained up to 40 and 30 cycles for rGO@Pd and rGO@α-MnO$_2$ electrodes, respectively. The charge potential drops to 3.2 V when α-MnO$_2$ and Pd catalysts are added to the structure, but the discharge voltage rises to 2.8 V. The Li$_2$O$_2$ production and breakdown rates are accelerated by the reduced polarization gap. It improves the charge/discharge capacity for 50 cycles in a steady manner

(Figure 6.23d). Table 6.4 presents the cyclabity of graphene-based hybrids cathodes from prior studies. It demonstrated that the capacity and cyclability of rGO@Pd@α-MnO$_2$ of this study is high. The decline in carbon degradation throughout cycling, which inhibits side reactions including Li$_2$CO$_3$, is likely to generate such enhancement due to the decrease in carbon content and bifunctional catalyst activity. Additionally, graphene sheets can provide a smooth path for the transmission of oxygen and electrons, while Pd and α-MnO$_2$ have many active points for electrochemical reactions, lowering the charge overpotential associated with Li$_2$O$_2$ breakdown and extending the cell's life cycle.
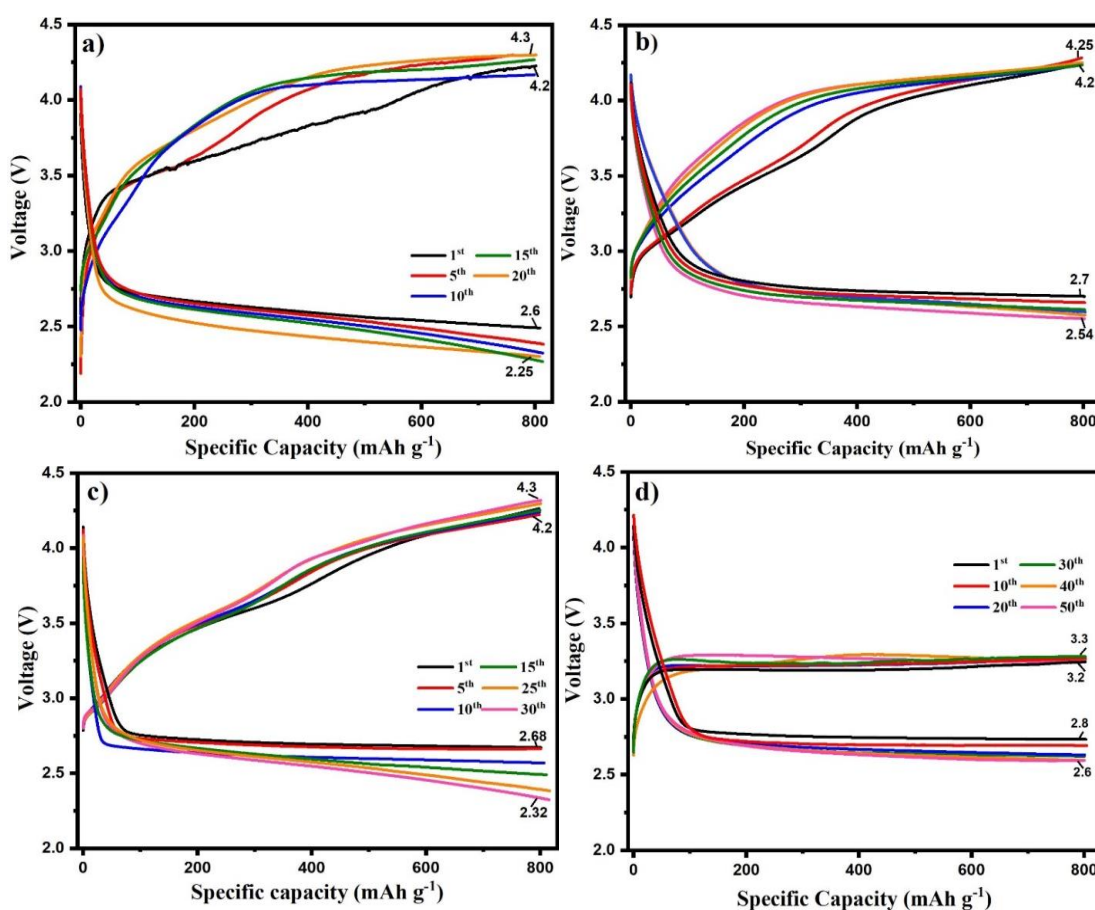


Figure 6.23. rGO (a), rGO@Pd (b), rGO@α-MnO$_2$ (c), and rGO@Pd@α-MnO$_2$ (d) cycling performance at fixed capacity of 800 mAh g$^{-1}$ for 7 hours.

Table 6.4. Previous publications on the cyclability of graphene-based nanocomposites cathodes. (Carbon black, CB)

| Cathode material | current | Specific capacity | Cycles | Graphene contents | Ref. |
|---|---|---|---|---|---|
| $La_{0.8}Sr_{0.2}Co_{0.8}Fe_{0.2}O_3$@N-rGO | 400 mA $g^{-1}$ | 500 mAh $g^{-1}$ | 52 | - | [165] |
| rGO/CoAl | 100 mA $g^{-1}$ | 500 mAh $g^{-1}$ | 30 | 29.6% | [166] |
| $LaCo_{0.8}Fe_{0.2}O_3$@rGO | 200 mA $g^{-1}$ | 500 mAh $g^{-1}$ | 56 | 15.5%+40% CB | [167] |
| PdSnCo/NG | 0.3 mA $cm^{-2}$ | 500 mAh $g^{-1}$ | 60 | 85% | [168] |
| G/$Co_3O_4$ | 160 mA $g^{-1}$ | 200 mAh $g^{-1}$ | 50 | - | [169] |
| rGO/$Co_3O_4$ | 0.1 mA $cm^{-2}$ | 500 mAh $g^{-1}$ | 39 | 30.7%+66.6%CB | [170] |
| PdNDS/GNP/GO | 200 mA $g^{-1}$ | 500 mAh $g^{-1}$ | 30 | 61.3% | [171] |
| rGO@Pd@$\alpha$-$MnO_2$ | 100 mA $g^{-1}$ | 800 mAh $g^{-1}$ | 50 | 50% | This work |

The optical photo of the disassembled Li-$O_2$ test cell is shown in Figure 6.24 to explain the poor cycle life of the cell, despite the good catalytic influence achieved by Pd and $MnO_2$ catalyst. Lithium metal is corroded, as observed Figure 6.24b, most likely because of oxygen coming from cathode and reacting with the electrolyte (Figure 6.24a). It's possible that to get a good cyclability, the lithium metal require to be preserved from corrosion and a low volatile electrolyte constructed.
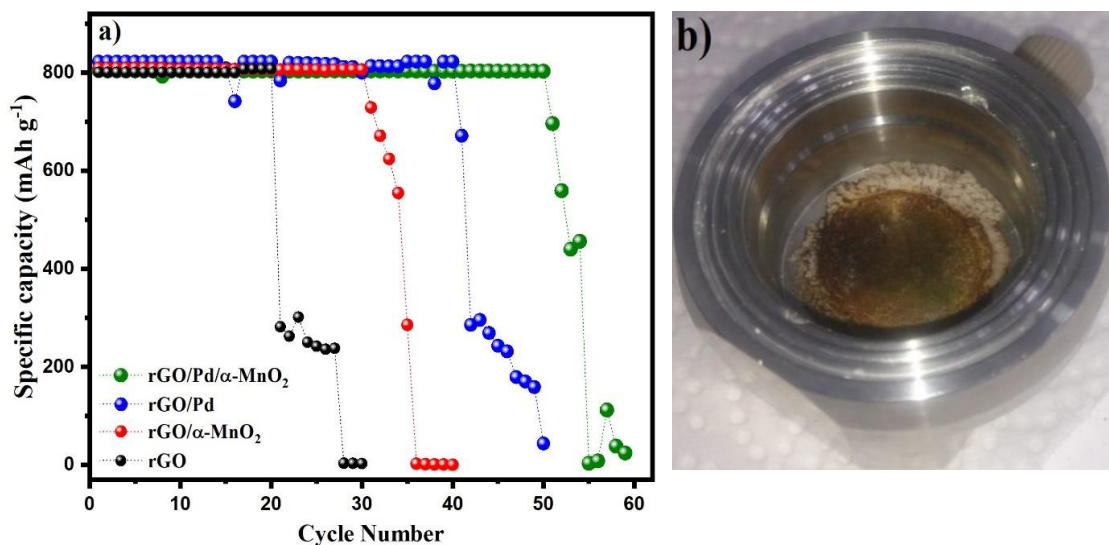
Figure 6.24. a) Comparison of electrode cycling data at a fixed capacity of 800 mAh g$^{-1}$, and b) optical photo of the cell after test revealing Li foil deterioration.

## 6.3. Physical Characterization Of Virus-Templated MnO$_2$

The morphology of v-MnO$_2$ (viral templated MnO$_2$) and rGO / v-MnO$_2$ was observed under FESEM (field emission electron microscopy). V-MnO$_2$ nanowires were prepared with urchin surface morphology by the moderate and easy chemical reaction by using M13 phage. M13 phages were utilized as versatile models to equip high aspect ratio nanowires to prepare with safe conditions. The MnO$_2$ formation is due to electrostatic interactions between the negative charge of functional groups and the opposite charge of Mn$^{2+}$ ions of p8 protein coat on the phage surface.

These v-MnO$_2$ nanowires revealed urchin-like morphology on the surface of virus (FESEM image in Figure 6.25 a,b), therefore designing this rough surface of materials expected to enhance Li-O$_2$ cell performance. Figures 6.25 c,d indicate the v-MnO$_2$ nanowires are incorporated on the graphene sheets. EDS spectra of both samples identified the presence of Mn and O.
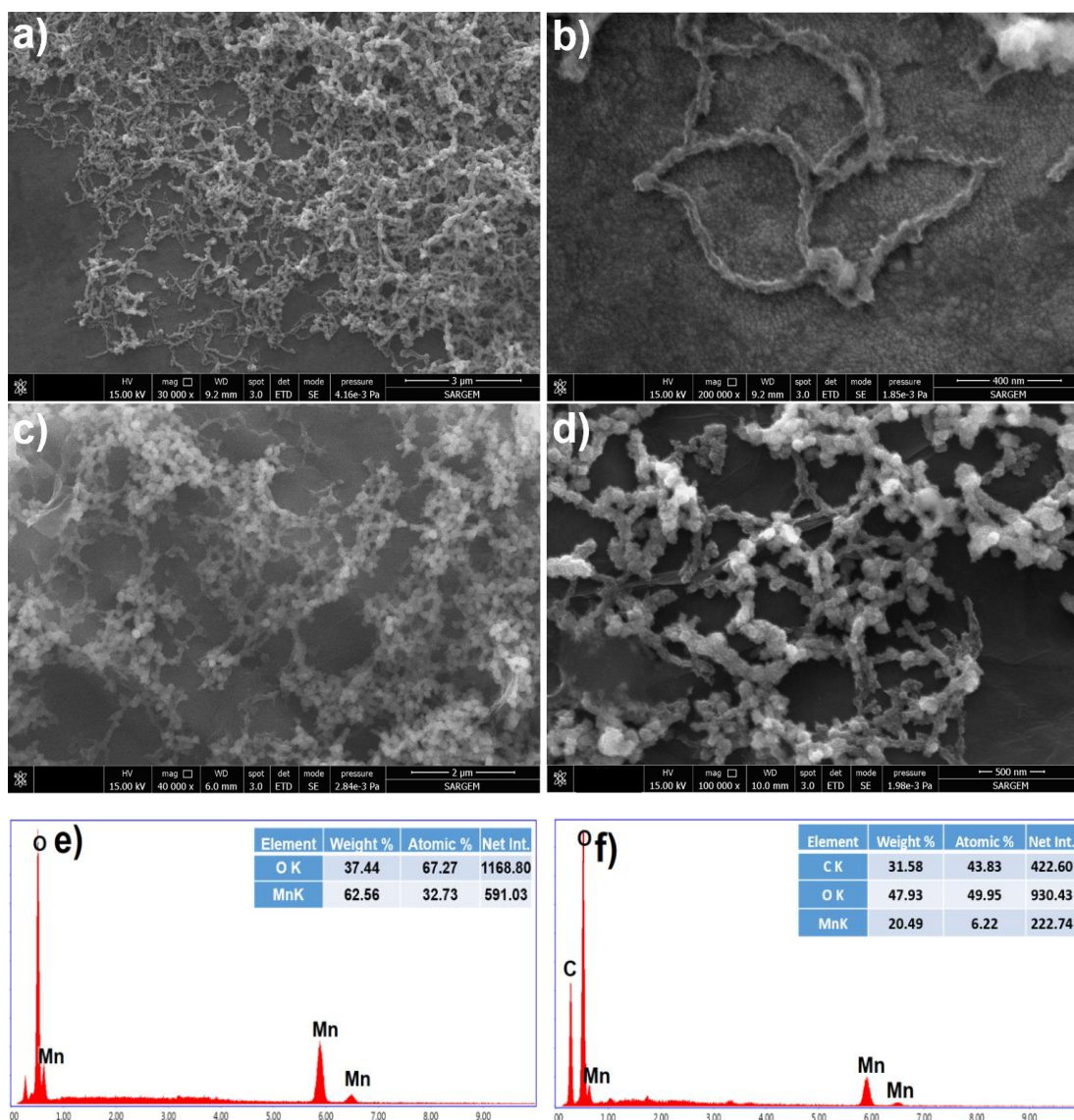
Figure 6.25. FESEM images of v-MnO₂ nanowires (a,b) and v-MnO₂/rGO (b,c). EDS spectra of v-MnO₂ nanowires (e) and v-MnO₂/rGO (f).

The crystallographic structure of v-MnO$_2$/rGO was detected with X-ray diffraction (XRD) (Figure 6.26a). First, the XRD pattern illustrated peaks centred at 2θ of 12.3°, 18.4°, 28.6°, 37.1°, 41.6°, 51°, 54.3°, 60.4°, and 71.9° matching to planes of α-MnO$_2$ (powder diffraction file number 44-0141). A broad peak at 2ɵ 24.5° is attributed to graphene layers. Raman spectroscopy was done, as shown in Figure 5.25b. In Raman spectra of the v-MnO$_2$/rGO the two peaks at 473 cm$^{-1}$ and 655 cm$^{-1}$ are attributed to stretching vibration of the Mn-O and Mn-O-Mn bonds. The weak peaks observed at 367 cm$^{-1}$ originated from the formation of Mn$_2$O$_3$ or Mn$_3$O$_4$ correspond to the bending mode of O-Mn-O. Therefore, the Raman peaks of v-MnO$_2$/rGO are ascribed

to the $MnO_2$ nanostructures. Moreover, the peaks at 1580.6 $cm^{-1}$ and 1316.3 $cm^{-1}$ are assigned to G-band and D band of graphene.
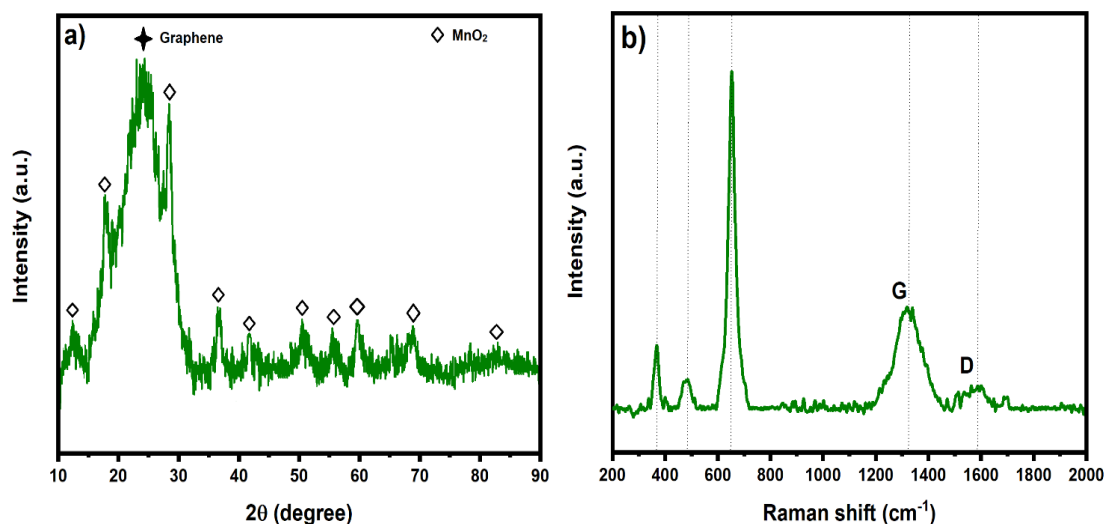


Figure 6.26. The XRD (a) and Raman (b) specta of v-$MnO_2$/rGO.

## 6.4. Electrochemical Tests Of Virus-Templated $MnO_2$ And Supported On Graphene Electrodes

To study the electrochemical activity of v-$MnO_2$/rGO electrode, the full charge-discharge test was carried out at a current density of 100 $mAg^{-1}$ at the voltage range of 2-4.3 V (Figure 6.27a). The v-$MnO_2$/rGO electrode exhibited a high specific capacity of about 7000 mAh $g^{-1}$, which is higher than the previous $MnO_2$/rGO (4500 mAh $g^{-1}$). The onset charge and discharge potentials were 3.7 V and 2.8 V, respectively. The low over charge-discharge could be due to enhanced formation and decomposition of $Li_2O_2$ attributed to rough morphology of $MnO_2$, which accelerated $O_2$ diffusion and led to better ORR and OER.

The cycling performance of the v-$MnO_2$/rGO nanowires cathode was evaluated with the capacity limited at 800 mAh $g^{-1}$. Figure 6.27(b) represents cycling performance up to 45. As shown in Figure 6.27b, the first discharge and charge plateau of v-$MnO_2$/rGO catalyzed Li-$O_2$ battery at a fixed capacity of 800 mAh $g^{-1}$ is about 2.81

V and 3.9 V, respectively; that reveals the mass of suitable reactant molecules with mass efficiency, and transfer decomposition and deposition of $Li_2O_2$ at the electrode. Then, after 45 cycles, the v-$MnO_2$ / rGO cathode discharge voltages decrease to 2.67 V. The results may be related to slow passivation of the cathode at most due to decreased cathode surface connectivity and expanded coverage of the activity sites due to $Li_2O_2$. Meantime, through the complete charge and discharge process, it does not show the voltage increase in the charge and keeps below 4.15 V, which then shows the excellent catalytic performance of OER for v-$MnO_2$ / rGO cathode.
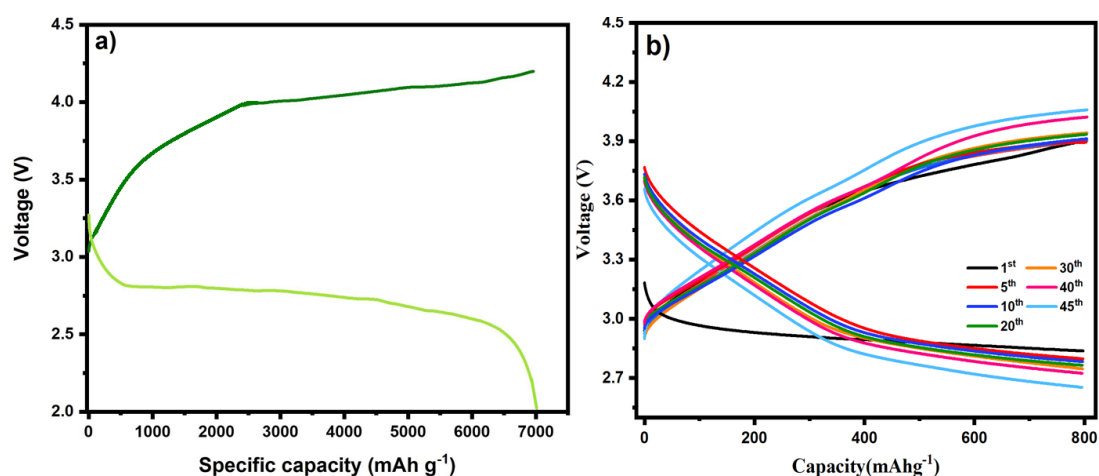


Figure 6.27. Full discharge and charge curves of v-$MnO_2$/rGO (a) and its cycling performance at limited capacity 800 mAh $g^{-1}$ (b).

Figure 6.28 represents the electrochemical impedance spectra (EIS) of v-$MnO_2$/rGO before and after the first discharge and charge test. The EIS plot is comprised of three frequency regions; the high frequency region is relevant to the ohmic resistance ($R_s$), which is linked to the electrolyte, current collector, and cell. The middle frequency ($R_{int}$) is ascribed to the charge-transfer between the electrolyte and air cathode interface, and covering the catalysts by discharge products layer increases this resistance. The low frequency region represents the diffusion process that generates a Warburg tail. During discharge, the $R_{int}$ value of Bio-$MnO_2$ increased from 264 $\Omega$ to 850 $\Omega$, which is likely due to the formation of discharge products on the cathode. During charge, $R_{int}$ reduced to $\approx$310 $\Omega$ close to the pristine cell resistance, displaying the reversibility of the charge-discharge process.
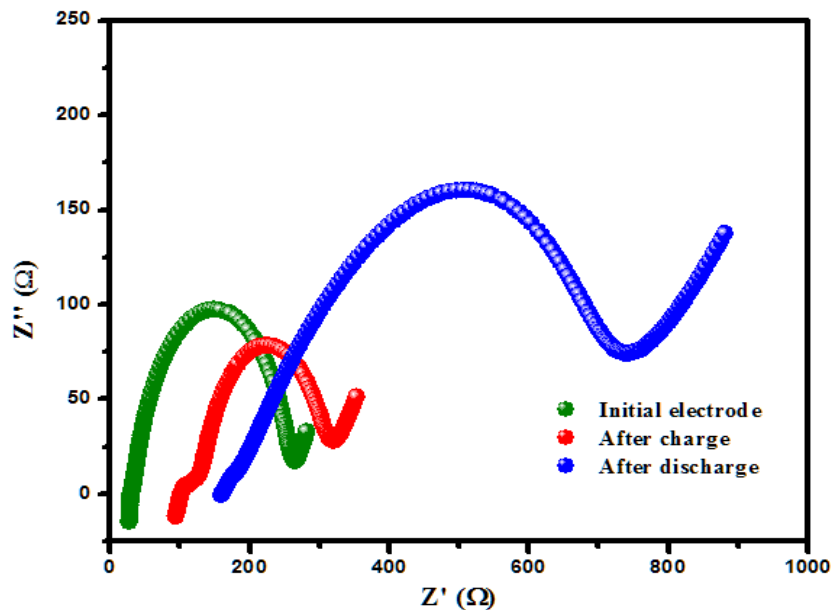
Figure 6.28. The EIS spectra of v-MnO$_2$/rGO electrode.

The XRD and FESEM were performed for v-MnO$_2$/rGO electrodes after the first full discharge and charge state to determine the discharge product and its morphology. The FESEM images of the electrode after first discharge show the film-like Li$_2$O$_2$ products (Figure 6.29a,b). It is noted that this morphology of Li$_2$O$_2$ improved OER due to better decomposition, therefore enhancing the specific capacity and round-trip efficiency. The XRD pattern after discharge confirms the formation of Li$_2$O$_2$ indexed to JCPD card no. 09-0355. However, the other side reactions were observed in XRD pattern approving the decomposition of carbon materials.
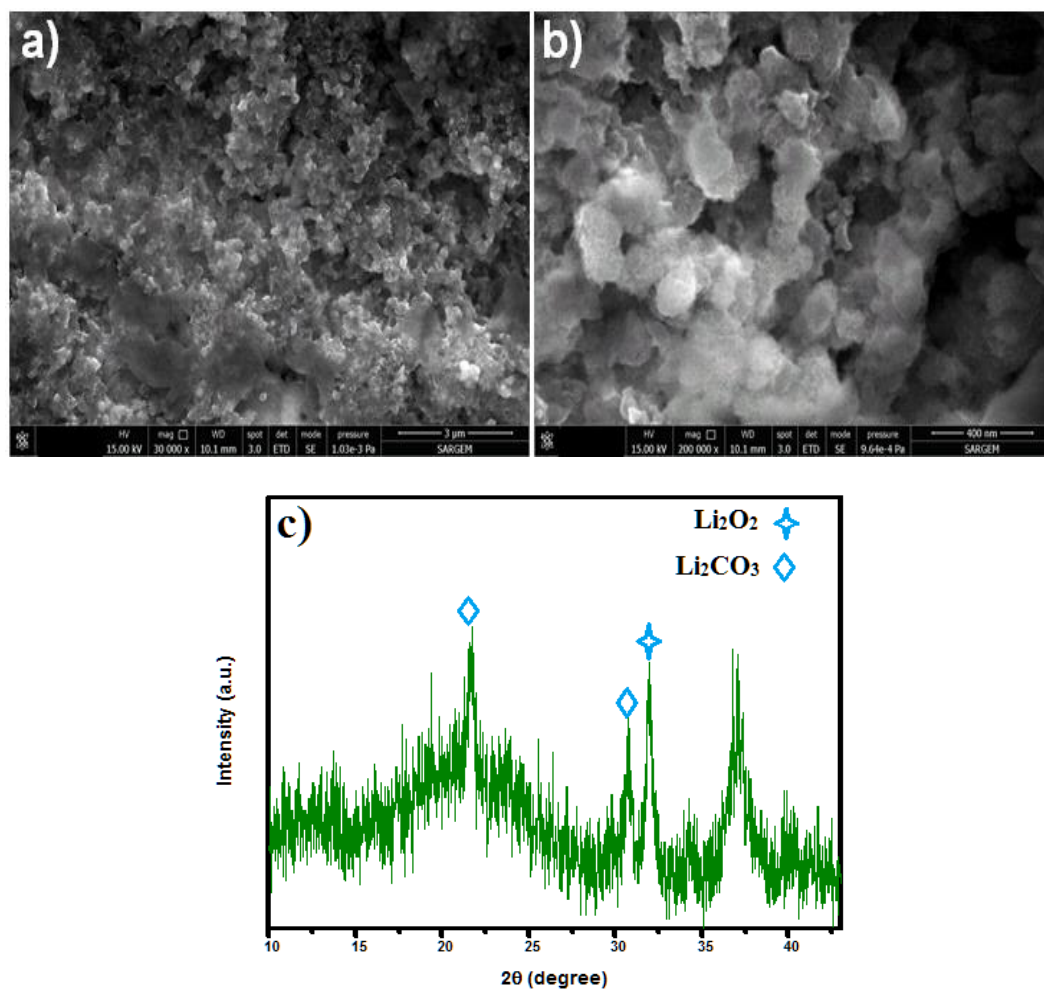
Figure 6.29. The FESEM images of v-MnO$_2$/rGO electrode in high (a) and low (b) magnification after cycling. XRD spectra of v-MnO$_2$/rGO electrode after cycling (c).

# CHAPTER 7. GENERAL CONCLUSIONS AND SOLUTIONS

## 7.1. General conclusions

High energy needs caused by the spread of humankind's demand for electronic devices and electric cars have prompted discovery and development of future rechargeable batteries with exceptional performance. The fundamental reversible reaction of $2Li^+ + O_2 + 2e^- = Li_2O_2$ ($E^0 = 2.96$ V against $Li/Li^+$) in lithium-oxygen batteries can produce a better theoretical energy density of 11,680 Wh $Kg^{-1}$, making them an attractive choice for future rechargeable batteries. Due to slow oxygen reduction/evolution reactions (ORR/OER) kinetics during (dis)charge operations, the isolated $Li_2O_2$ generates a significant polarization, low round-trip efficiency, and limited cycle life. The major hurdle for the actual implementation of $Li-O_2$ systems is cyclability. The limited lifetime of Li-O2 cells is due to cathode passivation, electrolyte dissolution, corrosion, and dendritic growth of lithium. As a result, a high-performance $Li-O_2$ battery relies heavily on the use of a stable electrolyte, lithium safety, and effective bifunctional catalysts with a sensible architecture. Because of crucial role of catalysts in accelerating ORR/OER kinetics, they have received more attention than other components of the $Li-O_2$ cell. Several experiments have been described to replace carbonaceous materials in the presence of $Li_2O_2$, which causes irreversible lithium carbonate ($Li_2CO_3$) and other byproducts at the interface [172,173]. These chemical intermediates generate a significant overpotential and inhibit the oxygen and electrolyte pathways, reducing the cell's capacity and shortening its life cycle. Carbon materials, on the other hand, are commonly utilized in batteries because of their large surface area, easy fabrication, porous, and low price.

Therefore, in this research, the focus was on designing enhanced cathode air

electrodes to overcome the limitations of current lithium-oxygen batteries by utilizing high-efficiency nanocatalysts assembled by reduced graphene oxide (rGO) nanocomposites. Graphene oxide (GO) was prepared by modified hummers method, followed by deposition of Pd nanoparticles on the surface of GO, due to the strong interactions between cationic $Pd^{2+}$ and the oxygen functional groups (hydroxyl, epoxy and carboxyl groups) on the surface and the edge of the GO sheets, then a reduction of GO in a reducing agent solution. And preparation of a $Ru/MnO_2$ mixed with rGO to understand the different electrochemical behavior of Ru and Pd. The prepared samples were characterized by X-ray diffraction (XRD), Raman spectroscopy, Field emission scanning microscopy (FESEM), Energy dispersive X-ray spectroscopy (EDS), and thermogravimetric analysis (TGA).

In conclusion, $Ru/\alpha\text{-}MnO_2$ supported on rGO have been dispersed and used in the rechargeable Li−air cells as air cathodes, and their catalytic performance was evaluated. $rGO/Ru/\alpha\text{-}MnO_2$ tested indicated reduction in charging overpotential resulted in a longer life cycle than $Ru/\alpha\text{-}MnO_2$. $rGO/Ru/\alpha\text{-}MnO_2$ hybrid cathode exhibited the most stable cycling and the lowest overpotentials in ORR reaction, remarkably reducing discharge potential to 2.8 V from 2.6 V for $Ru/\alpha\text{-}MnO_2$ electrode at full discharge profile due to higher conductivity and larger surface area of graphene. These results emphasize the importance of conductivity and surface area parameters in the electrochemical performance of the battery.

Pd nanosized particles and $\alpha\text{-}MnO_2$ NWs incorporated with rGO sheets are fabricated via a facile reduction process. $rGO@Pd@\alpha\text{-}MnO_2$ hybrids indicate high specific capacity of 7500 mAh $g^{-1}$ and low discharge/charge voltages in comparison with the rGO electrode. Besides, $rGO@Pd@\alpha\text{-}MnO_2$ electrode could be maintained for 50 cycles at fixed capacity 800 mAh $g^{-1}$ with no capacity decay. Moreover, the $Li_2O_2$ shape has been changed by lowering the carbon content and using a bifunctional catalyst, and increasing the oxygen reduction reaction leads to increased capacity. Our findings demonstrate the better catalytic performance of $rGO@Pd@\alpha\text{-}MnO_2$ nanostructures as an electrocatalyst and suggest that $Li\text{-}O_2$ batteries have a bright future.

## 7.2. Solutions

In conclusion, electrocatalyst development and mechanism investigation for high-performance lithium oxygen batteries have made significant progress. The results indicate that $Li-O_2$ cell failure is due to a lack of cell components and the accumulation of side products induced by various parasitic reactions rather than insufficient cathode catalyst activity.  However, we have faced some main issues, including lithium anode corrosion, electrolyte evaporation, binder degradation, and carbon decomposition, restricting the battery's lifespan.

The binder is primarily wrapped on the surface of cathode materials, which are easily attacked by oxygen species. In addition, the decomposition of the binder can result in cathode passivation and active material exfoliation. As a result, selecting a long-lasting binder is critical for enhancing battery cycle stability. Also, to avoid side effect of binder degradation, free-binder cathodes have been developing. An aerogel preparation can be an alternative solution to prepare free-standing graphene to enhance electrolyte permeation and oxygen diffusion.

Defects on the carbon surface account for the electrolyte's and carbon's rapid decomposition. As a result, successful steps such as the fabrication of a protective layer or high-temperature annealing can be used to passivate or remove defects on the carbon surface. The coating carbon surface will suppress side reactions while also acting as a catalyst, improving cell efficiency and stability at the same time.

To protect the lithium from corrosion, the coating layer can be developed. Other strategies can be designing a ceramic separator or solid-state electrolyte.

# REFERENCES

[1]     Wang, Z.L., Xu, D., Xu, J.J., Zhang, X.B., Oxygen electrocatalysts in metal-air batteries: From aqueous to nonaqueous electrolytes, 2014.

[2]     Luo, L., Liu, B., Song, S., Xu, W., Zhang, J.G., Wang, C., Revealing the reaction mechanisms of Li-$O_2$ batteries using environmental transmission electron microscopy. Nat. Nanotechnol. 12 (6): 2017.

[3]     Cheng, F., Liang, J., Tao, Z., Chen, J., Functional materials for rechargeable batteries. Adv. Mater. 23 (15): 2011.

[4]     Stock, J.T., Electrochemistry in retrospect: an overview. In: ACS Symposium Series. 1989.

[5]     Berckmans, G., Messagie, M., Smekens, J., Omar, N., Vanhaverbeke, L., Mierlo, J. Van, Cost projection of state of the art lithium-ion batteries for electric vehicles up to 2030. Energies. 10 (9): 2017.

[6]     May, G.J., Maleschitz, N., Diermaier, H., Haeupl, T., The optimisation of grid designs for valve-regulated lead/acid batteries for hybrid electric vehicle applications. J. Power Sources. 195 (14): 2010.

[7]     Shen, X., Liu, H., Cheng, X.B., Yan, C., Huang, J.Q., Beyond lithium ion batteries: Higher energy density battery systems based on lithium metal anodes, 2018.

[8]     Cheng, X.B., Zhang, R., Zhao, C.Z., Zhang, Q., Toward safe lithium metal anode in rechargeable batteries: A Review, 2017.

[9]     European Commission, The Paris Protocol - A blueprint for tackling global climate change beyond 2020. J. Eur. Comm. 81: 2015.

[10]    Herranz, J., Garsuch, A., Gasteiger, H.A., Using rotating ring disc electrode voltammetry to quantify the superoxide radical stability of aprotic Li-air battery electrolytes. J. Phys. Chem. C. 2012.

[11]    IPCC, Summary for Policymakers, In: Climate Change 2014, Mitigation of Climate Change. Contribution of Working Group III to the Fifth Assessment Report of the Intergovernmental Panel on Climate Change. 2014.

[12]     Berciaud, S., Ryu, S., Brus, L., Heinz, T., Probing the intrinsic properties of exfoliated graphene: raman spectroscopy of free-standing monolayers. Nano Lett. 2008.

[13]     Ji, X., Lee, K.T., Nazar, L.F., A highly ordered nanostructured carbon-sulphur cathode for lithium-sulphur batteries. Nat. Mater. 8 (6): 2009.

[14]     Padbury, R., Zhang, X., Lithium-oxygen batteries - Limiting factors that affect performance, 2011.

[15]     Pakseresht, S., Cetinkaya, T., Al-Ogaili, A.W.M., Akbulut, H., Urchin-like core-shell $TiO_2$/α-$MnO_2$ nanostructures as an active catalyst for rechargeable lithium-oxygen battery. Adv. Powder Technol. 2021.

[16]     Bruce, P.G., Freunberger, S.A., Hardwick, L.J., Tarascon, J.-M., Erratum: Li–$O_2$ and Li–S batteries with high energy storage. Nat. Mater. 11 (2): 2012.

[17]     Sidhu, S.S., Engineering M13 for phage display. Biomol. Eng. 18 (2): 57–63, 2001.

[18]     Elbing, K.L., Brent, R., Recipes and Tools for Culture of Escherichia coli. Curr. Protoc. Mol. Biol. 125 (1): 2019.

[19]     Lin, H.S., Lee, J.M., Han, J., Lee, C., Seo, S., Tan, S., Lee, H.M., Choi, E.J., Strano, M.S., Yang, Y., Maruyama, S., Jeon, I., Matsuo, Y., Oh, J.W., Denatured M13 Bacteriophage-Templated Perovskite Solar Cells Exhibiting High Efficiency. Adv. Sci. 7 (20): 2020.

[20]     Kim, I., Moon, J.S., Oh, J.W., Recent advances in M13 bacteriophage-based optical sensing applications, 2016.

[21]     Park, I.W., Kim, K.W., Hong, Y., Yoon, H.J., Lee, Y., Gwak, D., Heo, K., Recent developments and prospects of M13-bacteriophage based piezoelectric energy harvesting devices, 2020.

[22]     Lee, Y.J., Yi, H., Kim, W.J., Kang, K., Yun, D.S., Strano, M.S., Ceder, G., Belcher, A.M., Fabricating genetically engineered high-power lithium-ion batteries using multiple virus genes. Science (80-. ). 324 (5930): 1051–1055, 2009.

[23]     Lee, B.Y., Zhang, J., Zueger, C., Chung, W.J., Yoo, S.Y., Wang, E., Meyer, J., Ramesh, R., Lee, S.W., Virus-based piezoelectric energy generation. Nat. Nanotechnol. 7 (6): 2012.

[24]     Cho, Y.K., Wartena, R., Tobias, S.M., Chiang, Y.M., Self-assembling colloidal-scale devices: Selecting and using short-range surface forces between conductive solids. Adv. Funct. Mater. 17 (3): 2007.

[25]    Ki, T.N., Wartena, R., Yoo, P.J., Liau, F.W., Yun, J.L., Chiang, Y.M., Hammond, P.T., Belcher, A.M., Stamped microbattery electrodes based on self-assembled M13 viruses. Proc. Natl. Acad. Sci. U. S. A. 105 (45): 2008.

[26]    Al-Ogaili, A.W.M., Cetinkaya, T., Pakseresht, S., Akbulut, H., Graphene-based nanocomposite cathodes architecture with palladium and α-MnO$_2$ for high cycle life lithium-oxygen batteries. J. Alloys Compd. 854: 2021.

[27]    Christy, M., Arul, A., Kim, Y.B., Carbide composite nanowire as bifunctional electrocatalyst for lithium oxygen batteries. Electrochim. Acta. 2019.

[28]    Christy, M., Arul, A., Zahoor, A., Moon, K.U., Oh, M.Y., Stephan, A.M., Nahm, K.S., Role of solvents on the oxygen reduction and evolution of rechargeable Li-O$_2$ battery. J. Power Sources. 2017.

[29]    Goodenough, J.B., Kim, Y., Challenges for rechargeable Li batteries, 2010.

[30]    Li, Y., Dai, H., Recent advances in Zinc-air batteries, Chem. Soc. Rev., 2014.

[31]    Xu, Y.F., Chen, Y., Xu, G.L., Zhang, X.R., Chen, Z., Li, J.T., Huang, L., Amine, K., Sun, S.G., RuO$_2$ nanoparticles supported on MnO$_2$ nanorods as high efficient bifunctional electrocatalyst of lithium-oxygen battery. Nano Energy. 28: 2016.

[32]    Deiss, E., Holzer, F., Haas, O., Modeling of an electrically rechargeable alkaline Zn-air battery. Electrochim. Acta. 47 (25): 2002.

[33]    Ding, N., Chien, S.W., Hor, T.S.A., Lum, R., Zong, Y., Liu, Z., Influence of carbon pore size on the discharge capacity of Li-O$_2$ batteries. J. Mater. Chem. A. 2 (31): 2014.

[34]    Zhang, X.G., Fibrous zinc anodes for high power batteries. J. Power Sources. 163 (1 SPEC. ISS.): 2006.

[35]    Lee, J.S., Kim, S.T., Cao, R., Choi, N.S., Liu, M., Lee, K.T., Cho, J., Metal-air batteries with high energy density: Li-air versus Zn-air, Adv. Energy Mater., 2011.

[36]    Aricò, A.S., Bruce, P., Scrosati, B., Tarascon, J.M., Van Schalkwijk, W., Nanostructured materials for advanced energy conversion and storage devices, Nat. Mater., 2005.

[37]    Bruce, P.G., Hardwick, L.J., Abraham, K.M., Lithium-air and lithium-sulfur batteries. MRS Bull. 36 (7): 2011.

[38]    Black, R., Adams, B., Nazar, L.F., Non-Aqueous and Hybrid Li-O$_2$ Batteries. Adv. Energy Mater. 2 (7): 801–815, 2012.

[39]    Débart, A., Paterson, A.J., Bao, J., Bruce, P.G., α-MnO$_2$ nanowires: A catalyst for the O$_2$ electrode in rechargeable lithium batteries. Angew. Chemie - Int. Ed. 47 (24): 2008.

[40]    Abraham, K.M., Jiang, Z., A polymer electrolyte-based rechargeable lithium / oxygen battery. J. Electrochem. Soc. 143 (1): 1996.

[41]    Ogasawara, T., Débart, A., Holzapfel, M., Novák, P., Bruce, P.G., Rechargeable Li$_2$O$_2$ electrode for lithium batteries. J. Am. Chem. Soc. 128 (4): 2006.

[42]    Girishkumar, G., McCloskey, B., Luntz, A.C., Swanson, S., Wilcke, W., Lithium-air battery: Promise and challenges. J. Phys. Chem. Lett. 1 (14): 2010.

[43]    Feng, N., He, P., Zhou, H., Critical Challenges in Rechargeable Aprotic Li-O$_2$ Batteries, 2016.

[44]    Dou, S., Tao, L., Huo, J., Wang, S., Dai, L., Etched and doped Co9S8/graphene hybrid for oxygen electrocatalysis. Energy Environ. Sci. 9 (4): 2016.

[45]    Dubin, S., Gilje, S., Wang, K., Tung, V.C., Cha, K., Hall, A.S., Farrar, J., Varshneya, R., Yang, Y., Kaner, R.B., A one-step, solvothermal reduction method for producing reduced graphene oxide dispersions in organic solvents. ACS Nano. 4 (7): 2010.

[46]    Wu, J., Ma, L., Yadav, R.M., Yang, Y., Zhang, X., Vajtai, R., Lou, J., Ajayan, P.M., Nitrogen-doped graphene with pyridinic dominance as a highly active and stable electrocatalyst for oxygen reduction. ACS Appl. Mater. Interfaces. 7 (27): 2015.

[47]    S.J. Visco, E. Nimon, B. Katz, L. Jonghe, M.Y.C., The Electrochemical Society Meeting. In: Books of Abstract, The Electrochemical Society Meeting. p. Abstract-0389 , Cancun, Mexico, 2006.

[48]    VISCO, J., S., NIMON, Yevgeniy, S., KATZ, Bruce, D., Ionically conductive composites for protection of active metal anodes.

[49]    Zhang, T., Imanishi, N., Hasegawa, S., Hirano, A., Xie, J., Takeda, Y., Yamamoto, O., Sammes, N., Li∕Polymer Electrolyte∕Water Stable Lithium-Conducting Glass Ceramics Composite for Lithium–Air Secondary Batteries with an Aqueous Electrolyte. J. Electrochem. Soc. 155 (12): 2008.

[50]    Martin, J.J., Neburchilov, V., Wang, H., Qu, W., Air cathodes for metal-air batteries and fuel cells. In: 2009 IEEE Electrical Power and Energy Conference, EPEC 2009. 2009.

[51] Imanishi, N., Luntz, A.C., Bruce, P., The lithium air battery: Fundamentals. 2014.

[52] Lim, H.D., Lee, B., Bae, Y., Park, H., Ko, Y., Kim, H., Kim, J., Kang, K., Reaction chemistry in rechargeable Li-O$_2$ batteries, 2017.

[53] Zhang, T., Imanishi, N., Hasegawa, S., Hirano, A., Xie, J., Takeda, Y., Yamamoto, O., Sammes, N., Water-stable lithium anode with the three-layer construction for aqueous lithium-air secondary batteries. Electrochem. Solid-State Lett. 12 (7): 2009.

[54] Hasegawa, S., Imanishi, N., Zhang, T., Xie, J., Hirano, A., Takeda, Y., Yamamoto, O., Study on lithium/air secondary batteries-Stability of NASICON-type lithium ion conducting glass-ceramics with water. J. Power Sources. 189 (1): 2009.

[55] Shimonishi, Y., Zhang, T., Johnson, P., Imanishi, N., Hirano, A., Takeda, Y., Yamamoto, O., Sammes, N., A study on lithium/air secondary batteries-Stability of NASICON-type glass ceramics in acid solutions. J. Power Sources. 195 (18): 2010.

[56] Zhang, T., Imanishi, N., Shimonishi, Y., Hirano, A., Xie, J., Takeda, Y., Yamamoto, O., Sammes, N., Stability of a Water-Stable Lithium Metal Anode for a Lithium–Air Battery with Acetic Acid–Water Solutions. J. Electrochem. Soc. 157 (2): 2010.

[57] Li, L., Zhao, X., Manthiram, A., A dual-electrolyte rechargeable Li-air battery with phosphate buffer catholyte. Electrochem. commun. 14 (1): 2012.

[58] Yang, S., Knickle, H., Design and analysis of aluminum/air battery system for electric vehicles. J. Power Sources. 112 (1): 2002.

[59] Arora, P., Zhang, Z. (John), Battery Separators. Chem. Rev. 104 (10): 4419–4462, 2004.

[60] Gilje, S., Han, S., Wang, M., Wang, K.L., Kaner, R.B., A chemical route to graphene for device applications. Nano Lett. 7 (11): 2007.

[61] Ye, S.J., Kim, D.Y., Kim, D.W., Park, O.O., Kang, Y., Facile synthesis of palladium nanodendrites supported on graphene nanoplatelets: An efficient catalyst for low overpotentials in lithium-oxygen batteries. J. Mater. Chem. A. 2015.

[62] Sevim, M., Francia, C., Amici, J., Vankova, S., Şener, T., Metin, Ö., Bimetallic MPt (M: Co, Cu, Ni) alloy nanoparticles assembled on reduced graphene oxide as high performance cathode catalysts for rechargable lithium-oxygen batteries. J. Alloys Compd. 2016.

[63]   Visco SJ, Nimon E, De Jonghe LC, Katz B, C.M., Lithium fuel cells. In: 12th international meeting on lithium batteries. p. 53 , Japan, 2004.

[64]   He, M., Zhang, P., Liu, L., Liu, B., Xu, S., Hierarchical porous nitrogen doped three-dimensional graphene as a free-standing cathode for rechargeable lithium-oxygen batteries. Electrochim. Acta. 191 2016.

[65]   Hassan, H.M.A., Abdelsayed, V., Khder, A.E.R.S., Abouzeid, K.M., Terner, J., El-Shall, M.S., Al-Resayes, S.I., El-Azhary, A.A., Microwave synthesis of graphene sheets supporting metal nanocrystals in aqueous and organic media. J. Mater. Chem. 19 (23): 2009.

[66]   Guo, X., Han, J., Liu, P., Ito, Y., Hirata, A., Chen, M., Graphene@nanoporous nickel cathode for Li−O$_2$ Batteries. ChemNanoMat. 2 (3): 2016.

[67]   Han, J., Guo, X., Ito, Y., Liu, P., Hojo, D., Aida, T., Hirata, A., Fujita, T., Adschiri, T., Zhou, H., Chen, M., Effect of chemical doping on cathodic performance of bicontinuous nanoporous graphene for Li-O$_2$ batteries. Adv. Energy Mater. 6 (3): 2016.

[68]   He, P., Wang, Y., Zhou, H., A Li-air fuel cell with recycle aqueous electrolyte for improved stability. Electrochem. commun. 12 (12): 2010.

[69]   He, P., Wang, Y., Zhou, H., The effect of alkalinity and temperature on the performance of lithium-air fuel cell with hybrid electrolytes. J. Power Sources. 196 (13): 2011.

[70]   Wang, Y., Zhou, H., A lithium-air battery with a potential to continuously reduce O$_2$ from air for delivering energy. J. Power Sources. 195 (1): 2010.

[71]   Yilmaz, E., Yogi, C., Yamanaka, K., Ohta, T., Byon, H.R., Promoting formation of noncrystalline Li$_2$O$_2$ in the Li-O$_2$ battery with RuO$_2$ nanoparticles. Nano Lett. 2013.

[72]   Lin, X., Yuan, R., Cai, S., Jiang, Y., Lei, J., Liu, S.G., Wu, Q.H., Liao, H.G., Zheng, M., Dong, Q., An Open-Structured Matrix as Oxygen Cathode with High Catalytic Activity and Large Li$_2$O$_2$ Accommodations for Lithium–Oxygen Batteries. Adv. Energy Mater. 8 (18): 2018.

[73]   Cao, B., Xu, H., Mao, C., Transmission electron microscopy as a tool to image bioinorganic nanohybrids: The case of phage-gold nanocomposites. Microsc. Res. Tech. 74 (7): 2011.

[74]   Kim, D.S., Lee, G.H., Lee, S., Kim, J.C., Lee, H.J., Kim, B.K., Kim, D.W., Electrocatalytic performance of CuO/graphene nanocomposites for Li–O$_2$ batteries. J. Alloys Compd. 707 2017.

[75]    Kim, H., Jeong, G., Kim, Y.U., Kim, J.H., Park, C.M., Sohn, H.J., Metallic anodes for next generation secondary batteries, 2013.

[76]    Zhang, K., Zhang, L.L., Zhao, X.S., Wu, J., Graphene/polyaniline nanofiber composites as supercapacitor electrodes. Chem. Mater. 22 (4): 2010.

[77]    Nam, K.T., Kim, D.W., Yoo, P.J., Chiang, C.Y., Meethong, N., Hammond, P.T., Chiang, Y.M., Belcher, A.M., Virus-enabled synthesis and assembly of nanowires for lithium ion battery electrodes. Science (80-. ). 312 (5775): 2006.

[78]    Kim, J.H., Kannan, A.G., Woo, H.S., Jin, D.G., Kim, W., Ryu, K., Kim, D.W., A bi-functional metal-free catalyst composed of dual-doped graphene and mesoporous carbon for rechargeable lithium-oxygen batteries. J. Mater. Chem. A. 3 (36): 2015.

[79]    Kim, S., Kwon, K.C., Park, J.Y., Cho, H.W., Lee, I., Kim, S.Y., Lee, J.L., Challenge beyond Graphene: Metal Oxide/Graphene/Metal Oxide Electrodes for Optoelectronic Devices. ACS Appl. Mater. Interfaces. 8 (20): 2016.

[80]    Knosp, B., Jordy, C., Blanchard, P., Berlureau, T., Evaluation of Zr ( Ni , Mn ) 2 laves phase alloys as negative active material for Ni-mMH electric vehicle batteries. J. Electrochem. Soc. 145 (5): 1998.

[81]    Yoo, E., Zhou, H., Li-air rechargeable battery based on metal-free graphene nanosheet catalysts. ACS Nano. 5 (4): 2011.

[82]    Cetinkaya, T., Akbulut, H., Tokur, M., Ozcan, S., Uysal, M., High capacity Graphene/$\alpha$-MnO$_2$ nanocomposite cathodes for Li–O$_2$ batteries. Int. J. Hydrogen Energy. 2016.

[83]    Liu, C., Younesi, R., Tai, C.W., Valvo, M., Edström, K., Gustafsson, T., Zhu, J., 3-D binder-free graphene foam as a cathode for high capacity Li-O$_2$ batteries. J. Mater. Chem. A. 4 (25): 2016.

[84]    Chase, M., NIST-JANAF Thermochemical Tables, 4th Edition, 1998.

[85]    Li, F., Zhu, M., Luo, Z., Guo, L., Bian, Z., Li, Y., Luo, K., Nitrogen-doped graphene derived from polyaniline/graphene oxide composites with improved capacity and cyclic performance of Li-O$_2$ battery. J. Solid State Electrochem. 23 (8): 2019.

[86]    Qu, K., Zheng, Y., Dai, S., Qiao, S.Z., Graphene oxide-polydopamine derived N, S-codoped carbon nanosheets as superior bifunctional electrocatalysts for oxygen reduction and evolution. Nano Energy. 19: 2016.

[87]    Ji, X., Evers, S., Black, R., Nazar, L.F., Stabilizing lithium-sulphur cathodes using polysulphide reservoirs. Nat. Commun. 2 (1): 2011.

[88]     Jia, N., Liu, J., Gao, Y., Chen, P., Chen, X., An, Z., Li, X., Chen, Y., Graphene-Encapsulated Co9S8 Nanoparticles on N,S-Codoped Carbon Nanotubes: An Efficient Bifunctional Oxygen Electrocatalyst. ChemSusChem. 12 (14): 2019.

[89]     Wang, Y., Zhou, H., A lithium-air fuel cell using copper to catalyze oxygen-reduction based on copper-corrosion mechanism. Chem. Commun. 46 (34): 2010.

[90]     Goldstein, J., Brown, I., Koretz, B., New developments in the electric fuel Ltd. zinc/air system. J. Power Sources. 80 (1): 1999.

[91]     Geng, P., Zheng, S., Tang, H., Zhu, R., Zhang, L., Cao, S., Xue, H., Pang, H., Transition metal sulfides based on graphene for electrochemical energy storage, 2018.

[92]     Fujinaga, T., Sakura, S., Polarographic investigation of dissolved oxygen in nonaqueous solvent. Bull. Chem. Soc. Jpn. 47 (11): 2781–2786, 1974.

[93]     Ding, N., Chien, S.W., Hor, T.S.A., Lum, R., Zong, Y., Liu, Z., Influence of carbon pore size on the discharge capacity of Li–$O_2$ batteries. J. Mater. Chem. A. 2 (31): 12433–12441, 2014.

[94]     Kumar, B., Kumar, J., Leese, R., Fellner, J.P., Rodrigues, S.J., Abraham, K.M., A Solid-State, Rechargeable, Long Cycle Life Lithium–Air Battery. J. Electrochem. Soc. 157 (1): 2010.

[95]     Ferrari, A.C., Raman spectroscopy of graphene and graphite: Disorder, electron-phonon coupling, doping and nonadiabatic effects. Solid State Commun. 143 (1–2): 2007.

[96]     Lu, Y.C., Gasteiger, H.A., Parent, M.C., Chiloyan, V., Shao-Horn, Y., The influence of catalysts on discharge and charge voltages of rechargeable Li-oxygen batteries. Electrochem. Solid-State Lett. 13 (6): 2010.

[97]     Yang, Z.Z., Zheng, Q. Bin, Qiu, H.X., Li, J., Yang, J.H., A simple method for the reduction of graphene oxide by sodium borohydride with $CaCl_2$ as a catalyst. Xinxing Tan Cailiao/New Carbon Mater. 30 (1): 2015.

[98]     Zheng, J.P., Liang, R.Y., Hendrickson, M., Plichta, E.J., Theoretical Energy Density of Li–Air Batteries. J. Electrochem. Soc. 155 (6): 2008.

[99]     Jin, Y., Huang, S., Zhang, M., Jia, M., Hu, D., A green and efficient method to produce graphene for electrochemical capacitors from graphene oxide using sodium carbonate as a reducing agent. Appl. Surf. Sci. 268: 2013.

[100] He, P., Wang, Y., Zhou, H., Titanium nitride catalyst cathode in a Li-air fuel cell with an acidic aqueous solution. Chem. Commun. 47 (38): 2011.

[101] Guo, X., Liu, P., Han, J., Ito, Y., Hirata, A., Fujita, T., Chen, M., 3D nanoporous nitrogen-doped graphene with encapsulated $RuO_2$ nanoparticles for $Li-O_2$ batteries. Adv. Mater. 27 (40): 2015.

[102] Ganesan, P., Prabu, M., Sanetuntikul, J., Shanmugam, S., Cobalt sulfide nanoparticles grown on nitrogen and sulfur codoped graphene oxide: An efficient electrocatalyst for oxygen reduction and evolution reactions. ACS Catal. 5 (6): 2015.

[103] Park, H., Chang, S., Jean, J., Cheng, J.J., Araujo, P.T., Wang, M., Bawendi, M.G., Dresselhaus, M.S., Bulović, V., Kong, J., Gradečak, S., Graphene cathode-based ZnO nanowire hybrid solar cells. Nano Lett. 13 (1): 2013.

[104] Lyu, Z., Zhang, J., Wang, L., Yuan, K., Luan, Y., Xiao, P., Chen, W., $CoS_2$ nanoparticles-graphene hybrid as a cathode catalyst for aprotic $Li-O_2$ batteries. RSC Adv. 6 (38): 2016.

[105] Wang, Y., He, P., Zhou, H., A lithium-air capacitor-battery based on a hybrid electrolyte. Energy Environ. Sci. 4 (12): 2011.

[106] Lin, X., Cao, Y., Cai, S., Fan, J., Li, Y., Wu, Q.H., Zheng, M., Dong, Q., Ruthenium@mesoporous graphene-like carbon: A novel three-dimensional cathode catalyst for lithium-oxygen batteries. J. Mater. Chem. A. 4 (20): 2016.

[107] Kumar, B., Kumar, J., Cathodes for solid-state lithium–oxygen cells: roles of nasicon glass-ceramics. J. Electrochem. Soc. 157 (5): 2010.

[108] Kou, L., He, H., Gao, C., Click chemistry approach to functionalize two-dimensional macromolecules of graphene oxide nanosheets. Nano-Micro Lett. 2 (3): 2010.

[109] Shui, J., Lin, Y., Connell, J.W., Xu, J., Fan, X., Dai, L., Nitrogen-doped holey graphene for high-performance rechargeable $Li-O_2$ batteries. ACS Energy Lett. 1 (1): 2016.

[110] Zhang, P., Wang, R., He, M., Lang, J., Xu, S., Yan, X., 3D Hierarchical Co/CoO-graphene-carbonized melamine foam as a superior cathode toward long-life lithium oxygen batteries. Adv. Funct. Mater. 26 (9): 2016.

[111] Lu, Y.-C., Gasteiger, H.A., Crumlin, E., McGuire, R., Shao-Horn, Y., Electrocatalytic activity studies of select metal surfaces and ımplications in Li-Air batteries. J. Electrochem. Soc. 157 (9): 2010.

[112] Khan, M., Al-Marri, A.H., Khan, M., Shaik, M.R., Mohri, N., Adil, S.F., Kuniyil, M., Alkhathlan, H.Z., Al-Warthan, A., Tremel, W., Tahir, M.N., Siddiqui, M.R.H., Green approach for the effective reduction of graphene oxide using Salvadora persica L. root (Miswak) extract. Nanoscale Res. Lett. 10 (1): 2015.

[113] Sun, B., Huang, X., Chen, S., Munroe, P., Wang, G., Porous graphene nanoarchitectures: An efficient catalyst for low charge-overpotential, long life, and high capacity lithium-oxygen batteries. Nano Lett. 14 (6): 2014.

[114] Guo, S., Sun, S., FePt nanoparticles assembled on graphene as enhanced catalyst for oxygen reduction reaction. J. Am. Chem. Soc. 134 (5): 2012.

[115] Oh, D., Qi, J., Lu, Y.C., Zhang, Y., Shao-Horn, Y., Belcher, A.M., Biologically enhanced cathode design for improved capacity and cycle life for lithium-oxygen batteries. Nat. Commun. 2013.

[116] Liu, X., Amiinu, I.S., Liu, S., Cheng, K., Mu, S., Transition metal/nitrogen dual-doped mesoporous graphene-like carbon nanosheets for the oxygen reduction and evolution reactions. Nanoscale. 8 (27): 2016.

[117] Stankovich, S., Dikin, D.A., Piner, R.D., Kohlhaas, K.A., Kleinhammes, A., Jia, Y., Wu, Y., Nguyen, S.B.T., Ruoff, R.S., Synthesis of graphene-based nanosheets via chemical reduction of exfoliated graphite oxide. Carbon N. Y. 2007.

[118] Gnana Kumar, G., Christy, M., Jang, H., Nahm, K.S., Cobaltite oxide nanosheets anchored graphene nanocomposite as an efficient oxygen reduction reaction (ORR) catalyst for the application of lithium-air batteries. J. Power Sources. 2015.

[119] Pei, S., Cheng, H.-M., The reduction of graphene oxide. Carbon N. Y. 50 (9): 3210–3228, 2012.

[120] Pham, V.H., Pham, H.D., Dang, T.T., Hur, S.H., Kim, E.J., Kong, B.S., Kim, S., Chung, J.S., Chemical reduction of an aqueous suspension of graphene oxide by nascent hydrogen. J. Mater. Chem. 22 (21): 2012.

[121] Qu, K., Zheng, Y., Dai, S., Qiao, S.Z., Polydopamine-graphene oxide derived mesoporous carbon nanosheets for enhanced oxygen reduction. Nanoscale. 7 (29): 2015.

[122] Moon, I.K., Lee, J., Ruoff, R.S., Lee, H., Reduced graphene oxide by chemical graphitization. Nat. Commun. 1 (6): 2010.

[123] Özcan, Ş., Cetinkaya, T., Tokur, M., Algül, H., Guler, M.O., Akbulut, H., Synthesis of flexible pure graphene papers and utilization as free standing cathodes for lithium-air batteries. Int. J. Hydrogen Energy. 2016.

[124] Mao, S., Pu, H., Chen, J., Graphene oxide and its reduction: modeling and experimental progress. RSC Adv. 2 (7): 2643, 2012.

[125] Ma, Y., Wei, L., Gu, Y., Hu, J., Chen, Y., Qi, P., Zhao, X., Peng, Y., Deng, Z., Liu, Z., High-performance Li–$O_2$ batteries based on all-Graphene backbone. Adv. Funct. Mater. 2020.

[126] Chen, S., Duan, J., Han, W., Qiao, S.Z., A graphene–$MnO_2$ framework as a new generation of three-dimensional oxygen evolution promoter. Chem. Commun. 50 (2): 2014.

[127] Gadgil, B., Damlin, P., Kvarnström, C., Graphene vs. reduced graphene oxide: A comparative study of graphene-based nanoplatforms on electrochromic switching kinetics, 2016.

[128] Gao, W., Alemany, L.B., Ci, L., Ajayan, P.M., New insights into the structure and reduction of graphite oxide. Nat. Chem. 1 (5): 2009.

[129] Geim, A.K., Novoselov, K.S., The rise of graphene. Nat. Mater. 6 (3): 183–191, 2007.

[130] Wang, Y.F., Yang, S.Y., Yue, Y., Bian, S.W., Conductive copper-based metal-organic framework nanowire arrays grown on graphene fibers for flexible all-solid-state supercapacitors. J. Alloys Compd. 835: 2020.

[131] Singh, E., Meyyappan, M., Nalwa, H.S., Flexible Graphene-Based Wearable Gas and Chemical Sensors, 2017.

[132] Huang, J., Zhang, B., Xie, Y.Y., Lye, W.W.K., Xu, Z.L., Abouali, S., Akbari Garakani, M., Huang, J.Q., Zhang, T.Y., Huang, B., Kim, J.K., Electrospun graphitic carbon nanofibers with in-situ encapsulated Co-Ni nanoparticles as freestanding electrodes for Li-$O_2$ batteries. Carbon N. Y. 100: 2016.

[133] Yoo, E., Nakamura, J., Zhou, H., N-Doped graphene nanosheets for Li-air fuel cells under acidic conditions. Energy Environ. Sci. 5 (5): 2012.

[134] Chen, W., Yan, L., Bangal, P.R., Chemical reduction of graphene oxide to graphene by sulfur-containing compounds. J. Phys. Chem. C. 114 (47): 2010.

[135] Lei, Z., Lu, L., Zhao, X.S., The electrocapacitive properties of graphene oxide reduced by urea. Energy Environ. Sci. 5 (4): 2012.

[136] Fan, Z., Wang, K., Wei, T., Yan, J., Song, L., Shao, B., An environmentally friendly and efficient route for the reduction of graphene oxide by aluminum powder, 2010.

[137] Song, P., Zhang, X., Sun, M., Cui, X., Lin, Y., Synthesis of graphene nanosheets via oxalic acid-induced chemical reduction of exfoliated graphite oxide. RSC Adv. 2012.

[138] Giovannetti, G., Khomyakov, P.A., Brocks, G., Karpan, V.M., Van Den Brink, J., Kelly, P.J., Doping graphene with metal contacts. Phys. Rev. Lett. 101 (2): 2008.

[139] Chua, C.K., Pumera, M., The reduction of graphene oxide with hydrazine: elucidating its reductive capability based on a reaction-model approach. Chem. Commun. 52 (1): 2016.

[140] Wu, G., MacK, N.H., Gao, W., Ma, S., Zhong, R., Han, J., Baldwin, J.K., Zelenay, P., Nitrogen-doped graphene-rich catalysts derived from heteroatom polymers for oxygen reduction in nonaqueous lithium-$O_2$ battery cathodes. ACS Nano. 6 (11): 2012.

[141] Zu, C., Li, L., Qie, L., Manthiram, A., Expandable-graphite-derived graphene for next-generation battery chemistries. J. Power Sources. 284 2015.

[142] Thapa, A.K., Ishihara, T., Mesoporous $\alpha$-$MnO_2$/Pd catalyst air electrode for rechargeable lithium-air battery. J. Power Sources. 2011.

[143] Zhang, S.S., Foster, D., Read, J., Discharge characteristic of a non-aqueous electrolyte Li/O2 battery. J. Power Sources. 195 (4): 2010.

[144] Bhattacharya, G., Sas, S., Wadhwa, S., Mathur, A., McLaughlin, J., Roy, S.S., Aloe vera assisted facile green synthesis of reduced graphene oxide for electrochemical and dye removal applications. RSC Adv. 7 (43): 2017.

[145] Wu, J. Bin, Lin, M.L., Cong, X., Liu, H.N., Tan, P.H., Raman spectroscopy of graphene-based materials and its applications in related devices, 2018.

[146] Radin, M.D., Rodriguez, J.F., Tian, F., Siegel, D.J., Lithium peroxide surfaces are metallic, while lithium oxide surfaces are not. J. Am. Chem. Soc. 134 (2): 2012.

[147] Read, J., Characterization of the Lithium/Oxygen Organic Electrolyte Battery. J. Electrochem. Soc. 149 (9): 2002.

[148] Cui, X., Luo, Y., Zhou, Y., Dong, W., Chen, W., Application of functionalized graphene in Li-$O_2$ batteries, 2021.

[149] Zhu, L., Scheiba, F., Trouillet, V., Georgian, M., Fu, Q., Sarapulpva, A., Sigel, F., Hua, W., Ehrenberg, H., $MnO_2$ and reduced graphene oxide as bifunctional electrocatalysts for Li-$O_2$ batteries. ACS Appl. Energy Mater. 2019.

[150] Xin, X., Ito, K., Kubo, Y., Graphene/activated carbon composite material for oxygen electrodes in lithium-oxygen rechargeable batteries. Carbon N. Y. 99 2016.

[151] Shu, C., Li, B., Zhang, B., Su, D., Hierarchical Nitrogen-Doped Graphene/Carbon Nanotube Composite Cathode for Lithium-Oxygen Batteries. ChemSusChem. 8 (23): 2015.

[152] Jung, H.G., Jeong, Y.S., Park, J.B., Sun, Y.K., Scrosati, B., Lee, Y.J., Ruthenium-based electrocatalysts supported on reduced graphene oxide for lithium-air batteries. ACS Nano. 7 (4): 2013.

[153] Jeong, Y.S., Park, J.B., Jung, H.G., Kim, J., Luo, X., Lu, J., Curtiss, L., Amine, K., Sun, Y.K., Scrosati, B., Lee, Y.J., Study on the Catalytic Activity of Noble Metal Nanoparticles on Reduced Graphene Oxide for Oxygen Evolution Reactions in Lithium-Air Batteries. Nano Lett. 2015.

[154] Zhang, X., Chen, X., Chen, C., Liu, T., Liu, M., Zhang, C., Huang, T., Yu, A., Ruthenium oxide modified hierarchically porous boron-doped graphene aerogels as oxygen electrodes for lithium-oxygen batteries. RSC Adv. 8 (70): 2018.

[155] Chen, X., Zhang, X., Chen, C., Huang, T., Yu, A., A porous Co-Ru@C shell as a bifunctional catalyst for lithium-oxygen batteries. RSC Adv. 8 (42): 2018.

[156] Sawyer, D.T., Chlerlcato, G., Angells, C.T., Nanni, E.J., Tsuchiya, T., Effects of Media and Electrode Materials on the Electrochemical Reduction of Dioxygen. Anal. Chem. 54 (11): 1982.

[157] Thapa, A.K., Saimen, K., Ishihara, T., Pd/ $MnO_2$ air electrode catalyst for rechargeable lithium/air battery. Electrochem. Solid-State Lett. 13 (11): 2010.

[158] Tong, H., Bai, W., Yue, S., Gao, Z., Lu, L., Shen, L., Dong, S., Zhu, J., He, J., Zhang, X., Zinc cobalt sulfide nanosheets grown on nitrogen-doped graphene/carbon nanotube film as a high-performance electrode for supercapacitors. J. Mater. Chem. A. 4 (29): 2016.

[159] Liu, S., Zhang, C., Yue, W., Chen, X., Yang, X., Graphene-Based Mesoporous $SnO_2$ Nanosheets as Multifunctional Hosts for High-Performance Lithium-Sulfur Batteries. ACS Appl. Energy Mater. 2 (7): 2019.

[160] Black, R., Lee, J.H., Adams, B., Mims, C.A., Nazar, L.F., The role of catalysts and peroxide oxidation in lithium-oxygen batteries. Angew. Chemie - Int. Ed. 2013.

[161] Aurbach, D., Daroux, M., Faguy, P., Yeager, E., The electrochemistry of noble metal electrodes in aprotic organic solvents containing lithium salts. J. Electroanal. Chem. 297 (1): 1991.

[162] Saikia, B.K., Boruah, R.K., Gogoi, P.K., A X-ray diffraction analysis on graphene layers of Assam coal. J. Chem. Sci. 121 (1): 2009.

[163] Ang, H., Zhang, W., Tan, H.T., Chen, H., Yan, Q., Copper oxide supported on platinum nanosheets array: High performance carbon-free cathode for lithium-oxygen cells. J. Power Sources. 294: 2015.

[164] Jung, K.N., Riaz, A., Lee, S.B., Lim, T.H., Park, S.J., Song, R.H., Yoon, S., Shin, K.H., Lee, J.W., Urchin-like $\alpha$-$MnO_2$ decorated with Au and Pd as a bi-functional catalyst for rechargeable lithium-oxygen batteries. J. Power Sources. 2013.

[165] Cheng, J., Jiang, Y., Zhang, M., Zou, L., Huang, Y., Wang, Z., Chi, B., Pu, J., Li, J., Perovskite-type $La_{0.8}Sr_{0.2}Co_{0.8}Fe_{0.2}O_3$ with uniform dispersion on N-doped reduced graphene oxide as an efficient bi-functional Li-$O_2$ battery cathode. Phys. Chem. Chem. Phys. 2017.

[166] Wang, X., Wang, Q., Hou, X., Liu, Y., Zheng, P., Huo, J., Yin, L., Guo, S., Facile fabrication of two-dimensional reduced graphene oxide/CoAl-layered double hydroxides nanocomposites for lithium-oxygen battery with improved electrochemical performance. J. Alloys Compd. 2018.

[167] Kim, J.G., Kim, Y., Noh, Y., Lee, S., Kim, Y., Kim, W.B., Bifunctional Hybrid Catalysts with Perovskite $LaCo_{0.8}Fe_{0.2}O_3$ Nanowires and Reduced Graphene Oxide Sheets for an Efficient Li-$O_2$ Battery Cathode. ACS Appl. Mater. Interfaces. 2018.

[168] Ren, X., Liao, B., Li, Y., Zhang, P., Deng, L., Gao, Y., Facile synthesis of PdSnCo/nitrogen-doped reduced graphene as a highly active catalyst for lithium-air batteries. Electrochim. Acta. 2017.

[169] Sun, C., Li, F., Ma, C., Wang, Y., Ren, Y., Yang, W., Ma, Z., Li, J., Chen, Y., Kim, Y., Chen, L., Graphene-$Co_3O_4$ nanocomposite as an efficient bifunctional catalyst for lithium-air batteries. J. Mater. Chem. A. 2014.

[170] Zhang, J., Li, P., Wang, Z., Qiao, J., Rooney, D., Sun, W., Sun, K., Three-dimensional graphene-$Co_3O_4$ cathodes for rechargeable Li-$O_2$ batteries. J. Mater. Chem. A. 3 (4): 2015.

[171] Song, C., Cao, L., Li, B., Huang, X., Ye, K., Zhu, K., Cao, D., Cheng, K., Wang, G., Highly efficient palladium nanoparticles decorated reduced graphene oxide sheets supported on nickel foam for hydrogen peroxide electroreduction. Appl. Surf. Sci. 426: 2017.

[172] Zhang, T., Imanishi, N., Takeda, Y., Yamamoto, O., Aqueous lithium/air rechargeable batteries, 2011.

[173] Zhao, C.T., Yu, C., Liu, S.H., Yang, J., Fan, X.M., Huang, H.W., Qiu, J., 3D Porous N-Doped Graphene Frameworks Made of Interconnected Nanocages for Ultrahigh-Rate and Long-Life Li-O$_2$ Batteries. Adv. Funct. Mater. 25 (44): 2015.

# RESUME

**Name Surname**          **: Ahmed Al-Ogaili**

## EDUCATION

| Degree | School | Graduation Year |
|---|---|---|
| Ph.D. | Sakarya University / Natural Science Institute / Nanoscience and Nanoengineering | 2021 |
| Master | Osmania University / Science Institute  / Biotechnology | 2013 |
| Undergraduate | Anbar University / Science Institute / Biology | 2009 |
| High School | Abdullah Ben Mubarak Iraq | 2005 |

## JOB EXPERIENCE

| Year | Place | Position |
|---|---|---|
| 2017-Still | SARGEM Laboratories | Project assistant |
| 2016-2017 | Ostrava technical university | Researcher |
| 2013 | DNA Lab of India | Internship |
| 2012 | Bioaxis Institute | Internship |

## FOREIGN LANGUAGE

English
Turkish
Arabic

**PRODUCTS (article, paper, project, ets.)**

**1.** S. Pakseresht, T. Cetinkaya, A. W. M. Al-Ogaili, H. Akbulut, Urchin-like core-shell $TiO_2/\alpha-MnO_2$ nanostructures as an active catalyst for rechargeable lithium-oxygen battery, Advanced powder technology, 32(3), 2021, 895-907.

**2.** S. Pakseresht, T. Cetinkaya, A. W. M. Al-Ogaili, M. Halebi, H. Akbulut, Biologically synthesized $TiO_2$ nanoparticles and their application as lithium-air battery cathodes. Ceramics International. 47 (3), 3994-4005, 2021.

**3.** Ahmed Waleed Majeed Al-Ogaili, Tugrul Cetinkaya, Sara Pakseresht, Hatem Akbulut, Graphene-based nanocomposite cathodes architecture with palladium and $\alpha-MnO_2$ for high cycle life lithium-oxygen batteries. Journal of Alloys and Compounds, 854, 157293, 2021.

**4.** S. Pakseresht, A.W.M Al-ogaili, H. Akbulut, D. Placha, E. Pazdziora, D. Klushina, G.S. Martynková, Silver/Chitosan Antimicrobial Nanocomposites Coating for Medical Devices: Comparison of Nanofiller Effect Prepared via Chemical Reduction and Biosynthesis. Journal of Nanoscience and Nanotechnology. 19 (2018) 2938–2942.

**5.** Ahmed waleed majeed, prajitha E.M, Satti Vishnupriya, Role of caspase8 6N Ins/del in chronic myeloid leukemia, Helix journal. Vol. 1:478- 482 (2014).

**6.** Ahmed Waleed Majeed and Sara Pakseresht, Transformation of penicillin resistance plasmid from penicillin resistant soil bacteria to E.coli DH5α, Helix Journal, 1 (2014) 491- 493.

**7.** Sara Pakseresht and Ahmed Waleed Majeed, Production and  Qualitative Analysis of Secondary Metabolites of Staphylococcus Bacteria having Antibiotic Activity, Helix Journal, 2 (2014) 527- 530.

**8.** Projects: a) Novel carbon-free cathode materials for metal-air rechargeable batteries. Supported by TÜBITAK under contract number 217M979. (2018-2021)

b) A new approach to electrochemical energy storage: development of multi-cell lithium-air flow batteries. Supported by TÜBITAK under contract number 315M461 (2017-2019).

**9.** A. Al-ogaili, Oral presentation titled: Facile preparation of $rGO@RuO_2@\alpha-MnO_2$ hybrid as the air breathing cathode for rechargeable $Li-O_2$ batteries, International

symposium on Nanoparticles/Nanomaterials and Applications, Caparica, Portugal, 2020.

**10.** A. Al-ogaili, Oral presentation titled: High Cyclability rGO/Pd/$\alpha$-MnO$_2$ Nanocomposite for Lithium-Air Battery Utilized as Air Breathing Cathode, Electrochemistry Conference (ISI), Istanbul, Turkey, 2019.

**11.** A. Al-ogaili, S.pakseresht, Grazyna Simha, Poster titled: Fabrication of Sulfur/Carbon/Clay mineral cathode material and its electrical performance, NanoOstrava, Ostrava technical university, Czech Republic, 2017.

**12.** Participated in one day seminar on Perspectives of genomics and epigenomics organized by Osmania University, Hyderabad.

**HOBBIES**

Gaming, Movie, Sport